Università degli Studi di Catania
Dottorato di Ricerca in Fisica – XXVI Ciclo
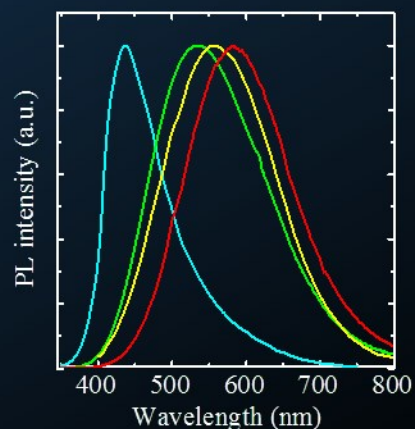
Gabriele Bellocchi

Visible light emission from Eu-containing Si-based materials

Tutor: Chiar.mo Prof. Francesco Priolo
Supervisors: Dr.ssa Giorgia Franzò
Dr. Fabio Iacona
Coordinatore : Chiar.mo Prof. Francesco Riggi

Università degli Studi di Catania

Dottorato di Ricerca in Fisica – XXVI Ciclo
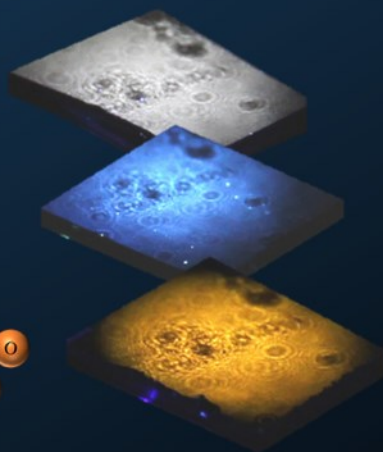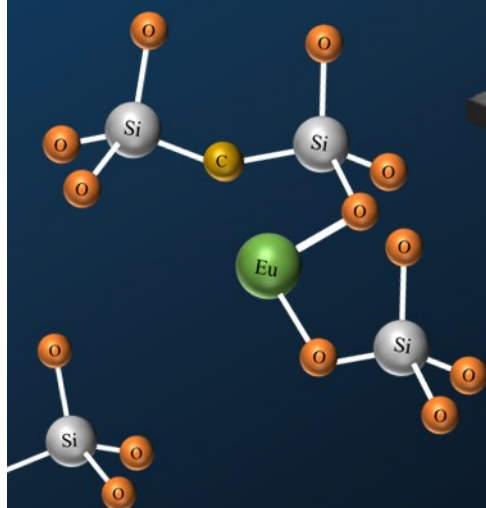
Gabriele Bellocchi

**Visible light emission from
Eu-containing Si-based materials**

Tutor: Chiar.mo Prof. Francesco Priolo

Supervisors: Dr.ssa Giorgia Franzò

Dr. Fabio Iacona

Coordinatore: Chiar.mo Prof. Francesco Riggi

Triennium 2010/2013

Cover

From left to right:

Schematic repre sentation of Eu-containing Si-based materials assembly: from atoms to molecular structures.

Photographs of (top) Eu-doped SiOC bilayer, (in the middle) Eu-doped SiOC film and (bottom) Eu silicate film, excited by the 364 nm line of a fully defocused Ar^+ laser beam, showing bright PL emission visible by the naked eye.

Room temperature normalized PL spectra for Eu-doped SiOC films containing four different Eu concentrations.

"La teoria è quando si sa tutto e niente funziona.
La pratica è quando tutto funziona e nessuno sa il perché.
Noi abbiamo messo insieme la teoria e la pratica:
non c'è niente che funzioni... e nessuno sa il perché!".

Albert Einstein

Contents

Chapter 1

Rare earths: properties and applications in Si-based photonics and lighting

Since their discovery, rare earths (REs) have been used in many fields for their peculiar optical properties. In particular, depending on their oxidation state, REs can show different light emission characteristics, spanning from the sharp emission of trivalent RE ions, characterized by low intensity and long decay lifetime, to the broader and more intense bands of the divalent ions. Since many RE ions show light emission in the visible range, they have been widely employed in lighting, in the fabrication of fluorescent lamps or phosphors converting LEDs. A more ambitious application of REs could be envisaged in Si photonics; indeed the doping with REs of Si-based materials represents, together with Si nanostructures, one of the most promising approaches for the development of Si-based light sources. Current applications of RE-doped materials in Si photonics will be reviewed and the future perspectives discussed.

1.1   Optical properties of rare earth ions

Rare earths (REs), also known as lanthanides or lanthanoids, are the elements following lanthanum in the periodic table, as shown in figure 1.1.

Figure 1.1: *Periodic table of elements.*

The electronic configuration of RE ions is $[Xe]4f^n6s^2$ (with $1 \leq n \leq 14$). All REs have a partially filled 4f shell and the same outer-shell configuration, namely $5s^25p^66s^2$. Since the valence electrons are the same for all the ions, they show very similar reactivity and coordination behavior; the 4f electrons are not the outermost ones, and they are shielded from external fields by other electronic shells, i.e. the 5s and 5p with larger radial extension. The result of this shielding is that, when a RE ion is introduced into a solid, the crystal field has almost no effect on the 4f electrons which result only weakly perturbed by the

charge of the surrounding ligands and so the optical properties of RE ions, i.e. the absorption and emission specta, are only slightly affected by the environment [1]. As a consequence, many of the spectroscopic properties of RE ions in solids can be understood from considerations on the free ions. Becquerel, the first scientist that studied the optical properties of RE [2], realized that in many solids the emission lines of RE ions were as narrow as those commonly observed in the spectra of the free atoms or molecules. A schematic representation of RE energy level diagrams for the isolated trivalent ions of each of the 13 lanthanides with partially filled 4f orbitals, from Ce (n = 1) to Yb (n = 13), is shown in figure 1.2, in which the most technologically important radiative transitions are indicated.

The sharp emission lines of REs are associated with $4f^n \longrightarrow 4f^n$ type transitions, which are forbidden for electric dipole radiation by the parity selection rule. However, they are usually observed in crystals since the interaction of the RE ion with the crystal field or with the lattice vibrations partially removes the degeneration in the component m_j of the total angular momentum through the Stark effect and mixing states of different parity into the 4f states. Although these mixtures make the transitions observable, their oscillator strength remains relatively low (about 10^{-6}), and their decay time is of the order of ms.

Although the most common valence state of RE ions in solids is the trivalent one, some REs, such as Sm, Eu and Yb, also occur as divalent ions. The different oxidation state involves a change in the electronic configuration; in particular for divalent RE ions the energy separation between the $4f^n$ and $4f^{n-1}5d$ configuration is smaller (about 3.7 eV) than in the case of trivalent ions (6-12 eV), which allows to observe the $4f^n \longrightarrow 4f^{n-1}5d$ transitions in the UV-visible spectroscopic range. The transitions of divalent RE ions are notably different from those of the trivalent one, showing much broader emission bands. Furthermore $4f^n \longrightarrow 4f^{n-1}5d$ transitions are parity-allowed, and have intensities up

Figure 1.2: *Energy level diagrams for the isolated trivalent ions of lanthanides with partially filled 4f orbitals (a) from Ce to Eu and (b) from Gd to Yb. The arrows indicate the most technologically important optical transitions.*
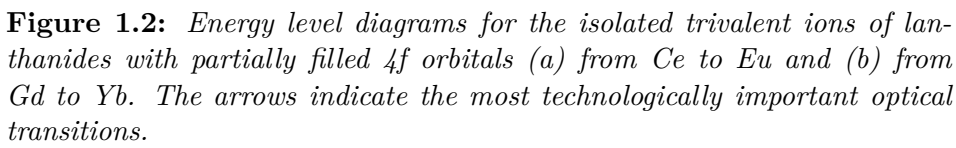
to 10^4 times stronger than the strongest $4f^n \longrightarrow 4f^n$ transitions, and a typical decay time of the order of μs. The energy levels of the $4f^{n-1}5d$ configuration in a solid are subjected to the simultaneous action of the crystal field, electron interactions and spin-orbit coupling. As a result, by changing the RE ion environment a change in the electronic configuration occurs, due to the less localized nature and stronger coupling to lattice vibrations of 5d states, which corresponds to a shift in the position of the emission bands due to $4f^n \longrightarrow 4f^{n-1}5d$ transitions.

Their optical properties make the RE ions highly interesting for many high-tech applications. RE-activated luminescent materials are widely used for solid-state lasers, fluorescent lamps, flat displays, optical fiber communication systems, and other optical devices. Eu, for instance, is used as the red phosphor in colour cathode-ray tubes and liquid-crystal displays. A lot of applications involve electronic transitions between states within a $4f^n$ configuration of trivalent RE ions doped into transparent host materials. The popular solid-state Nd^{3+}:YAG laser, for example, utilizes the 1064 nm electronic transition from the $^4F_{3/2}$ and $^4I_{11/2}$ multiplets within the $4f^3$ configuration of the Nd^{3+} ion [3]. Similarly, the Er fluorescence at 1.5 μm is very important for optical amplification in telecommunications [4–7]. Furthermore divalent RE ions are also used in phosphors in combination with LEDs to obtain high quality white light sources.

In the following sections two of the main fields of RE applications are discussed: lighting and photonics.

1.2   RE based materials in lighting

Lighting has been an integral part of human civilization since before recorded history. Today artificial lighting is a critical issue of modern life. During the past years until up 2009, (European Union's Ecode-

sign Directive 2009/125/EC), the most popular lighting technology have been incandescent lamps. This technology involves the use of electricity, to heat a solid that emits broadband blackbody light. For incandescent lamps, the evolution from electric arc and to carbon-filament, to metal-filament lamps, can be viewed as an attempt to increase the intensity of emitted light, by increasing the temperature of the emitting filament, maintaining an acceptable lifetime. Because the light emitted from incandescent lamps is broadband, most of it lies outside the visible spectrum. This corresponds to a loss of energy, which is dissipated as heat, therefore incandescent lighting is highly inefficient. This has led to a situation where lighting takes up to 6.5 % of the total energy usage world-wide [8]. Energy saving is becoming increasingly important, since easily accessible resources are becoming scarce and more efficient lighting products have to be developed [9]. In this context, during the last decades, light sources with high efficiency and low price, such as fluorescent lamps and LEDs (see figure 1.3), have been produced in order to satisfy the increment of light demand without increasing the energy consumption, as such as fluorescent lamps.

As shown in figure 1.3, a primary attribute of a lighting source is its luminous efficacy measured in (lm/W), which is the efficiency of the conversion from electrical power to optical power, combined with the efficiency of the conversion from optical power to the luminous flux (lm) sensed by the human eye within its spectral responsivity range. The past-two-decades evolution of luminous efficacy of various lighting sources is illustrated in figure 1.3. Nevertheless, for a light source luminous efficacy is not the only parameter to be considered. In fact, for lighting commercial purposes, one of the most important parameter is the spectral power distribution of a light source with respect to its quality perceived by humans. Therefore, characterization of light sources with respect to standard light parameters is of great importance for lighting market and applications. The International
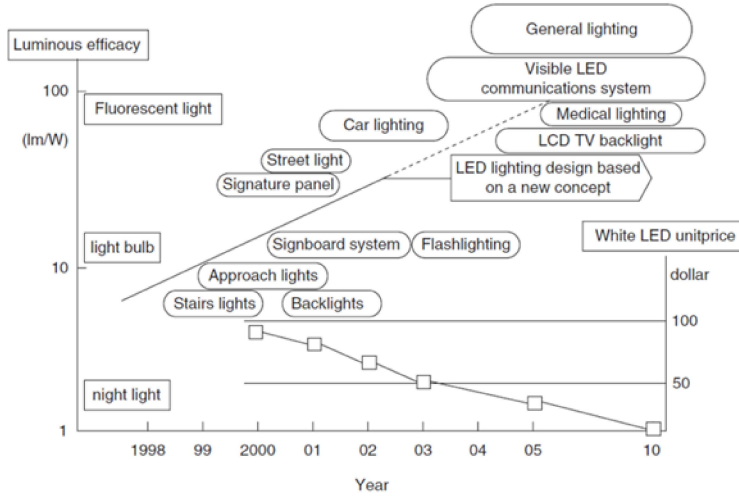
Figure 1.3: *Changes in luminous efficacy of white LEDs, with examples of practical applications and commercialization predictions up to 2010. Prediction of costs per LED unit are also reported [10].*

Commission on Illumination has defined some parameters, based on an averaged human visual perception, to establish the quality of perceived light. The first property of visible light is colour. To define colours emitted from a light source, one of the most important tool is the 1931 Commission Internationale D'Eclairage (CIE) chromaticity diagram [10], shown in figure 1.4. In this diagram the coordinates (x,y) are used to specify the color of a light source independently of the luminous intensity. In figure 1.4 a particular set of coordinates, labeled with black points, are shown. These points define the Planckian locus, which is the set of points in the CIE chromaticity diagram associated to the light emitted from a blackbody radiator at given temperatures (in figure 1.4, the blackbody radiator temperatures range reported is 2500-6500 K).

From the CIE coordinates it is also possible to calculate the cor-
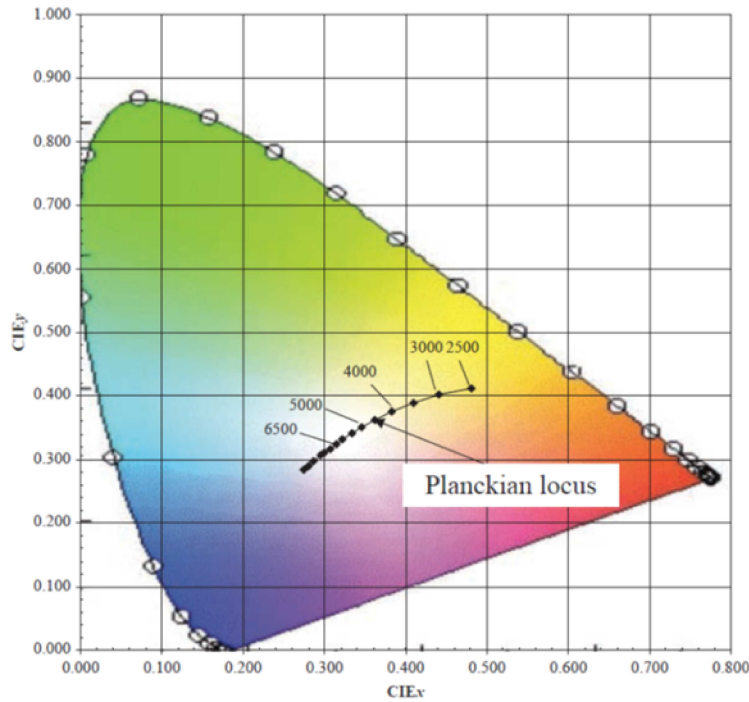
Figure 1.4: *Chromaticity diagram, showing also the Planckian locus in the temperature range 2500-6500 K.*

related color temperature (CCT) of the emission. To establish the CCT of a given light source, which is not a blackbody radiator, the straight isothermal lines perpendicular to the Planckian locus in the CIE diagram have to be considered. The typical CCT sought for lighting applications is along the arc from 3000 to 6000 K, while an ideal white light source has coordinates (0.33, 0.33).

Another important parameter in the classification of light sources is the color rendering index (CRI), which is defined as the ability of a light source to accurately render all frequencies of its color spectrum

when compared to a perfect reference light of a similar type (with the same color temperature). CRI is rated on a scale ranging from 1 to 100: the lower the CRI rating, the less accurately colors will be reproduced. Light sources that are incandescent radiators have a CRI of 100, since all colors in their spectrum are equally rendered, while a monochromatic, low-pressure sodium vapor lamp has a CRI of nearly zero.

The parameters described above are useful to classify the different sources used in lighting. Among the different visible light sources, an increasingly important role is played by light-emitting diodes (LEDs). A LED emits light by applying a forward-bias current into the p-n junction of a semiconductor diode. LEDs available on the market today are manufactured using III-V semiconductor materials such as GaAlAs, AlInGaP, InGaN and AlInGaN [11]. Owing to recent technological advances, the function of LEDs has shifted from display to lighting; indeed they have the same lighting properties of conventional incandescent bulb and fluorescent lamps, but they offer many advantages, such as high-level safety, low-voltage drive and long life, coupled with a compact and lightweight packaging.

Another very popular approach in lighting exploits the luminescence properties of phosphors (figure 1.5). The word phosphor, extensively used to describe luminescent materials, comes from the Greek language and means "light bearer"; barium sulfide is one of the earlier known naturally occurring phosphors [12].

These materials exploit the emission properties of the activators, light emitting impurities which very often are RE ions. Among the RE ions used for this purpose, Ce^{3+} and divalent ions, such as Eu^{2+}, introduced in a solid matrix show many advantages: (i) these ions emit visible light when they undergo d $\longrightarrow$ f rather than f $\longrightarrow$ f electronic transitions, (ii) the emissions arising from d $\longrightarrow$ f electronic transitions are generally more intense than those originating from f $\longrightarrow$ f transitions, (iii) the emissions arising from d $\longrightarrow$ f electronic
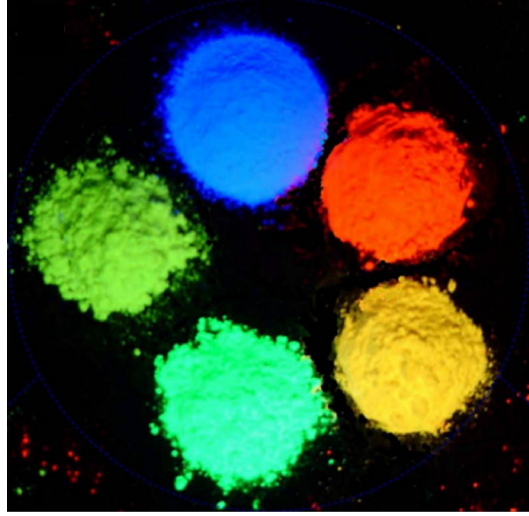
Figure 1.5: *Phosphor powders under UV radiation.*

transitions are broader than those originating from f $\longrightarrow$ f transitions, and (iv) the emission due to d $\longrightarrow$ f electronic transitions is more wavelength tunable than that originating from f $\longrightarrow$ f transitions because d orbitals are more sensitive to chemical environment than the f orbitals. Therefore emission wavelength tunability can be achieved by altering the crystal field splitting of the d orbitals of the activator ion, by changing the host lattice or the activator concentration.

An example of phosphor applications is the fabrication of typical "cool white" fluorescent lamps; as shown in figure 1.6a, two RE-doped phosphors, $LaPO_4:Tb^{3+}$, Ce^{3+} for green and blue emission and $Y_2O_3:Eu^{3+}$ for red, have been used to coat the internal walls of a fluorescent lamp. Following a charge discard, the excited gas (mercury) present inside the lamp bulb emits UV radiation which is absorbed by the phosphors. After this excitation, RE-doped phosphors emit their typical radiation. The combination of the emissions from the

phosphors gives the spectrum shown in figure 1.6b.

The introduction of fluorescent tubes has decreased the energy demand for lighting. However, the narrow optical atomic transition lines emitted by this type of sources results in a reduced light quality with regards to color rendering. A standard "cool white" fluorescent lamp has a CRI of about 63, while newer tri-phosphor fluorescent lamps often claim a CRI of 80-90. Furthermore, the relatively large and fragile glass tubes containing mercury pose limitations to applicability as well as environmental problems.

Since 1997, UV and blue LEDs have been also used to excite phosphors [13–15]. Today a full range of colored phosphor converting LEDs (pcLEDs), which combine the LEDs advantages with the ones of phosphors, is available (figure 1.7) and it is employed in many day-life colored applications, including also displays, displacing more traditional lighting methods.

Recently many efforts have been also devoted to the research on white light emitting pcLEDs. To fabricate a white source a wide emission spectrum is needed, which can be obtained by combination of color conversion phosphors and LEDs or multicolor LEDs. The choice between the different approaches largely depends on the application. In particular, four main different strategies have been used in the literature, which are classified along with an assessment of their relative CRI vs. luminous efficacy attributes:

   i. Combination of red, green and blue LEDs (figure 1.8a). The drawbacks of this approach arise from different aging of the single LEDs and poor CRI due to the narrow emission range of these LEDs. On the other hand, the luminous efficacy is relatively high, because light comes directly from LEDs, with the absence of any color phosphors which can lead to energy loss during the conversion step.

  ii. A pcLED consisting of a blue LED and two color conversion
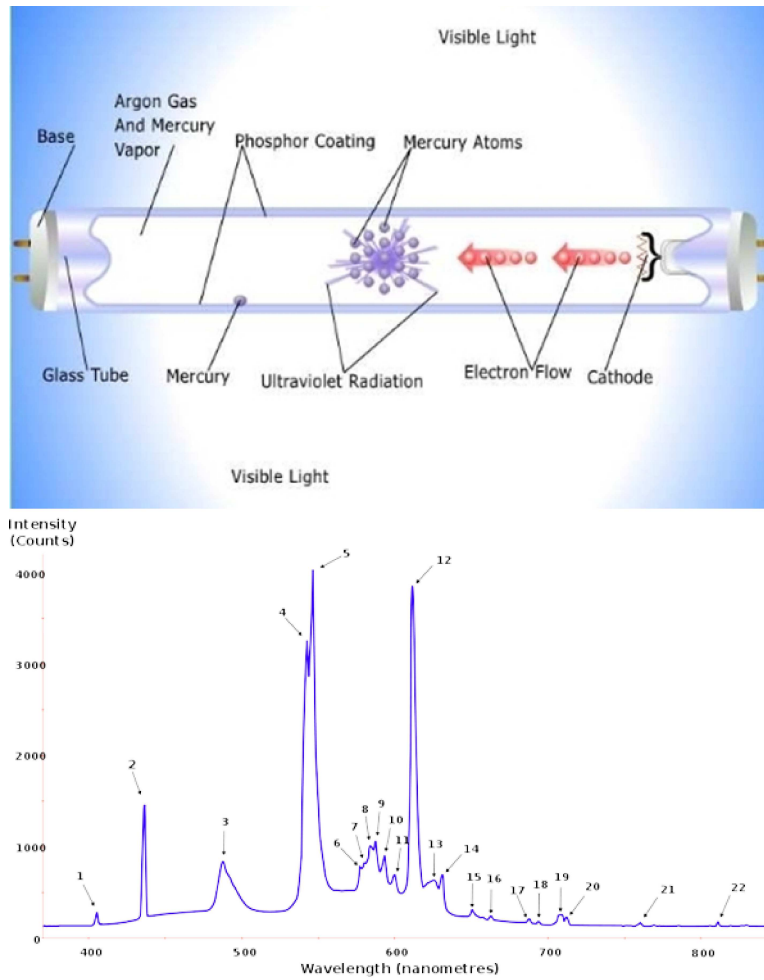
Figure 1.6: *(a) Schematic representation of a typical fluorescent lamp. (b) Emission spectrum of a cool white fluorescent lamp utilizing two RE-doped phosphors. Note that several peaks are directly generated from the mercury arc.*
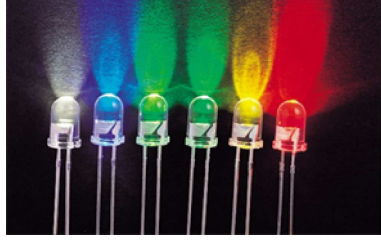
Figure 1.7: *Different colour LEDs.*

phosphors, emitting in the green and red regions of the visible spectrum, as schematically shown in figure 1.8b. This approach uses only a single LED, so overcoming the problem of the different aging of the LEDs. Furthermore, the green and red emitting phosphors can have broad emission wavelength ranges, so the CRI is around 80-90, i.e. higher than for the approach (i). However due to the conversion process of the blue LED emission into green and red due to the phosphors, the overall luminous efficacy of the pcLED is lower than case (i).

iii. A pcLED consisting of a blue LED and a single color conversion phosphor, which emits in the yellow-orange region, as schematically shown in figure 1.8c. This approach uses only a single phosphor, so its emission needs to cover a broad wavelength range in the orange-yellow region in order to achieve a sufficiently high CRI. Nevertheless, there are wavelength regions in the red and between the LED and phosphor emissions where there is little or no light output, so a maximum CRI around 80 is achievable for a pcLED with a single phosphor. Although the CRI is lower than that obtained in case (ii), the luminous efficacy can be higher because the losses due to conversion process are lower than in case (ii), where a large energy loss in converting blue light into red occurs. Consequently, pcLEDs with a single phosphor do

not have sufficiently high CRIs to replace incandescent bulbs or fluorescent lamps for generic white light applications, but they are used instead for niche applications, e.g. for car headlamps.

iv. A pcLED consisting of an UV LED and three phosphors emitting in the blue, green and red regions (figure 1.8d). This approach can achieve a higher CRI ($\geqslant$ 90) than approaches (i)-(iii), because the blue, green and red phosphor emissions can cover the whole visible region. However, there is a trade-off with luminous efficacy, which is lower than for the approaches (i)-(iii) because of the high energy loss in converting UV radiation into visible light.

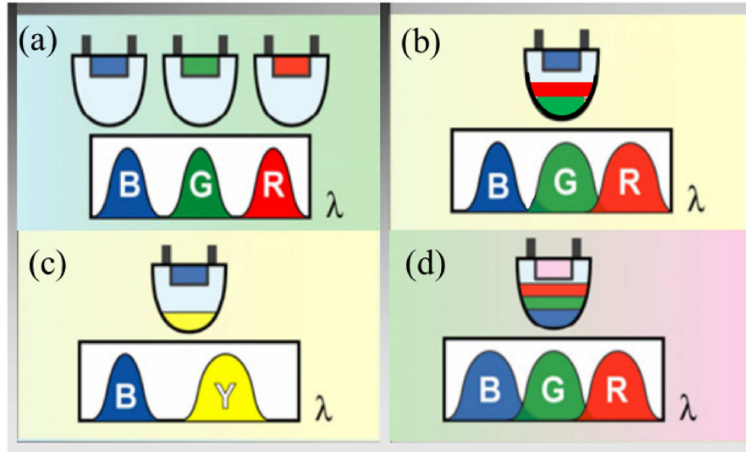**Figure 1.8:** *Scheme of the different approaches used to produce white light: (a) combination of red, green and blue LEDs, (b) pcLED, consisting of a blue LED and two color conversion phosphors, (c) pcLED, consisting of a blue LED and a single color (yellow-orange) conversion phosphor and (d) pcLED consisting of an UV LED and three color conversion phosphors.*

From the analysis of the different approaches, it is evident that

the ideal solution could be represented by the availability of a single solid-state LED which can cover the whole visible region. In this context, the development of RE-doped LEDs could represent a significant improvement but, in spite of the promising emission properties elucidated in section 1.1, the interest around REs still seems to be mainly confined to the field of phosphors.

1.3   Si photonics

It is well known that Si is the leading material in microelectronic technology; its wide diffusion is due to its abundance in nature, its low cost and its electrical, thermal and mechanical stability. Moreover, its oxide (SiO_2) is a very good insulator, which can well passivate surfaces and acts as an effective diffusion barrier.

One of the main fields where microelectronics is applied is the information technology. During these last years the aim of computer industry has been to fabricate increasingly performing microprocessors. This trend is depicted in the famous plots known as Moore's law, shown in figure 1.9, which has been able, until now, to predict future processor transistor density, and thus performance of computers expressed in million instructions per second (MIPS). This plot was born in 1965, just four years after the first planar integrated circuit, when Gordon E. Moore from Intel observed that the number of transistors that could be manufactured on a chip doubled every 18 months. Today, thanks to the technology development, it is possible to integrate a huge number of devices on a single microprocessor, which is able to perform the same number of instructions per second of a mouse brain. If processor development will continue with this rate, in the next 50 years a single processor will be able to perform a number of instruction per second comparable with the ones performed by all human brains together (figure 1.9)
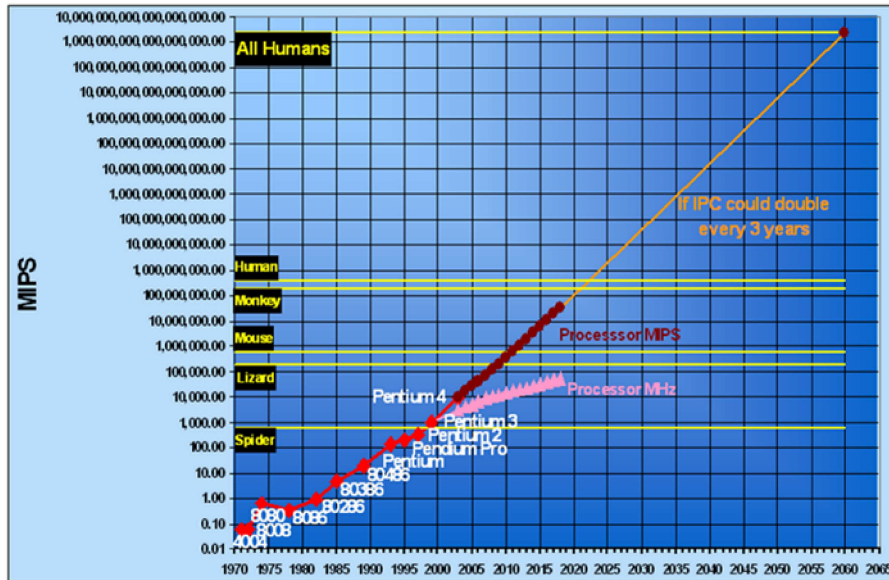
Figure 1.9: *Moore's law describing the growth of integrated circuits and their performance (in MIPS), compared with the ones of some life species' brains.*

To follow this trend and improve computational capacities, a more compact and performing computer technology is needed; as a consequence, much longer electrical connections are required in order to let all the components talk each other, and at larger scale to link different microprocessors integrated in the same circuit board. Today the total length of metallic interconnections in a microprocessor is more than 10 km and therefore many levels of metals are required. This dramatic increase of the total length of metallic connections leads to electromagnetic interferences causing power dissipation. This phenomenon is known as "interconnection bottleneck" and constitutes the most important limitation for further developments of microelectronics.

A possible solution to this problem is to move the technology from microelectronics to microphotonics, by replacing the electrical interconnections with optical ones for linking chip-to-chip and board-to-board [16]. Photons, in fact, do not suffer the same problems of metallic connections, having the possibility to travel at the light speed in the medium they pass through. A possible example of photonic device is the one proposed by IBM Research, shown in figure 1.10 [17]. This technology is capable of integrating a photodetector (red feature on the left side of the cube) and a modulator (blue feature on the right side of the cube) fabricated side-by-side with Si transistors (red sparks on the far right of the cube). Si photonic circuits and Si transistors are interconnected by nine levels of metal wires (shown in yellow).
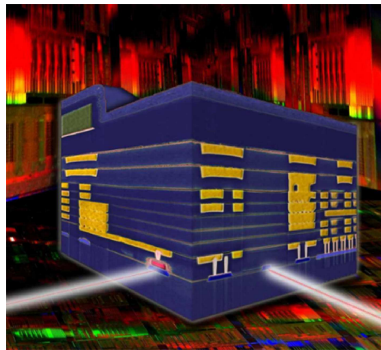
Figure 1.10: *Cross-sectional view of an IBM Si photonic chip combining optical and electrical circuits [17].*

Similarly to microelectronics, Si has all the characteristics to be used as the main material even in photonics. Indeed its high refractive index (n = 3.5) makes it a good medium through which light can be guided and transmitted: several low loss waveguides based on Si have been developed, using different approaches [18–20]. Moreover, Si based detectors, able to convert a light signal into an electrical one, have been realized [21–24]. Even if the fabrication of photonic passive devices,

including waveguides, detectors, etc., is well developed, a necessary step forward to apply Si in microphotonics, is certainly the realization of active devices, and in particular of light sources. A light source is a fundamental component in microphotonics because it can act as a generator of light-dark signals that can be associated to the logic value 1-0, giving the possibility to maintain the same logic of actual microprocessors.

In this context, despite its relevant properties, the main limit for Si applications in photonics is Si itself: indeed Si is a bad emitter and the fabrication of a Si-based light source is a hard task. The reason lies in its band diagram: Si in fact has an indirect band gap of 1.1. eV [25]. This means that the highest level in the valence band (Γ point) and the lowest level in the conduction band (X point) correspond to different k vectors, as shown in figure 1.11. As a consequence an electron-hole (e-h) radiative recombination requires some additional momentum, which can be given for instance by a phonon.

Therefore, the radiative recombination is a three-particle process, involving the e-h pair, a photon and a phonon (either absorbed or emitted): though it is not forbidden, it has a low probability. In fact, this process is characterized by a lifetime of more than 10 ms above 20 K [26, 27], which is much more longer than the typical lifetime of III-V semiconductors with direct band gap (100 ns). Consequently, Si shows a very low (10^{-6}-10^{-7}) quantum efficiency, which is several orders of magnitude lower than that of III-V semiconductors.

It is therefore necessary to find efficient strategies in order to realize efficient light emitting devices compatible with Si-based technology.

1.3.1 Si nanostructures as visible light sources

As discussed in the previous section, to fabricate a Si-based light source we have to solve the problem of light emission from bulk Si.

A first approach to overcome this limitation of Si is based on the
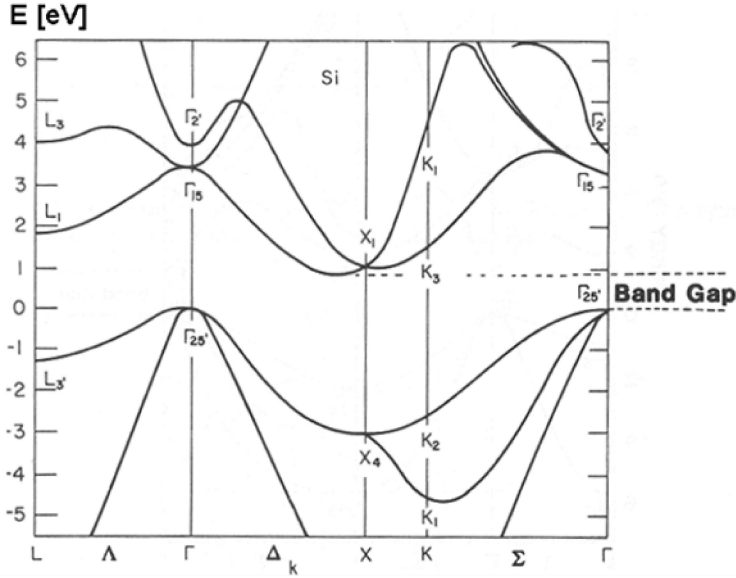
Figure 1.11: *Band structure of Si. The indirect band gap is clearly visible.*

synthesis of low dimensional systems. Electronic and optical prop-
erties of low dimensional systems deviate substantially from those of
bulk materials. Indeed, once a semiconductor structure is reduced to
nanometric size (1-10 nm), the electron and the hole become spatially
confined; as a consequence their wavefunctions from a Block type,
become confined and overlapped. In this situation, due to the bound-
ary conditions, only certain wavefunctions, with precise wavelengths,
can be supported by the material. Therefore the energies of the con-
fined particles become quantized; this picture can be described by the
model of a particle in a box. In this model the solution of the prob-
lem provides a mathematical connection between energy states and
the dimension of space: decreasing the volume or the dimensions of
the available space, the energy of the states increases, as schematically

shown in figure 1.12.
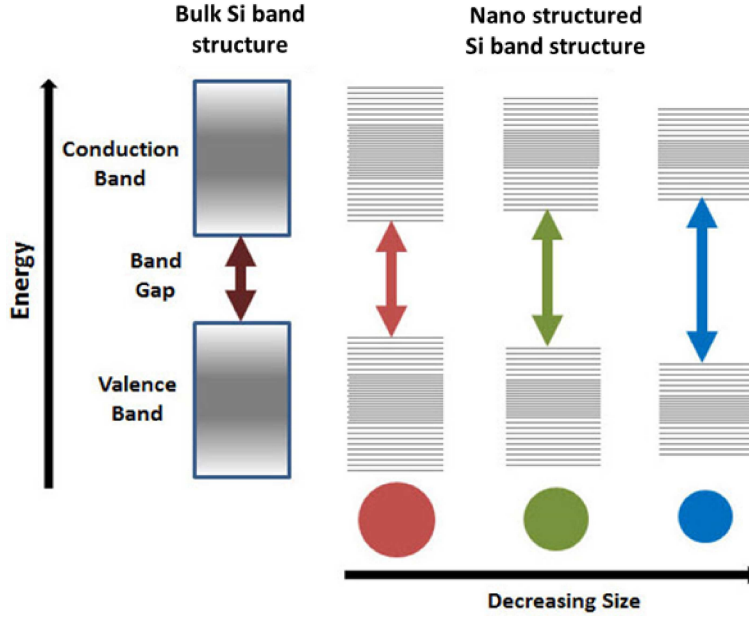
Figure 1.12: *Schematic representation of energy gap of bulk Si and nanostructured Si systems as function of their size.*

Another effect of quantum confinement is the increment of the probability of optical transitions. Indeed, due to the reduced size, the translational symmetry of the system is no more satisfied and, as a consequence, the crystal momentum is no more a good quantum number. This allows that no-phonon direct band to band transitions become more probable [28]. Furthermore, quantum confinement influences also the density of states (DOS): going from three-dimensional to zero-dimensional systems, DOS tends to resemble the Dirac's delta function, producing an increase in the probability of a photon to be emitted in an exciton recombination process.

Due to the peculiar properties of the quantum confined systems, Si nanostructures represent a promising approach for the fabrication of light emitting devices. Some of the most studied nanostructured systems are discussed below (figure 1.13):
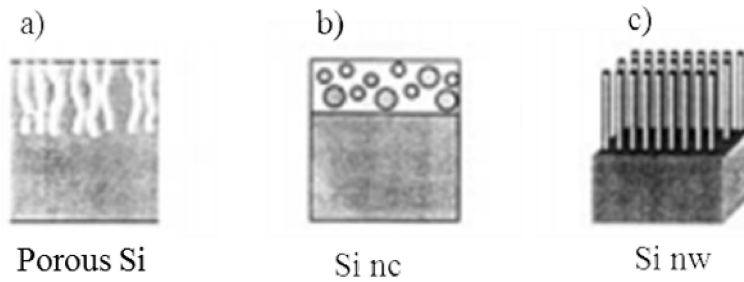
Figure 1.13: *Schematic representation of some low-dimensional Si structures: (a) porous Si, (b) Si nanoclusters and (c) Si nanowires.*

- **Porous Si** (figure 1.13a) has been studied since 1990. This system exhibits an intense room temperature photoluminescence (PL) emission in the visible range [29, 30], which allows LED fabrication. However porous Si has a series of disadvantages: a poor optical and mechanical stability and the difficulty of integration with Si processing technology because electrochemical etching is needed for its production.

- More recently, since the observation of optical gain [31], **Si nanocrystals (Si nc)** embedded in a SiO_2 matrix have attracted a strong interest in photonics (figures 1.13b and 1.14). The strong visible light emission of Si nc at room temperature and in particular its dependence on the nc size [32] and the mechanisms leading to photon emission are still the object of an intense scientific debate [33, 34].
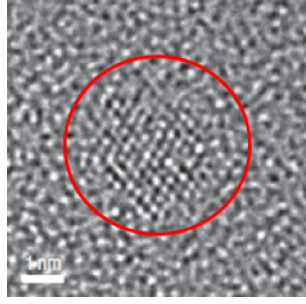
Figure 1.14: *High resolution transmission electron microscopy image of a single Si nc embedded in SiO$_2$ (evidenced by a red circle in the figure) [35].*

Typical PL spectra of Si nc embedded in SiO$_2$ are shown in figure 1.15a [36]. It is possible to observe a shift of the emission peak to higher wavelengths by increasing the Si nc size, in agreement with the quantum confinement theory. The structural features of Si nc embedded in a SiO$_2$ matrix allows also the electrical excitation of the system and Si nc-based LEDs have been realized [37]. An example of device is reported in figure 1.15b, where an emission microscopy (EmMi) image of an electroluminescent device based on Si-nc is shown. The EmMi image is in false colors, which are proportional to the intensity of the emitted light.

- Another recent approach to realize luminescent Si nanostructures is the fabrication of **Si nanowires (Si nw)**, shown in figures 1.13c and 1.16a. There are several fabrication methods to obtain Si nw, mainly based on two different approaches: top-down, in which Si nw are obtained onto the material through the combination of different technological processes (lithography, etching, etc.), and bottom-up, which consists in assembling chemically synthesized and well-defined nanoscale building
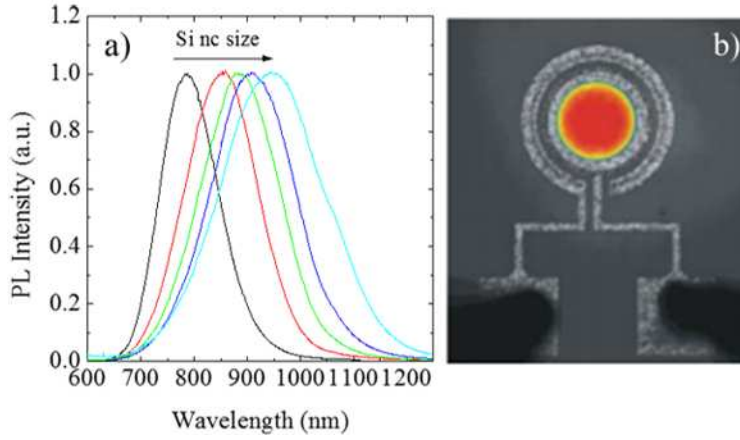
Figure 1.15: *(a) Normalized room temperature PL spectra of Si nc with different sizes. (b) EmMi image of a device containing Si-nc. Red area corresponds to the region emitting at the highest intensity [37].*

blocks. By controlling the synthesis parameters it is possible to control the dimension of the single Si nw, and the PL emission wavelength. In figure 1.16b the PL spectra of Si nw with different sizes are shown; figure 1.16c displays a photograph of the PL emission coming from a Si nw sample with a very high external quantum efficiency of 0.5% [38].

1.3.2   RE-doped Si-based materials for visible light emission

Although Si nanostructures themselves exhibit a tunable emission through the control of their size, it is difficult to obtain a precise control over the emission energy throughout the visible spectrum. One reason is that nc or nw surface states and defects limit the tunability range of these systems. Furthermore, since light emission from
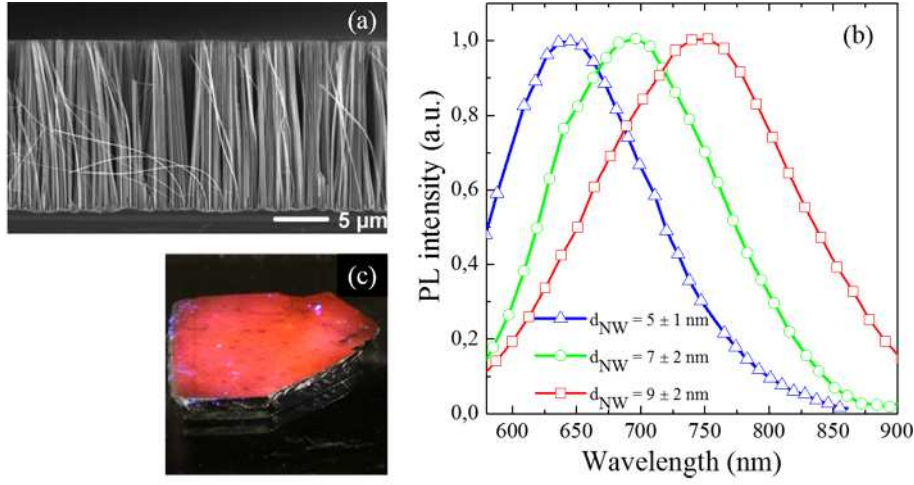
Figure 1.16: *(a) Cross sectional scanning electron microscopy image of Si nw [39]. (b) PL spectra of Si-nw samples having different sizes. (c) Photograph of a Si nw sample showing a bright PL emission visible by the naked eye [38].*

these materials strongly depends on composition and processing parameters, slight variations in the processing can lead to changes in the emission spectra. On the other hand, an alternative method to obtain specific and controlled emission energy is through the incorporation of RE dopants into Si-based materials. For obvious technological reasons, Si and Si oxides have been considered of particular interest and importance as host matrix for RE ions.

As discussed in section 1.2, the use of RE dopants to achieve specific color emissions for lighting has been previously applied in phosphor-based systems. For RE-doped Si-based materials much of the present work involves efforts to characterize the structural and optical properties of thin films, in order to optimize their performances. Among the various REs, Er has attracted a particular attention be-

cause of the coincidence between its intra-4f transition at 1.535 μm and the transparency window used for telecommunications [40]. However, the most critical application of REs is the fabrication of light sources; to this end, the demand to realize full-color light emission from Si-based materials extended technology interests to many other RE elements [41, 42]. For example, electroluminescence (EL) emission has been reported for Tb-implanted SiO_2 layers [43–45], with a power efficiency of 0.3% [46]. *Sun* and co-workers have observed strong EL from Gd-implanted SiO_2 [47], and *Prucnal* et al. have realized an Eu-doped LED fabricated through ion implantation of Eu into SiO_2 [48]. The authors have observed that this device exhibits both blue and red emissions (due to the presence of Eu^{2+} and Eu^{3+}) with the ability to switch between emissions from the two ions by varying the excitation current (figure 1.17).
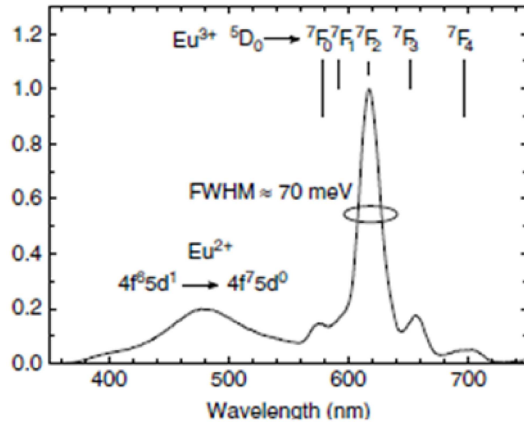
Figure 1.17: *Typical EL spectrum of an Eu-implanted LED [49].*

Furthermore there are reports about the EL from Ce- [50, 51], Eu- [52, 53], Gd- [54–61], Tb- [45, 62, 63], Tm- [50, 64, 65] and Yb-implanted SiO_2 layers [66–68]. The use of RE in Si-based material

is a very active research field; figure 1.18 gives a sketch of what is technically feasible with RE-doped Si-based materials.
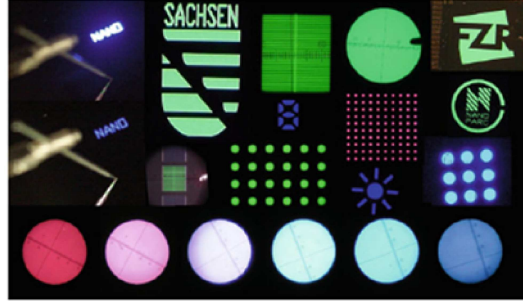
Figure 1.18: *Light emitting RE-implanted MOS structures with different layouts. The blue, green and reddish structures in the upper part of the figure originate from Ge-, Tb- and Gd-implanted LEDs. The lower row displays Eu-implanted LEDs, with different Eu concentrations processed under different annealing conditions [49].*

Despite the very interesting optical properties of RE-doped Si-based materials, one of the main limits to be overcome in order to achieve efficient emission is the low solubility of optically active RE ions. Indeed the solubility of RE ions in various Si materials is generally low due to the mismatch of ionic radii and the strong covalent bonding of the matrix network. Above a critical concentration, RE ions tend to form precipitates, which results in severe luminescence quenching through ion-ion interaction or by forming an optically inactive phase [41]. A possible solution to obtain high RE concentrations in Si-based materials is to synthesize RE compounds. For example, Eu silicates represent an attractive option to incorporate high Eu concentrations in order to achieve bright luminescence. Although the formation of pure Eu silicates requires annealing at temperatures higher than 1400 °C, mixed phase structures have been obtained by reactive sputtering of Si and $EuSi_2$ in Ar or Ar/O_2 atmospheres followed by

annealing at 900-1000 °C [69, 70]. A schematic of the ITO/EuSiO/Si EL device structure realized is shown in figure 1.19a, where the upper contact is made by a transparent conductive indium/tin oxide (ITO) layer. The EL spectrum, obtained by applying 30 V of bias voltage, shows broad spectral structure ranging from 400 to 800 nm and appears to the naked eye as white light (see figure 1.19b). The authors assigned this broad spectrum to the $4f^6 5d^2 \longrightarrow 4f^7$ transition of divalent Eu ions.
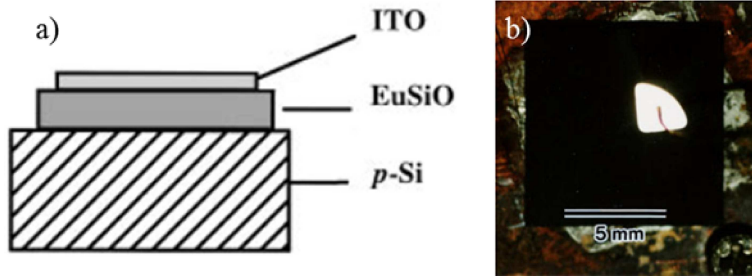
Figure 1.19: *(a) A scheme of the Eu silicate EL device structure. The luminescent Eu silicate layer and the ITO transparent layer are about 2 µm and 100 nm thick, respectively. (b) A photograph of the uniform white light emission from the device [70].*

Despite the above described results, application in photonics of RE-based materials still presents some unsolved problems: (i) Si-based materials are not an ideal host matrix, due to the low solid solubility of RE ions; (ii) RE silicates are basically insulating materials; (iii) synthesis processes of RE-doped Si-based materials fully compatible with Si technology have to be developed for future scaling in photonics.

1.4 Contents of this thesis

Aim of this thesis is to study novel approaches to fabricate Si-based materials which exhibit efficient and controlled emission of light in the visible range, for application in lighting and Si photonics, allowing to overcome some of the current limits described above.

In **Chapter 2** the structural and optical properties of SiOC thin films will be discussed. SiOC is a material fully compatible with Si technology, which exhibits a very broad and intense room temperature luminescence band, spanning almost all the visible range from 400 to 600 nm. It will be shown that the PL emission is ascribed to different emitting centers whose efficiency depends on the annealing temperature and ambient. The results suggest to consider SiOC a promising material for applications in Si photonics and in solid-state lightning.

A different approach to obtain Si compatible materials emitting light in the visible range will be proposed in **Chapter 3**, in which the structural and optical properties of Eu-doped SiO_2 and SiOC thin films will be shown. Performances of SiO_2 and SiOC layers as host matrices for optically active Eu ions will be compared. SiO_2 allows to observe room temperature light emission from both Eu^{2+} and Eu^{3+} ions, but in this matrix PL efficiency of both ions remains relatively low and quite far from the requirements for technological applications, mainly due to the extensive formation of Eu-containing precipitates. It will demonstrated that in a SiOC matrix Eu ions are characterized by a higher solubility than SiO_2. Furthermore, when incorporated in a SiOC matrix, Eu^{3+} ions are efficiently reduced to Eu^{2+}, producing a very strong room temperature PL emission peaked at about 440 nm, which is a wavelength of interest for blue LEDs fabrication. An energy transfer mechanism between SiOC matrix and Eu^{2+} ions, which increases the efficiency of photon absorption for excitation wavelengths shorter than 300 nm, will be demonstrated. Finally, bilayers consisting of two SiOC films doped with different Eu concentrations will be stud-

ied. With a proper choice of the annealing condition, these bilayers show an intense white emission at room temperature, characterized by high CRI values. These findings constitute a relevant progress towards the realization of efficient white light sources, which can be of great interest for applications in solid-state lighting. Furthermore, since SiOC is a material fully compatible with standard Si technology, Eu-doped SiOC layers can also be considered a highly interesting candidate for photonic applications.

Finally, in **Chapter 4** it will be shown how it is possible to overcome the limit of the low Eu solid solubility and therefore to incorporate a very large amount of Eu ions in Si-based materials, through the synthesis of Eu silicates. These materials have been studied in detail, by performing structural and optical characterization. Main results include the demonstration that divalent Eu silicates can be obtained with a process compatible with Si technology, starting from an Eu_2O_3 thin film deposited on a Si substrate. Eu silicates show an intense PL emission peaked at 590 nm, with an external quantum efficiency of about 10%, suggesting that this material can be a good candidate for photonic and lighting applications.

Chapter 2

Silicon oxycarbide (SiOC): an emitting material in the visible region

In this chapter a deep investigation of the chemical and optical proper-
ties of SiOC thin films synthetized by RF magnetron sputtering will be
presented. SiOC exhibits a very broad and intense room temperature
luminescence band spanning almost all the visible range from 400 to
600 nm. Optical analysis, as a function of the annealing temperature
and ambient, allowed us to ascribe this broad emission to two lumines-
cent centers emitting at 400 and 510 nm. The first one at 400 nm has
been assigned to defects centers, and in particular vacancies, formed
during an annealing process in O_2, while the second emission at 510
nm has been related to the presence of Si-C bonds, which are stabilized
after thermal treatments. These results indicate that with a proper con-
trol of the thermal annealing conditions, it is possible to continuously
tune the PL emission of SiOC from 400 to 500 nm. Finally it has been
demonstrated that the film refractive index variations as a function of
the annealing process are in agreement with the PL emission charac-

teristics of SiOC. Furthermore, refractive index measurements allow to gain information on the chemistry of the SiOC films after thermal treatments. On the basis of its chemical and optical properties, SiOC can be considered a potential material for applications in Si-photonics and in solid state lightning.

2.1 Introduction

As previously discussed in Chapter 1, the synthesis of Si nanocrystals (nc) embedded in a SiO_2 film is one of the most promising approaches for the development of Si-based light-emitting devices operating in the visible region [31]. Indeed, this material is compatible with the standard Si technology and is characterized by a high photoluminescence (PL) and electroluminescence (EL) efficiency at room temperature [71, 72]. The size-dependent emission of Si nc in SiO_2 is usually located in the red-near IR spectral region ($\sim$ 1.4-1.8 eV) even for the smallest nc sizes [72]. Therefore systems emitting at higher energies require alternative approaches or different materials.

Si oxycarbide (SiOC) has been widely studied in the last years because it could provide a suitable heat-resistant material for high-energy luminescence as well as white light applications. SiOC is a generic formula used to denote a chemical structure in which Si is simultaneously bonded with C and O and in which the O/C atomic ratio can be varied within a wide range. The incorporation of C in SiO_2 implies the replacing of some O atoms, which are only twofold coordinated, with C atoms, which can be fourfold coordinated. This increased bonding per anion is expected to strengthen the molecular structure of the glass network and thereby to improve its thermal and mechanical properties. Indeed SiOC is studied due to applicability in Si microelectronic devices as low-k dielectric, etch-stop and passivation layers [73].

In terms of optical properties SiOC shows broad PL emission bands, that cover the entire visible range from 350 to 800 nm. As a consequence, SiOC seems to be one of the promising candidates for white light device fabrication. The origin of PL emission from SiOC films is not clear; generally it consists of multiple contributions, which have been attributed to different centers, including Si-C bonds in C-containing Si (or SiC) nanoclusters [74, 75], C- and Si-related O defects [76], defects at the SiC/SiO_2 interface [77], neutral O vacancies [78]. Furthermore a strong dependence of SiOC PL emission on the growth conditions was observed. Indeed there are several techniques to synthesize light emitting SiOC layers: mainly C implantation in SiO_2 [79–81], chemical vapor deposition (CVD) [74], rf magnetron sputter deposition [82], sol-gel technique [83] and successive carbonization/oxidation treatment of porous Si [84].

Two PL bands at 410 nm (violet band) and 470 nm (blue band) were observed by *Zhuge* et al. [85] in SiOC films. The Si- and C-codoped SiO_2 films were prepared by dual ion beam sputtering. The authors observed that the intensity of the two PL bands is strongly dependent on the annealing temperature. When the annealing temperature is above 800 °C, Si reacts with C atoms to form Si-C bonds, changing the stoichiometry of the matrix and producing O defects. Indeed they ascribed the 470 nm PL band to the neutral oxygen vacancy ($O_3 \equiv$ Si-Si $\equiv O_3$). To explain the origin of the 410 nm PL band two possibilities have been put forward by the authors: C clusters, whose existence remains without clear evidences and the defects in a region where Si-C bonds are formed. CVD is another technique widely used to synthesize SiOC films. *Seo* et al. [74] realized C-doped Si-rich Si oxide (SRSO:C) films using a high-vacuum electron cyclotron resonance plasma enhanced CVD system. Figure 2.1 shows the evidence of an intense and broad luminescence from SRSO:C due to presence of high C concentration. The authors observed that the emission intensity depends on the excess Si and C concentration and annealing conditions.

When the C/Si atomic ratio is 0.9, the PL intensity from SRSO:C film has a maximum and it is more intense than the one observed from a C-free SRSO, probably due to the formation of Si-C bonds which emit at around 2.3 eV (540 nm).
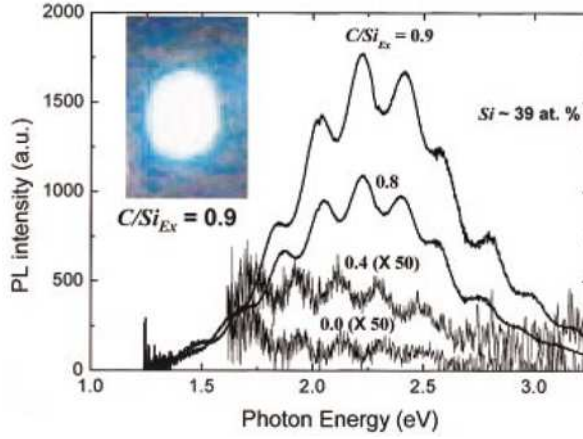
Figure 2.1: *PL spectra of SRSO:C film with Si content of 39% and different C/Si atomic ratio. The inset is a camera image of the PL observed in the film with C/Si_{ex} = 0.9 [74].*

Gallis et al. [76] realized SiOC film by high temperature CVD. They observed an intense broad emission band with a maximum at around 440 nm, visible to the naked eye under bright room conditions (figure 2.2). A dependence of PL intensity on the annealing conditions was found. This PL behavior was correlated with the presence of C-related O defect centers, demonstrating that these defects may play an important role in white light emission.

Rodriguez et al. [75] provided a detailed microstructural and optical analysis of SiO_2 layers sequentially implanted with Si and C and then annealed. These analyses allowed them to characterize the different bands arising in the PL spectra, which are responsible for the

intense white emission observed at high implanted doses (for Si atomic excesses higher than 10%). These bands have been assigned to the emission from Si-nc and C-containing amorphous nanoparticles. At lower implanted doses the PL spectra show only one band, in addition to the well-known red one related to the Si-nc. The authors also observed that C implantation strongly affects the growth kinetics of Si-nc; indeed, from the transmission electron microscopy (TEM) image reported in figure 2.3 it is clear that the presence of C inhibits Si-nc formation in the region of the C-implanted profile (region 2).
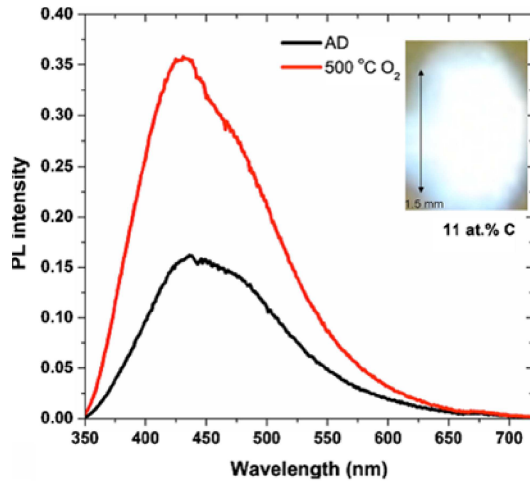
Figure 2.2: *Room temperature PL spectra of a $SiC_{0.32}O_{1.56}$ film as deposited and annealed in O_2 at 500 °C. The inset is a camera photo of the PL observed in the annealed sample [76].*

SiOC was also fabricated by carbonization of porous Si in acetylene flow followed by wet oxidation. In samples grown with this technique, *Ishikawa* et al. [84] observed a PL emission in the 400-700 nm range. They have shown that PL color, in the range of blue-white and yellow-white, can be controlled by selecting the porosity of the

starting porous Si as well as the carbonization and oxidation temperatures. Low-temperature oxidation resulted in bluish light emission in lower porosity series, while high-temperature oxidation promoted yellow-white light emission. The maximum PL intensity was observed after oxidation at 800 °C. It was shown that white PL from SiOC has blue and yellow-white PL bands originating from different light-emitting centers. The origin of blue PL is attributed to defects in SiO_2. Some trap levels at the interface between C clusters and SiO_2 are suggested to be the origin of the yellow-white light.
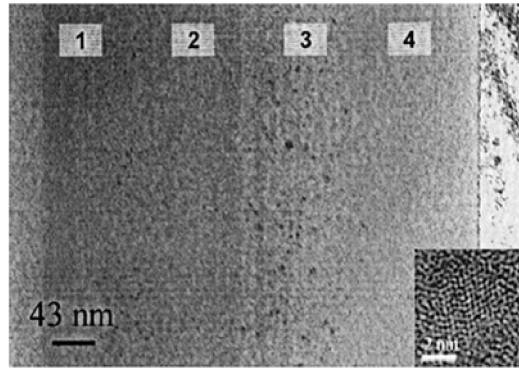
Figure 2.3: *Cross section TEM image of a 30 Si at.%, Si+C implanted and annealed SiO_2 sample. The image shows the presence of a buried layer with darker contrast and free of crystalline precipitates (region 2), which corresponds to the maximum of the C-implanted profile. Si nc are observed in regions 1 and 3. Region 4 corresponds to the SiO_2 layer without precipitates. The inset shows a high-resolution TEM image of a Si nc from region 1 [75].*

From the point of view of applications, the observed blue-white emission of SiOC is usually strong enough to be seen by the naked eye under bright room conditions. *Gebel* et al. [86] also obtained some positive results for the electrical excitation of SiOC films. Further-

more, as will be discussed in detail in Chapter 3, SiOC can be also an interesting host material for rare-earth ions, including Er [87] and Eu [88].

All these features make SiOC a very promising material to fabricate visible light emitting sources. However some open points concerning the nature of SiOC PL emission need further investigations to improve PL emission intensity and color control, which are very important parameters for the fabrication of light emitting devices based on SiOC.

2.2   Growth and characterization of SiOC thin films

All the thin films studied in this thesis have been synthesized by using rf magnetron sputtering, which is a technique fully compatible with Si technology and it is widely used in microelectronic industry. The system is shown in figure 2.4a; it mainly consists of an ultra-high vacuum (UHV) chamber with a base pressure of about 10^{-9} mbar, a load-lock, with an independent pumping group, for sample loading, and three 4-inches diameter, water-cooled targets, located at the bottom of the chamber and arranged in a confocal geometry (figure 2.4b). SiOC thin films have been deposited on 5-inches diameter Si wafers in an Ar atmosphere at $5 \cdot 10^{-3}$ mbar by co-sputtering SiO_2 and SiC targets; substrates were heated at 400 °C and held in rotation at 50 rpm to guarantee a good film uniformity. The rf power applied to SiO_2 and SiC targets (figure 2.4c) was 500 and 100 W, respectively.

After deposition the films have been thermally treated at temperatures ranging from 600 to 900 °C for 1 h in O_2 or N_2 atmosphere by using a conventional horizontal furnace.

The SiOC films obtained have a thickness of about 190 nm, as measured by both ellipsometry and cross sectional TEM. The refractive
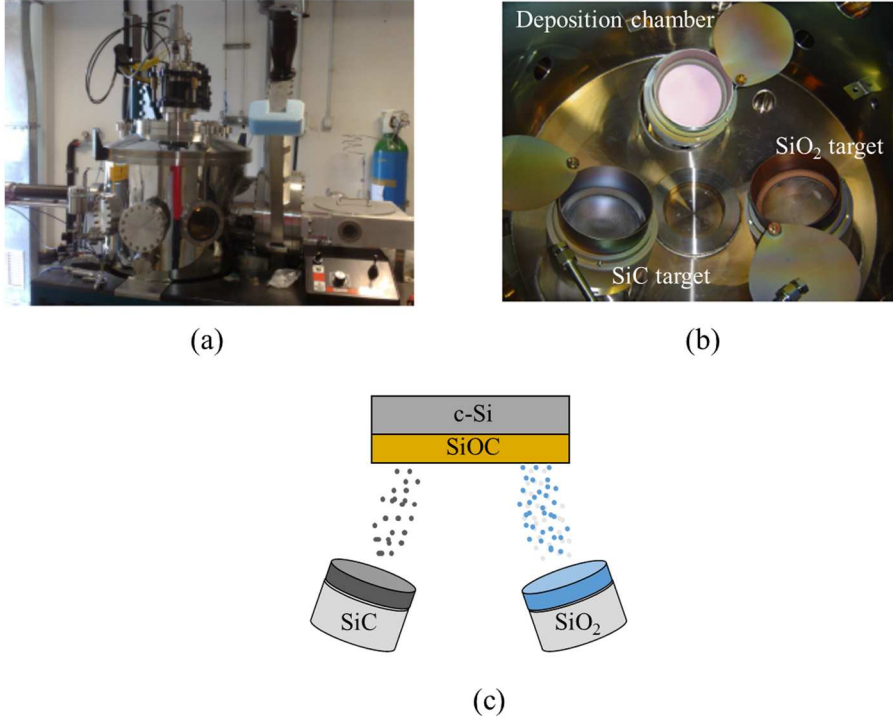
(a)   (b)

(c)

Figure 2.4: *Pictures of the rf-magnetron sputtering system used for SiOC thin film growth: (a) a general view of the apparatus and (b) the three targets located at the bottom of.the chamber. (c) Schematic representation of SiOC thin films deposition through the rf cosputtering of SiC and SiO$_2$ targets.*

index of SiOC samples was measured using an ellipsometer equipped with a He-Ne laser operating at 632.8 nm. The C content of the film is about 5 at.%, as obtained by Rutherford backscattering spectrometry (RBS) measurements, performed by using a 2 MeV He^+ beam in random configuration, with the detector placed at an angle of 165° with respect to the incident beam.

Photoluminescence (PL) measurements have been performed at room temperature by pumping with the 325 nm line of a He-Cd laser. The pump power was about 3 mW and the laser beam was chopped through an acousto-optic modulator at a frequency of 55 Hz. As shown in the experimental set-up sketched in figure 2.5, the laser beam is driven and focused on the sample thanks to mirrors and lens systems. The PL signal emitted from the sample is collected and analyzed by a single grating monochromator and detected with a Hamamatsu visible photomultiplier. Spectra have been recorded by a lock-in amplifier using the acousto-optic modulator frequency as a reference.

PL lifetime measurements have been performed by monitoring the decay of the luminescence signal at fixed wavelengths. The pulsed excitation source has been fixed at 300 nm, provided by the second harmonic from a Spectra Physics 3500 dye laser, pumped with a Nd^{3+}:YAG laser. The system have a temporal resolution of 80 ps.

Photoluminescence excitation (PLE) measurements in the 250-475 nm range were performed by using a FluoroMax spectrofluorometer by Horiba, which use a Xe lamp, coupled with a monochromator, as excitation source. The system allows to measure the emission spectra at different excitation wavelengths. PLE spectra can be obtained by considering the PL intensity at a fixed emission wavelength or the integrated PL intensity in a fixed wavelength range. All the spectra have been measured at room temperature and corrected for the system spectral response.
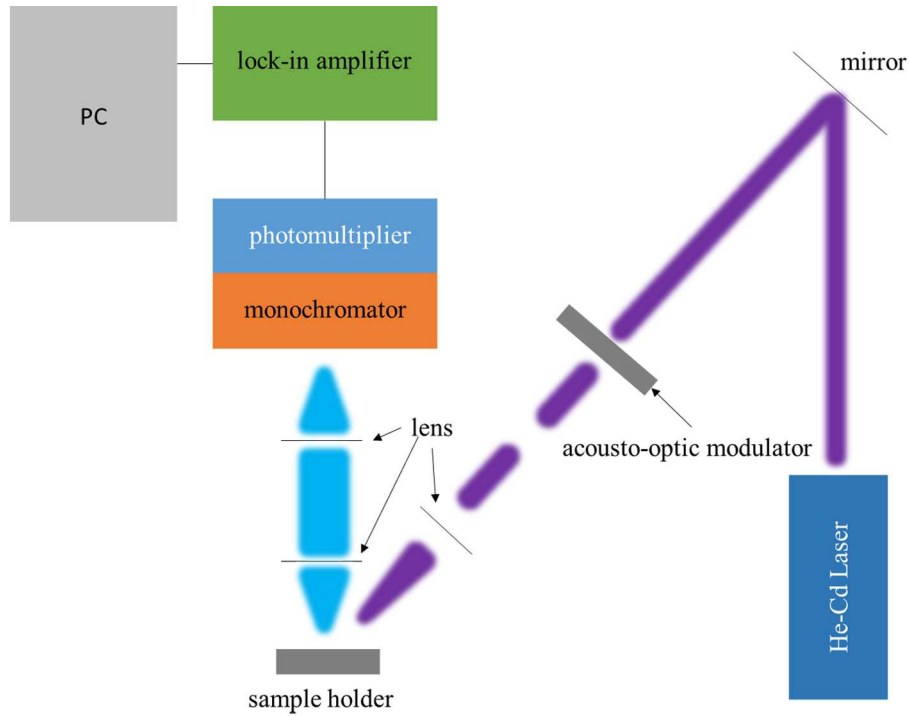
Figure 2.5: *Scheme of PL set-up used: the laser beam from a He-Cd laser is focused on the sample with a lens. The beam is pulsed at a frequency of 55 Hz by an acousto-optic modulator. The emitted PL signal is collected and focused on a single grating monochromator and detected with a Hamamatsu visible photomultiplier.*

2.3   Visible PL from SiOC thin films

The SiOC films deposited by sputtering have been thermally treated to optimize the stoichiometry and remove eventual defects which could act as non-radiative de-excitation centers and limit the efficiency of the optical emission. We have investigated the influence of annealing temperature and ambient on the PL properties of SiOC films. In figure 2.6 the room temperature PL spectra of as-deposited and thermally annealed SiOC films, obtained by exciting with the 325 nm line of a He-Cd laser, are reported. Figures 2.6a and 2.6b refer to samples annealed in N_2 and O_2 atmosphere, respectively, the explored temperature range is 600-900 °C and the duration of all the processes is 1 h. It is evident that the conditions of the thermal treatment strongly influence the optical properties of the films. In particular, both the intensity and the shape of the PL peaks markedly depend on the ambient and on the temperature of the thermal process. More in detail, spectra of N_2-annealed samples (figure 2.6a) are generally redshifted and broader with respect to those of samples annealed in O_2 (figure 2.6b). Moreover, while the PL signal of samples annealed in O_2 ambient is maximized at 900 °C, that of N_2 annealed samples is maximized at 750 °C.

In order to better understand the nature of the observed emission, figure 2.7 compares the PL spectrum of an as-deposited film (black line) and those measured in samples annealed in N_2 (red line) or O_2 (blue line) ambient at the same temperature of 900 °C. All spectra have been normalized to allow an easier comparison of the shape. The spectrum of the as-deposited sample appears quite broad, indicating the presence of different contributions to the PL signal originating from multiple luminescent centers. The complex nature of the PL emission of SiOC films can be better understood by analyzing the PL peaks of the annealed films. Indeed, after annealing in N_2 atmosphere, a peak at 510 nm becomes predominant, although it is still visible a
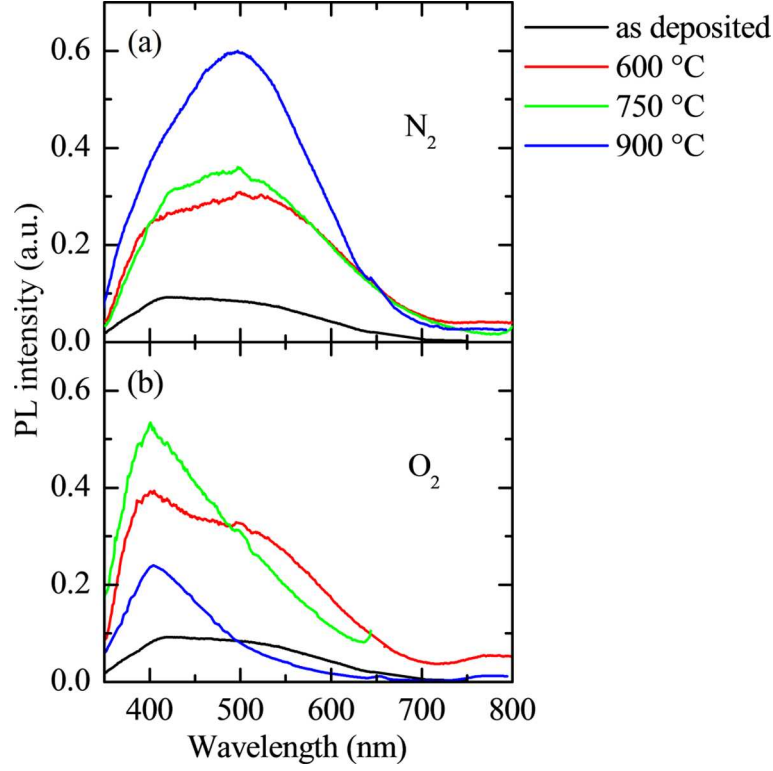
Figure 2.6: *Room temperature PL spectra for SiOC films as deposited and annealed in the temperature range 600-900 °C for 1 h (a) in N_2 ambient, and (b) in O_2 ambient.*

shoulder at 400 nm. In contrast, after annealing in O_2 atmosphere, the maximum of the band is found at 400 nm and the component at 510 nm is almost completely quenched.
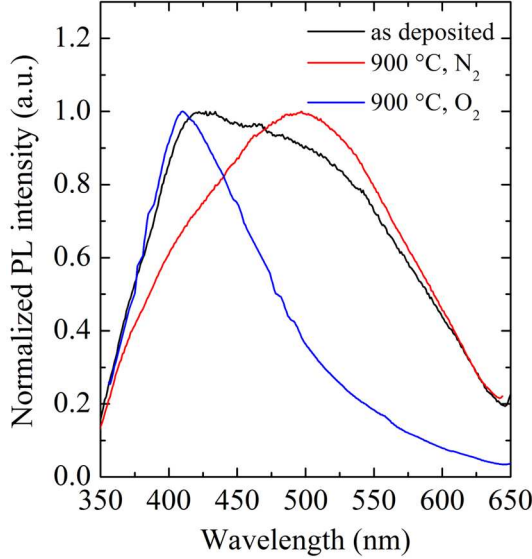
Figure 2.7: *Comparison between the normalized PL spectra of SiOC films as deposited and annealed at 900 °C in N_2 and in O_2 ambient.*

This behavior suggests the presence of at least two different luminescent centers in SiOC films, producing PL signals peaked at 400 and 510 nm. In particular, the broad nature of the PL spectrum of the as-deposited sample indicates that the two luminescent centers coexist and have a very similar efficiency, while the thermal treatment leads to the prevalence of one of them, depending on the annealing conditions.

The behavior of the two components of the PL emission of SiOC films, as a function of the annealing temperature for both N_2 and O_2 processes, can be analysed by plotting their integrated intensity, obtained by the fitting procedure employing Gaussian peaks described

in figure 2.8. The figure shows the spectrum of the as-deposited sample (black line), which has been well fitted by a curve (green line) obtained by summing two Gaussian curves peaked at 400 nm (blue line) and 510 nm (red line).
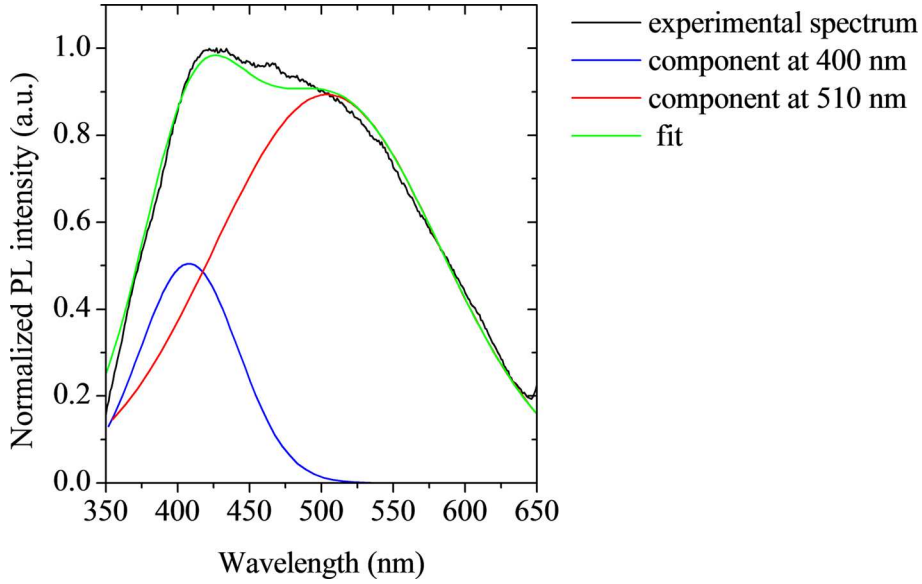
Figure 2.8: *PL spectrum of a SiOC film as deposited (black line) and its fit (green line) given by the sum of two Gaussian curves peaked at 400 nm (blue line) and 510 nm (red line).*

The integrated PL intensity as a function of the annealing temperature for the two components of the PL signal of SiOC films is reported in figure 2.9. For processes performed in N_2 atmosphere (figure 2.9a) the prevalent PL band is the one at 510 nm and its intensity (plotted as red line and circles) continuously increases with increasing the annealing temperature, while the intensity of the component at 400 nm (blue line and circles) remains quite low and almost constant throughout the explored temperature range. In contrast, for samples

annealed in O_2 atmosphere (figure 2.9b), the prevalent PL band is the one at 400 nm and its intensity has a maximum at 750 °C and decreases at higher temperatures, while the component at 510 nm has a maximum at 600 °C and decreases at higher temperatures, being almost completely quenched at 900 °C.
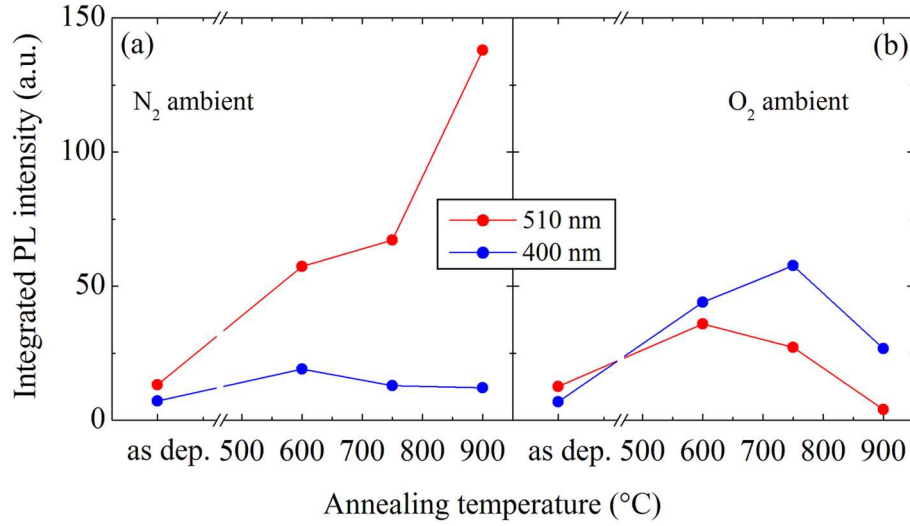
Figure 2.9: *Integrated intensity as a function of the annealing temperature for the two components of the PL signal of SiOC films annealed (a) in N_2 ambient, and (b) in O_2 ambient. The red circles refer to the component at 510 nm, the blue ones to the component at 400 nm.*

To obtain more information on the nature of the two luminescent centers, PL excitation spectroscopy measurements on SiOC samples annealed at 900 °C have been performed. The PLE intensity shown in figure 2.10, obtained by integrating the emission spectra recorded as a function of the excitation wavelength in the 250-370 nm range, is deeply influenced by the annealing environment. In particular, for the sample annealed in N_2, the integral PL intensity is almost constant

between 250 and 270 nm and then steeply drops by increasing the excitation wavelength, while for the sample annealed in O_2 it monotonically decreases with increasing wavelength.
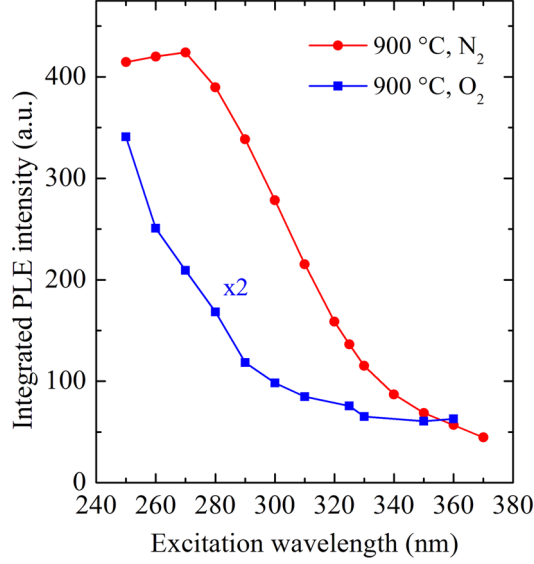
Figure 2.10: *Room temperature PLE intensity obtained by integrating the PL spectra recorded as a function of the excitation wavelength in the range 250-370 nm for SiOC films annealed at 900 °C in N_2 (red circles and line), and O_2 (blue squares and line, multiplied by a factor of 2).*

In addition, PL lifetime measurements have been performed on the samples annealed at 900 °C in O_2 and N_2 ambient, by selecting as emission wavelength 400 and 510 nm, respectively. As shown in figure 2.11, the decay curves are not single-exponential, therefore the values of the decay-time τ has been obtained by considering the time at which the PL signal is $1/e$ of the value observed at the laser shut-off. The τ values are 1.9 and 11.2 ns for the emission at 400 and 510, respectively, which confirms the different nature of the two emitting

centers.
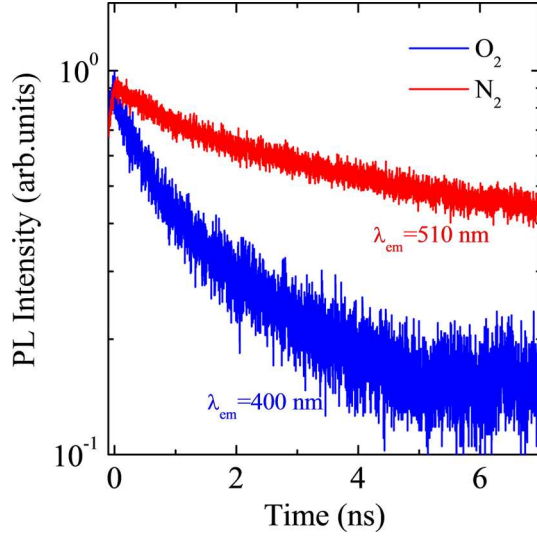
Figure 2.11: *Room temperature PL time-decay curves of SiOC films annealed at 900 °C in O_2 (blue line) or N_2 (red line) ambient, measured at 400 and 510 nm, respectively.*

On the basis of the data shown in figures 2.6-2.11 it is possible to reasonably conclude that the peak at 510 nm is due to the presence of Si-C bonds [74, 75], while the peak at 400 nm can be assigned to luminescent defects, such as oxygen vacancies [76, 78, 84]. Indeed, when SiOC films are annealed in N_2 atmosphere, free C and Si atoms, or Si-C complexes, increase their mobility and a partial ordering of the film structure occurs, leading to the formation of optically active Si-C bonds. The increase of these bonds concentration, as a function of the annealing temperature, corresponds to an increase of the PL signal at 510 nm, shown in figure 2.9a. The evidence that the system becomes more optically efficient at higher temperatures confirms that the PL at 510 nm cannot be assigned to defect centers, further supporting its

assignment to Si-C bonds, in agreement with the results obtained by *Zhuge* et al. [85].

On the other hand, by increasing the annealing temperature of O_2-treated samples, Si-C bonds emission intensity decreases because the oxidation of SiOC films implies a decrease of the C concentration into the film. Indeed, as depicted in figure 2.12, during the annealing O_2 diffuses inside the sample and reacts with the C atoms to form volatile CO or CO_2 molecules which can therefore escape from the sample, leaving it depleted in C [89]. This process also leads to the formation of vacancies into the film.
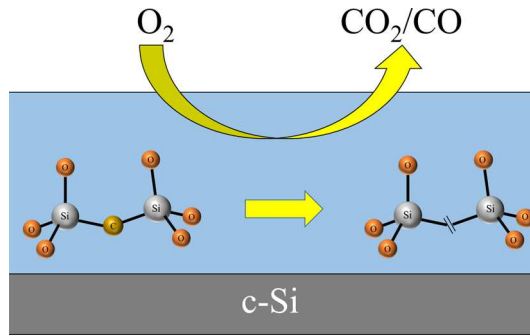
Figure 2.12: *Schematic view of the oxidation process of SiOC films under O_2 exposure. O_2 reacts with the C present in the film and forms volatile species such as CO or CO_2, leaving the film less rich in C and with the presence of vacancies.*

We propose that the origin of the 400 nm band may correlate with Si-O-C defects like Si or C dangling bonds during the thermal treatment which are known to be present in the SiOC system [76]. Similar PL emission originating from Si-O-C complex has been previously observed in C-implanted SiO_2 film [86] and amorphous SiOC film [76]. Furthermore, the quenching of the emission at 400 nm for high annealing temperature (figure 2.9), in agreement with the defect-nature

of this emission, is due to the recovery of the chemical luminescent defects of the film induced by the thermal treatment, leading to the formation of a nearly stoichiometric SiO_2 layer.

In order to have an indication on the structural modifications occurring during the annealing, we performed ellipsometric measurements of the refractive index at 632.8 nm of both as-deposited and annealed SiOC films. Figure 2.13 shows the evolution of the refractive index as a function of the annealing temperature for SiOC films treated in N_2 or O_2 ambient.
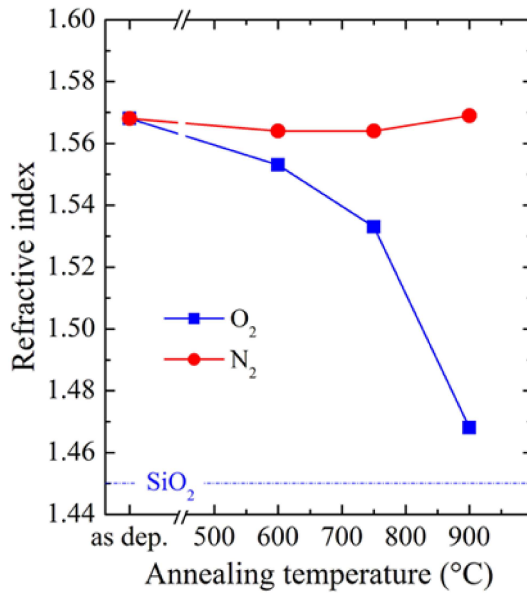
Figure 2.13: *Refractive index, measured at 632.8 nm, as a function of the annealing temperature for SiOC films annealed in N_2 (red circles and line), and O_2 (blue squares and line). The refractive index of pure SiO_2 is indicated by a blue dash-dotted line.*

The as-deposited sample has a refractive index of about 1.57, which

reflects its low C content (pure SiC refractive index is about 2.60 [90], while pure SiO2 refractive index is about 1.45 [91]). For annealing in N_2 atmosphere (red line and circles), the refractive index is almost constant throughout the explored temperature range (from room temperature up to 900 °C), indicating that the stoichiometry does not change during the annealing process, in agreement with the conclusions drawn on the basis of the above discussed PL data. In contrast, after annealing in O_2 atmosphere (blue line and squares), the refractive index decreases with increasing the annealing temperature. This corresponds to a change in the sample stoichiometry, and in particular to a variation of the C content in the SiO_2 matrix, which is in agreement with the above described oxidation process (figure 2.12). Increasing the annealing temperature, oxidation rate increases too, and the final result is a deep change of the stoichiometry of SiOC samples, leading to a continuous reduction of the refractive index, towards the typical SiO_2 value of 1.45, indicated in figure 2.13 by a dash-dotted blue line. The variation of the refractive index of SiOC films annealed in O_2 is in full agreement with the optical properties described in figures 2.6-2.11, demonstrating the strong correlation between structural, chemical and optical properties of SiOC.

A confirmation of the above picture concerning the nature of the PL emission in SiOC films has been obtained by analyzing the shape of the PL spectra of samples annealed at 900 °C in N_2 as a function of the time of air exposure after film synthesis. In figure 2.14 the normalized spectra of the same sample after one day, three months and 18 months are reported. It can be noted that a shoulder, evidenced in the figure by a black circle, appears on the short wavelength side of the aged samples. In agreement with the data of figure 2.7-2.9, this modification of the PL spectrum of SiOC films can be ascribed to an increased contribution of the defects, peaked at 400 nm. Indeed leaving the sample for a long time in contact with air, O_2 can react with the SiOC leading the formation of vacancies (see figure 2.12) with

consequential increase of the emission peaked at 400 nm. This result confirms the ambient-dependent nature of the luminescence centers of SiOC described above.
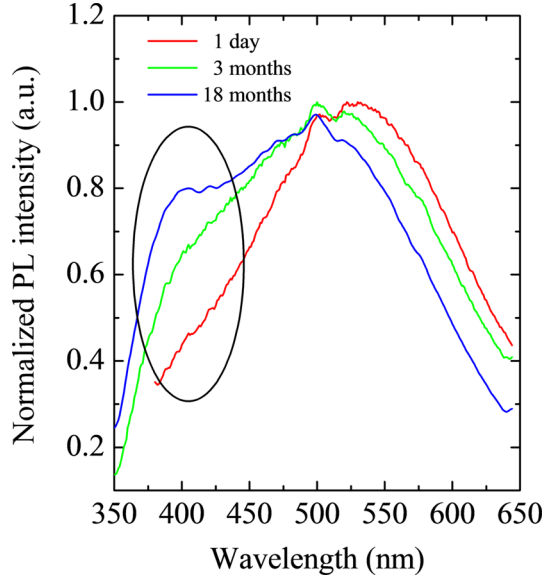
Figure 2.14: *PL spectra of 1 day (red line), 3 months (green line) and 18 months (blue line) aged SiOC films exposed to the air at room temperature, after thermal treatments at 900 °C in N_2. The black circle evidences the increase of PL contribution of the vacancies formed due to the exposure to atmospheric oxygen.*

In figure 2.15 a schematic representation of the SiOC emission mechanisms is depicted. The figure shows a scheme of the energetic levels of the two luminescent centers, Si-C bonds and vacancies. After the 325 nm excitation (black line) the system can relax non-radiatively (dashed arrows) to the lowest excited level of Si-C (red line) or of vacancies (blue line). With their typical lifetime of the order of ns (see figure 2.11), the excited levels of Si-C and vacancies can relax

to their ground states emitting a photon at 400 (blue arrows) or 510 (red arrows) nm. In the case of the as-deposited sample, the two luminescent centers coexist and the two processes depicted in figure 2.14 both occur with a similar efficiency, while in annealed samples the nature of the ambient determines the prevalence of one process with respect to the other. This picture is in agreement with the broad nature of the as-deposited spectrum and the thermal evolution of SiOC PL emission shown in figures 2.6 and 2.7.
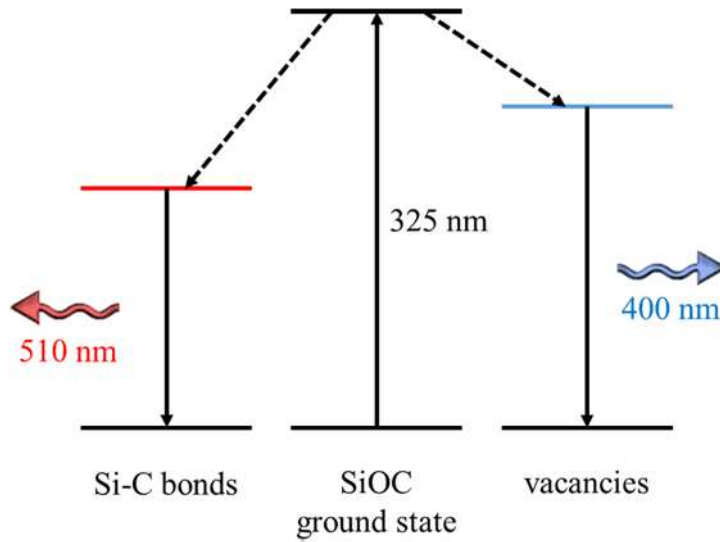
Figure 2.15: *Schematic view of the two different mechanisms populating the energetic levels formed after N_2 and O_2 annealing. An excitation photon at 325 nm excites the film which relaxes by emitting a photon at 510 or 400 nm.*

2.4   Conclusions

The intense visible emission of SiOC layers has been studied and its dependence on the thermal annealing parameters elucidated. In particular, the presence of two different emitting centers, one related to the presence of Si-C bonds, the other associated to structural defects, has been evidenced and the experimental conditions leading to the prevalence of one contribution with respect to the other have been identified.

The broad and tunable emission of SiOC in the visible range is bright enough to be visible by the naked eye. These optical characteristics, in combination with the full compatibility of SiOC films with Si technology, make this material potentially very interesting for applications in photonics (as the active medium in Si-based light emitting devices) or in lighting technology for LED fabrication.

Chapter 3

Eu-doped SiOC: a new approach for tunable and efficient light emission in the visible range

Eu-doped SiO_2 and SiOC thin films have been synthesized by using an UHV magnetron sputtering system. The comparison of the performances between SiO_2 and SiOC layers as host matrices for optically active Eu ions is presented.

A SiO_2 matrix allows to observe room temperature light emission from both Eu^{2+} and Eu^{3+} ions, owing to a proper tuning of the thermal annealing process used for the optical activation of the rare earth. However the photoluminescence (PL) efficiency of both ions remains relatively low and quite far from the requirements for technological applications, mainly due to the extensive formation of Eu-containing precipitates. A detailed study by transmission electron microscopy allowed us to analyze and elucidate the clustering process and to find suitable strategies for minimizing it.

To overcome the clustering phenomenon, substitution of SiO_2 matrix with a SiOC one has been performed. In fact, Eu ions are characterized by an enhanced solubility in this matrix and, as a consequence, Eu precipitation is strongly reduced. Furthermore, when incorporated in a SiOC matrix, Eu^{3+} ions are efficiently reduced to Eu^{2+}, producing a very strong room temperature PL emission peaked at about 440 nm. Eu^{2+} ions benefit also of the occurrence of an energy transfer mechanism involving the matrix, which increases the efficiency of photon absorption for exciting wavelengths shorter than 300 nm. We evaluate that Eu doping of SiOC produces an enhancement of the PL intensity at 440 nm accounting for about a factor of 250 with respect to Eu-doped SiO_2.

Finally, bilayers consisting of two SiOC films doped with different Eu concentrations have been grown. A proper choice of the annealing temperature allows to avoid Eu diffusion and clustering, so that each layer holds its optical properties. Under these conditions, the bilayer allows to take advantage of the dependence of the PL peak position on the Eu concentration, so that an intense white emission is obtained at room temperature.

These findings constitute a relevant progress towards the realization of efficient white light sources, which can be of great interest for applications in solid-state lighting. Furthermore, since SiOC is a material fully compatible with standard Si technology, Eu-doped SiOC layers can also be considered a highly interesting candidate for photonic applications.

3.1   Optical and structural properties of Eu

In Chapter 1 we have discussed the optical properties of rare earth (RE) ions, which make them very interesting for several practical applications. Usually, the most common valence state of REs in solids is the trivalent one, but Eu can exist both in its trivalent (Eu^{3+}) and divalent (Eu^{2+}) oxidation state. Figure 3.1 shows the Eu electronic energy levels for both oxidation states. The electronic configuration for the trivalent ion is $4f^6 5s^2 5p^6$, while that of the divalent ion is $4f^7 5s^2 5p^6$.

In the trivalent state 4f electrons are not the outermost ones and are shielded from external fields by two other electronic shells. As a consequence, when an Eu ion is introduced into a solid matrix, the 4f electrons are only weakly perturbed by the charges of the surrounding ligands. Therefore, many of the spectroscopic properties of Eu^{3+} ions do not depend on the matrix in which they are introduced and are expected to be understood from considerations about the free ions. A typical emission spectrum of Eu^{3+} is reported in figure 3.2, which shows different sharp peaks in the 500 - 750 nm region. In particular the spectrum has a maximum at around 620 nm, corresponding to the $^5D_0 \longrightarrow {}^7F_2$ optical transition (see figure 3.1). For Eu^{3+} the intra-4f shell transitions are electric dipole forbidden, resulting in a low emission intensity and quite long decay lifetime (of the order of ms).

An efficient optical excitation would require the promotion of an electron into the 5d shell (which is not dipole forbidden) followed by a radiative transition of the system back to the ground state: this is the case of Eu^{2+}. The most common oxidation state of Eu in solids is the trivalent one, but in some conditions Eu can be stabilized into the divalent state. For Eu^{2+} ions the energy separation between the $4f^7$
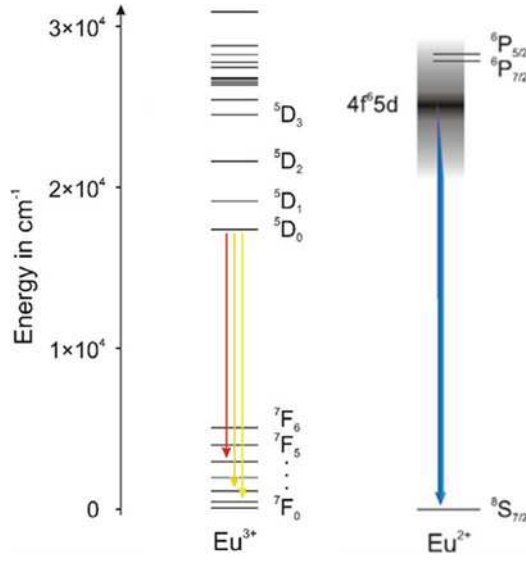
Figure 3.1: *Electronic energy levels of Eu^{2+} (right) and Eu^{3+} (left). Eu^{2+} shows a broad d–f emission in the blue since the energy levels of the $4f^7$ configuration have a higher energy than the broad levels of the $4f^6 5d$ configuration. Eu^{3+} ($4f^6$ configuration) shows typical f-f emission lines in the yellow to red [92].*

and $4f^6 5d$ configuration is smaller than in the case of Eu^{3+}, and transitions between them may be observed in the UV-visible spectroscopic range. Figure 3.3 reports a typical Eu^{2+} emission spectrum which is notably different from that of the trivalent ions: in fact it consists of a broad band, due to the $4f \longrightarrow 5d$ electronic transitions, peaked in the wavelength range of 550-650 nm.

Since 5d levels exhibit a less localized nature and a stronger coupling to lattice vibrations, and being the Eu inter-configuration $4f^7 \longrightarrow 4f^6 5d$ transitions parity-allowed, the emission intensities are up to 10^4 times stronger than those associated to intra-4f transitions.
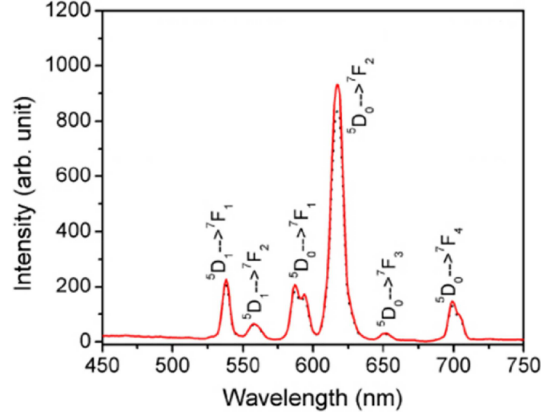
Figure 3.2: *Emission spectrum of Eu^{3+} in YVO_4 [93].*
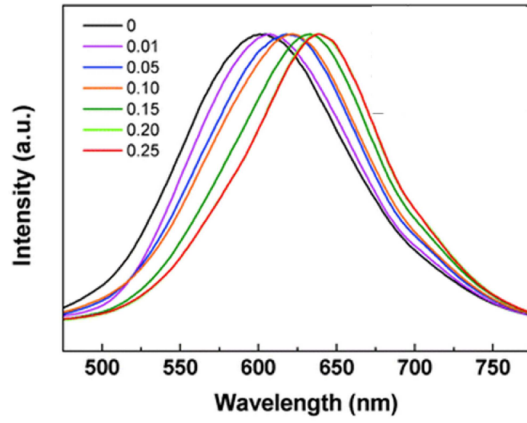
Figure 3.3: *Emission spectra of $Ca_{2.95}SiO_{4-x}S_xCl_2$:$0.05Eu^{2+}$ for x values ranging from 0 to 0.25 [94].*

Moreover, the Eu^{2+} emission characteristics strongly depends on the host matrix: in figure 3.3 a change in the stoichiometry of the host corresponds to a shift of about 50 nm of the maximum of the PL emission. This emission wavelength shift is evidenced in figure 3.4, where the $4f^6 5d$ levels of Eu^{2+} are split due to the influence of the crystal field of the host matrix. By increasing the crystal field acting on Eu^{2+} ions, the emission wavelength can be tuned from 400 (UV-blue) to 600 (yellow-red) nm and the intensity and lifetime are strongly influenced too.
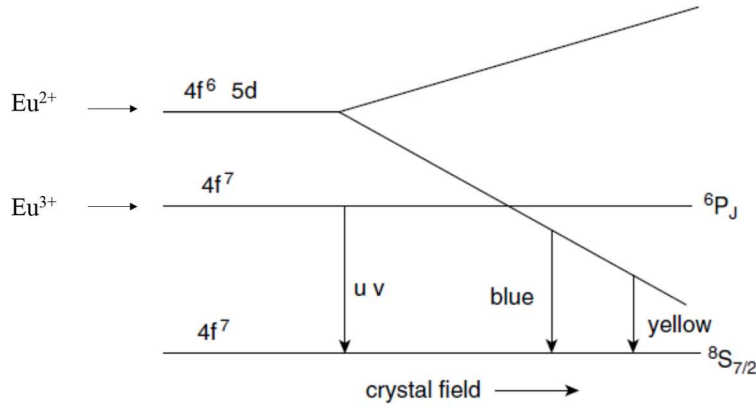
Figure 3.4: *Schematic energy level diagram of Eu^{2+} and Eu^{3+} ions as function of the magnitude of the crystal field [49].*

For practical applications in Si photonics, including the fabrication of light sources or optical amplifiers, or in solid-state lighting, an Eu-based device has to cope both with the presence of two oxidation states and with the dependence of emission properties on the host material. These properties differentiate Eu from other RE ions widely used in photonics, such as Er, which is stable only in the trivalent oxidation state. The simplest road that has been followed to couple Eu ions with the Si technology is represented by Eu doping of a SiO_2 matrix

[48, 53, 95–97]. In particular, *Skorupa* and co-workers [48, 53, 95, 96] extensively studied the properties of electroluminescent metal-oxide-semiconductor (MOS) devices based on Eu-doped SiO_2 layers exploiting the emission from both Eu^{2+} and Eu^{3+} ions. In figure 3.5 the electroluminescence (EL) spectra of Eu doped SiO_2 having different Eu concentrations are reported. The spectra show a great variability in the blue-green spectral region due to Eu^{2+}, while the Eu^{3+} peaks in the red region show no shift of their position by varying the Eu concentration. The 5d orbital sensitivity to the chemical environment qualitatively explains the variability in the blue-green region, since the SiO_2 microstructure remarkably changes with Eu concentration.
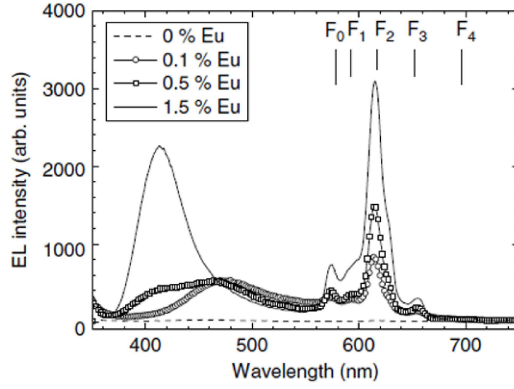
Figure 3.5: *EL spectra of Eu-implanted MOS devices for various Eu concentrations. The solid lines indicate the position of the $^5D_0 \longrightarrow {^7F_J}$ lines $(0 \leqslant J \leqslant 4)$ [49].*

The dependence of the emission spectra of Eu-doped SiO_2 on the synthesis conditions is not the only issue to be faced, since another key point to be considered is the low Eu solid solubility and the consequent cluster formation. The latter phenomenon occurs when impurity atoms are incorporated at concentrations higher than the solid solubility and are subjected to an annealing process. For these reasons,

the solid solubility represents an important limit for practical applications of REs in solids, and the search for innovative host matrices able to accommodate higher RE concentrations is currently attracting the efforts of a wide scientific community [98, 99]. In particular, it was observed that an efficient emission of Eu-doped SiO_2 is strongly prevented by the low Eu solid solubility in this host material, which leads to massive phenomena of Eu clustering and precipitation [53, 95–97].

The main challenge for Eu applications in photonics or solid-state lighting is therefore represented by the availability of a host matrix, whose synthesis and processing are compatible with the involved technologies, which is simultaneously able to efficiently host high concentrations of optically active Eu ions and that allows the control of the Eu oxidation state.

In this chapter we will investigate the structural and optical properties of Eu-doped SiOC films and we will compare them with those of Eu-doped SiO_2 films. The final aim is to overcome the limits of SiO_2 as a host matrix for Eu ions, by obtaining a material in which high concentrations of optically active Eu^{2+} ions can be accommodated. Furthermore, a new approach, consisting in the stacking of Eu-doped SiOC films doped with different Eu concentrations, will be proposed; this multilayer approach exploits the tunability of Eu^{2+} emission peak position as a function of the Eu concentration, and it will be shown that it is able to provide an efficient and Si-compatible white light source operating at room temperature, which could be of great interest for both photonic and lighting applications.

3.2   Synthesis of SiO_2:Eu and SiOC:Eu thin films

To study the influence of the host matrix on the optical, chemical and structural properties of Eu ions, two different Eu-doped Si-based thin films, SiO_2:Eu and SiOC:Eu, have been grown.

Eu-doped SiO_2 thin films were deposited on (100) Si substrates heated at 400 °C by using an ultrahigh vacuum magnetron sputtering system. The base pressure was about $1 \cdot 10^{-9}$ mbar. The deposition has been obtained by rf co-sputtering of 4 inches diameter, water-cooled SiO_2 and Eu_2O_3 targets (figure 3.6a). The deposition was carried out with a sputter up configuration in a $5 \cdot 10^{-3}$ mbar Ar atmosphere. Sputter rates have been set in order to obtain two Eu concentrations (1.5 and $5.0 \cdot 10^{20}$ Eu/cm^3). Similarly, Eu-doped SiOC thin films were grown by rf co-sputtering of SiO_2, SiC and Eu_2O_3 targets (figure 3.6b); sputter rates have been set in order to obtain a C concentration of about 5 at.% and Eu concentration of $1.5 \cdot 10^{20}$ Eu/cm^3. Both kinds of films are about 200 nm thick. After deposition, samples were thermally treated for 1 h in ultra-pure O_2 or N_2 ambient by using a horizontal furnace operating at temperatures ranging from 750 to 1000 °C.

Transmission electron microscopy (TEM) analyses in bright field (BF) mode were performed with a 200 kV Jeol 2010 microscope to investigate the film structure, while a 200 kV Jeol 2010F microscope, equipped with a Gatan Image Filter, was used to investigate the chemical composition by energy filtered TEM (EFTEM) analyses.

The atomic composition of the films was studied by Rutherford backscattering spectrometry (RBS), using a 2 MeV He$^+$ beam in random configuration. The backscattered He ions from the near surface region of the sample are collected by a solid state detector placed at 165 ° with respect to the incident beam. In the RBS measurements, the relative number of He ions backscattered from a target atom into
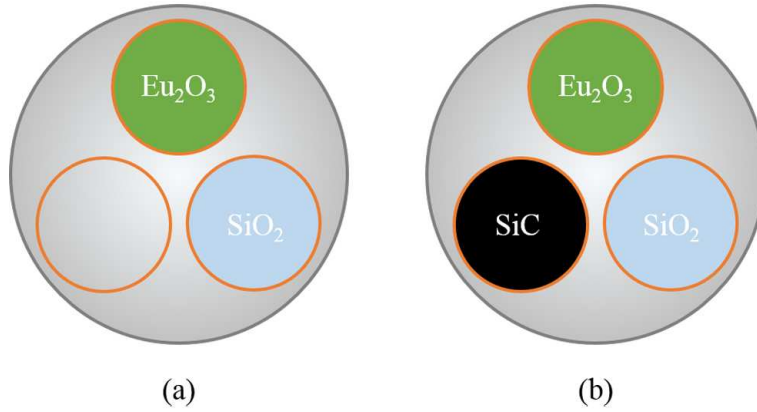
Figure 3.6: *Schematic representation of sputter target configuration used to deposit (a) SiO$_2$:Eu and (b) SiOC:Eu.*

a given solid angle, for a given number of incident particles, is related to the differential scattering cross section, which is basically proportional to the square of the atomic number of the target atom. From this relation, quantitative and chemical information can be collected. A schematic RBS spectrum of a sample composed by two elements A (lighter) and B (heavier), is displayed in figure 3.7. By measuring the height (H) of the A and B peaks and normalizing by the scattering cross sections for the respective elements, the concentration ratio of A to B can be obtained at any given depth in the film. It is also possible to calculate the A concentration in the film by comparing the height of the A peak to that of the peak for the pure A substrate, corrected for the different stopping cross sections of the two materials. Furthermore, by measuring the energy width ΔE of the peaks and dividing by the energy loss of He per unit depth in the sample, the thickness of the layer can be calculated.

PL measurements were performed at room temperature by using the same configuration shown in figure 2.5, by pumping with the 325
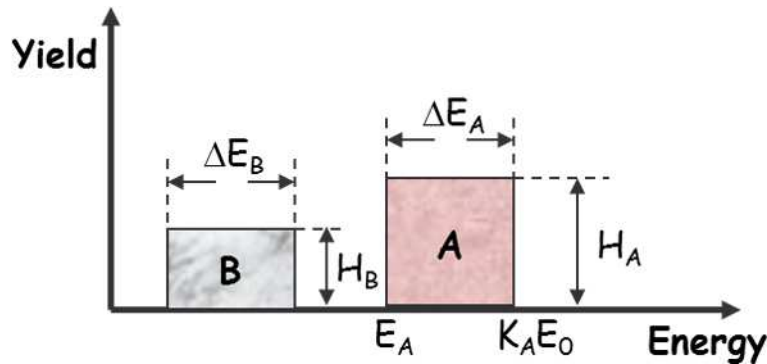
Figure 3.7: *Schematic representation of a RBS spectrum of a sample composed by two elements A and B. In this sketch the spectrum is composed by two peaks for which ΔE correspond to the energy width and H is referred to the height.*

nm line of a He-Cd laser. The pump power was about 2 mW and the laser beam was chopped through an acousto-optic modulator at a frequency of 55 Hz. The PL signal was analyzed by a single grating monochromator and detected with a Hamamatsu visible photomultiplier. Spectra were recorded with a lock-in amplifier using the acousto-optic modulator frequency as a reference. All the spectra have been measured at room temperature and corrected for the system spectral response. PL lifetime measurements were performed by monitoring the decay of the luminescence signal at a fixed wavelength after pumping to steady state and switching off the laser beam. The overall time resolution of our system is of 200 ns.

Photoluminescence excitation (PLE) measurements in the 250-475 nm range were performed by using a FluoroMax spectrofluorometer by Horiba. All the spectra have been measured at room temperature and corrected for the system spectral response.

3.3 Structural and Optical properties of Eu-doped SiO$_2$ films

As already illustrated in section 3.1, Eu ions have a low solid solubility in a SiO$_2$ matrix, particularly after the thermal process required to maximize the emission properties of the system. Thermal annealing is unavoidable when Eu ions are introduced by ion implantation[53], since this process removes implantation damage (which may create non-radiative de-excitation channels) and makes Eu ions optically active, by optimizing their chemical environment [95]. However, a thermal annealing can be very useful also when, as in the present case, a non-damaging technique, such as co-sputtering, is used to dope the material.

We have used TEM analyses to study cluster formation in Eu-doped SiO$_2$ and its dependence on the thermal annealing conditions. In figure 3.8 a the BF cross sectional TEM (XTEM) of a SiO$_2$ film doped with 5.0 1$\cdot$ 10^{20} Eu/cm^3 and annealed at 750 °C in N$_2$ is reported and shows that no precipitation occurs. The same scenario is found in as-deposited materials and for samples annealed at temperatures lower than 750 °C.

On the other hand, by increasing the temperature up to 900 and 1000 °C in N$_2$, precipitate formation occurs, as clearly visible in the BF XTEM images shown in figures 3.8b and c, respectively. At 900 °C clusters are almost homogeneously distributed throughout the film, but their size markedly decreases on going from the interface with the substrate (where diameters as large as about 15 nm are found) towards the surface (where the mean diameter is a few nm). After a further increase of the annealing temperature up to 1000 °C most of the precipitates are found close to the surface and a marked increase of their maximum diameter (about 30 nm) occurs.

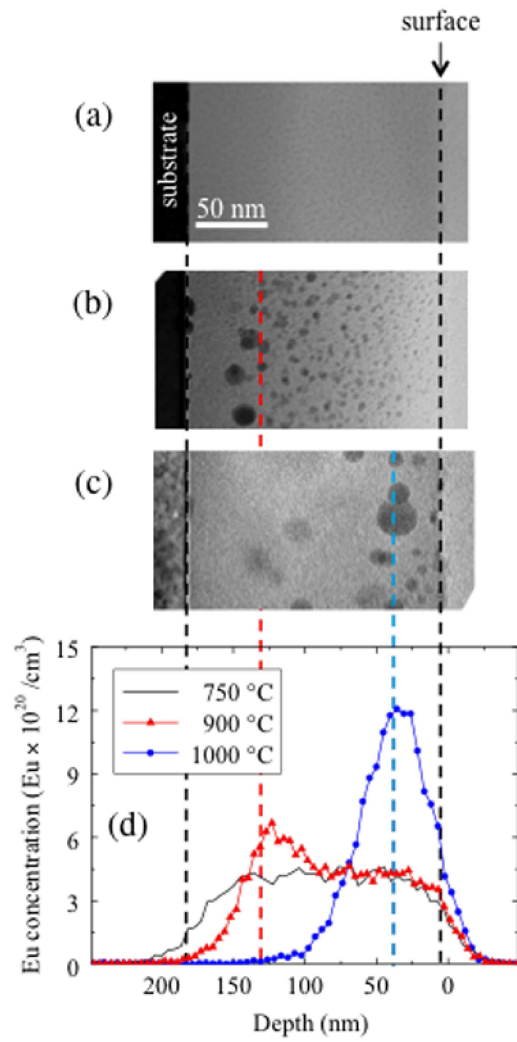Eu precipitation is tightly related to Eu diffusion toward the sur-

Figure 3.8: *BF XTEM images of Eu-doped SiO_2 films annealed in N_2 ambient at (a) 750 °C, (b) 900 °C, and (c) 1000 °C. Eu concentration is $5.0 \cdot 10^{20}$ cm^{-3} in all cases. (d) Eu concentration profiles, measured by RBS, relative to the samples shown in panels (a)-(c).*

face, as demonstrated by the analysis of the Eu concentration profiles, measured by RBS, reported in figure 3.8d. The Eu profile of the sample annealed at 750 °C (black line) is almost constant throughout the SiO$_2$ layer, indicating the absence of relevant diffusion phenomena at this temperature. At 900 °C (red line and triangles) an Eu peak located at a depth of about 125 nm (corresponding to the region where the larger precipitates are detected in the TEM image) emerges over the Eu background concentration. At 1000 °C (blue line and circles) the Eu peak is more intense and moves towards the surface, at a depth of about 30 nm, corresponding again to the region where the larger precipitates are detected by TEM, while in the deeper regions the residual Eu concentration is very low. In all cases the integrated Eu concentration does not change with respect to the as-deposited sample, indicating the absence of Eu outdiffusion phenomena.

In order to gain more information on the nature and composition of the precipitates, further TEM investigations have been performed. Figure 3.9a shows a BF XTEM image, taken at a higher magnification with respect to the image of figure 3.8b, of an Eu-doped SiO$_2$ sample containing $5.0 \cdot 10^{20}$ Eu/cm^3 and treated at 900 °C in N$_2$ atmosphere. Since no information on the cluster composition can be extracted from a conventional TEM image, EFTEM technique has been employed. EFTEM is an electron microscopy technique which allows us to generate a TEM image by using only electrons that have lost a specific amount of energy due to the interaction with the sample. This allows us to obtain a chemical mapping of all the species present in a sample with the very high spatial resolution typical of TEM [100]. In figure 3.9b the EFTEM map of elemental Eu, obtained by energy filtering at 133 eV (corresponding to the NIV edge of Eu) and by using the 3-windows method [101], is shown; the image displays exactly the same region shown in figure 3.9a and unambiguously demonstrates that all clusters contain Eu.

The diffraction pattern reported in the inset of figure 3.9a indi-
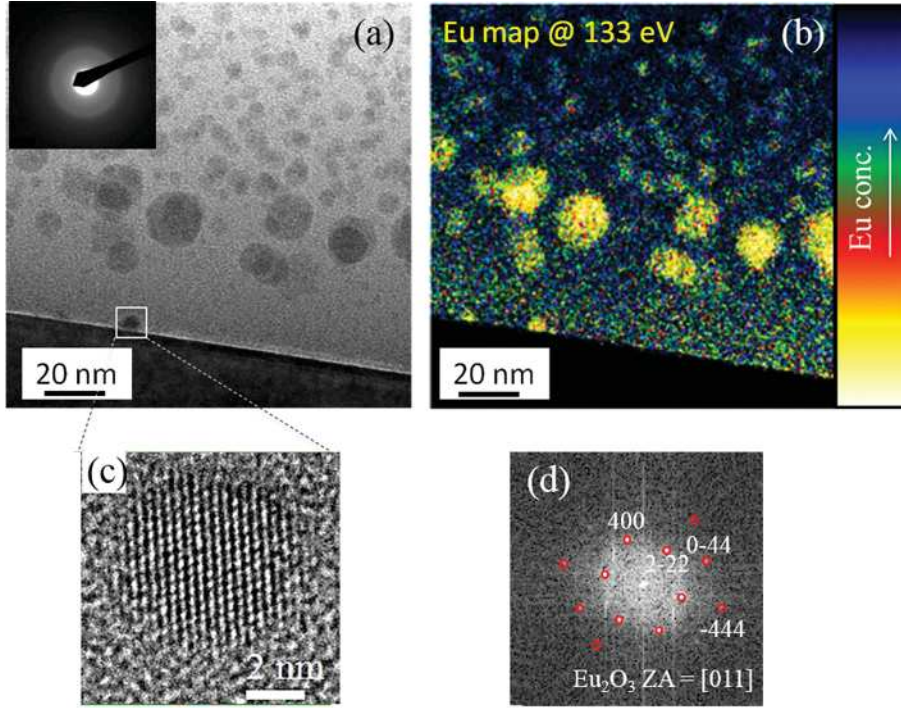
Figure 3.9: *(a) BF XTEM image relative to an Eu-doped SiO_2 film (Eu concentration is $5.0 \cdot 10^{20}$ cm^{-3}) annealed in N_2 ambient at 900 Â°C. In the inset the electron diffraction pattern of the same sample is shown. (b) EFTEM cross section image showing the same region of the same sample shown in panel (a), obtained by energy filtering at 133 eV (corresponding to the N_{IV} edge of Eu). (c) HR TEM image of the precipitate circled in red in panel (b). (d) Fast Fourier transform of the cluster shown in panel (c); the red circles are the simulation of the FFT.*

cates that the Eu-containing precipitates are amorphous or strongly damaged. Since high resolution (HR) TEM analyses conducted on tens of clusters was not able to detect the typical fringes of the crystalline planes, we can conclude that they are amorphous. The only crystalline clusters are detected at the interface with the Si substrate, as shown by the HR TEM image reported in figure 3.9c, referring to the cluster marked with a white square in figure 3.9a. The analysis of the corresponding fast Fourier transform (FFT), shown in figure 3.9d, reveals that these precipitates are epitaxial with respect to the Si substrate. Moreover, the simulation of the FFT, performed by using Carine Cristallography software [102] and superimposed in figure 3.9d as red circles, allows to recognize that these clusters have the crystalline structure of pure Eu$_2$O$_3$. The experimental evidences on the nature of the interfacial clusters, coupled with the well known tendency of RE ions, including Eu and Er, to precipitate as an oxidized phase when they are embedded in SiO$_2$ [103, 104], allow us to reasonably conclude that also the amorphous precipitates consist of Eu oxides (and/or silicates).

Eu precipitation in SiO$_2$ is not a surprising phenomenon, since it is well known that it has a low solid solubility [53, 97, 103] and diffuses very fastly in this matrix. On the other hand, the peculiar temperature dependence of the precipitation phenomenon (both size and position of the clusters remarkably change) and the tendency of the clusters to move towards the surface when the annealing temperature is increased are certainly less expected. In the as-deposited sample the Eu ions are homogeneously distributed throughout the film; during the thermal process they acquire mobility but, in absence of any concentration gradient, no relevant diffusion process towards a preferential direction is expected. It should be taken into account that Eu ions tend to be fully coordinated with O atoms and that a non-negligible O$_2$ contamination is unavoidably present in the conventional furnaces used for thermal processing in Si-based technology, even if ultra-pure

N_2 is used. This implies that, during the thermal process, O diffuses inside the samples but, given its low concentration, it is reasonable to assume that it is mainly present in the surface region of the film. Therefore, the higher O concentration close to the surface and the tendency of Eu ions to be surrounded by O atoms to stabilize their chemical environment, both concur to force Eu migration towards the surface, as shown in figure 3.8. Under these conditions Eu solubility in SiO_2, especially close to the surface, is largely overcome and clustering occurs.

To confirm the role of O as a driving force for Eu migration towards the surface, annealing processes in pure O_2 ambient have been performed. In particular, an Eu-doped SiO_2 sample containing $5.0 \cdot 10^{20}$ Eu/cm^3 has been annealed at 900 °C in O_2 ambient. In these conditions we expect that, due to the temperature, O can homogenously diffuse throughout the sample and therefore the effect related to the disomogeneous O distribution observed for N_2 annealing processes would be reduced. The main results of the thermal processes performed in O_2 ambient is shown in the BF XTEM image of an Eu-doped SiO_2 sample containing $5.0 \cdot 10^{20}$ Eu/cm^3, reported in figure 3.10a. Indeed, if compared with the image of figure 3.8b, it is clear that clustering, although still present, is deeply influenced by the change of annealing ambient. Superimposing the Eu concentration profile obtained from RBS measurements to the XTEM image, as shown in figure 3.10a, a homogeneous Eu depth distribution and the absence of any Eu diffusion towards the surface can be observed.

The precipitation phenomenon can be better described by using cross section EFTEM images; the Eu map shown in figure 3.10b, obtained by energy filtering at 133 eV, evidences a huge number of very small Eu-containing precipitates (the mean diameter is of about 5 nm) uniformly dispersed throughout the film. The image confirms that O diffuses inside the whole film. Indeed under these conditions Eu ions have no reasons to move, and the precipitation phenomenon shown
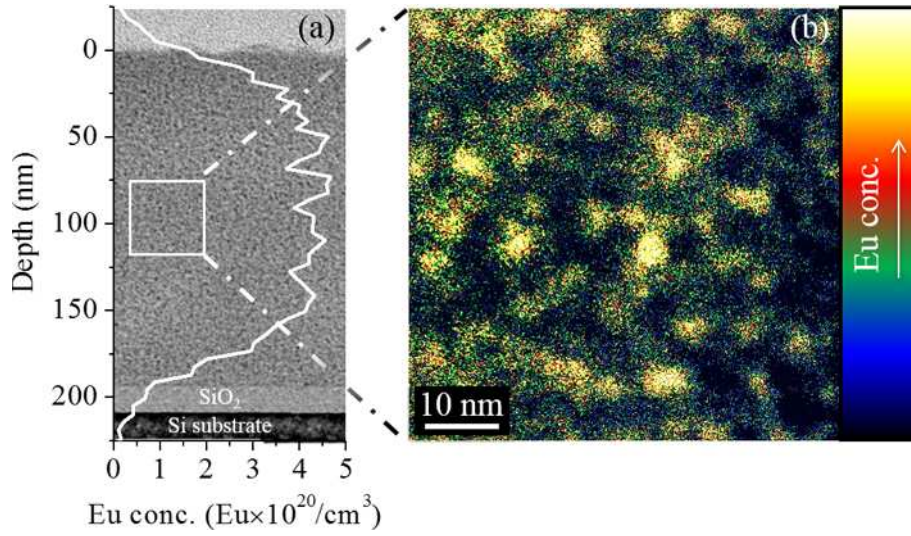
Figure 3.10: *(a) BF XTEM image relative to an Eu-doped SiO$_2$ film (Eu concentration is 5.0·10^{20} cm^{-3}) annealed in O$_2$ ambient at 900 °C. The Eu concentration profile, measured by RBS, is superimposed to the image. (b) EFTEM Eu map showing a detail of the sample, obtained by energy filtering at 133 eV (corresponding to the NIV edge of Eu).*

in figure 3.10 depends only on the overcoming of the Eu solubility in SiO$_2$. Since this scenario is strongly different with respect to that characterizing samples annealed in N$_2$ ambient, we can conclude that O plays a key role during the annealing of Eu-doped SiO$_2$ and we can also evaluate the solubility limit of Eu in SiO$_2$, that is smaller than 5.0·10^{20} cm^{-3}

In order to correlate the structural and the optical properties of Eu-doped SiO$_2$ films, we have performed PL measurements. Figure 3.11 shows the room temperature PL spectra of as-deposited and annealed films, obtained by exciting the samples with the 325 nm line of a He-Cd laser.
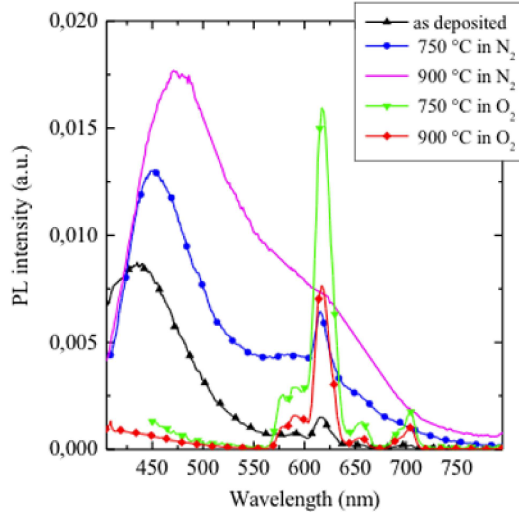
Figure 3.11: *Room temperature PL spectra of Eu-doped SiO_2 films (Eu concentration is $5.0 \cdot 10^{20}$ cm^{-3}) as-deposited and annealed at 750 and 900 Â°C, both in N_2 and O_2 ambient.*

The PL spectrum of the as-deposited sample consists of a broad band having its maximum at ∼435 nm, corresponding to the emission of Eu^{2+} ions [105], and of some narrow lines at ∼600 nm corresponding to the emission of Eu^{3+} ions [106]. The most intense Eu^{3+} line is found at 616 nm with a FWHM of about 15 nm and it corresponds to the $^5D_0 \longrightarrow {}^7F_2$ transition of Eu^{3+} ions in solid matrices; the less intense peaks at about 578, 590, 656 and 704 nm correspond to $^5D_0 \longrightarrow {}^7F_J$ transitions, with J = 1, 3, 4 and 5, respectively. After annealing the samples in N_2 ambient, we notice an increased intensity of the peak associated to Eu^{2+}, coupled with a shift to 450 nm (at 750 °C) and to 475 nm (at 900 °C); a further increase of the PL intensity and a small redshift are found at 1000 °C (spectrum not shown). The Eu^{3+} emission remains clearly visible as a peak at 750 °C and as a

shoulder of the Eu^{2+} peak at 900 °C. The increased PL intensity in annealed samples accounts for a reduced defects density in the host matrix which can represent preferential non-radiative decay channels and for a better Eu coordination, while the redshift of Eu^{2+} peak is related to the formation of regions characterized by different local Eu concentrations [107, 108]. Indeed, as discussed in section 3.1.1, while the emission of Eu^{3+} is due to intra-4f shell transitions and does not depend on the chemical environment of the ion, the emission of Eu^{2+} is due to a 4f-5d transition and it is sensible to local variations of the Eu chemical environment [109]. The co-existence of Eu^{2+} and Eu^{3+} ions in Eu-doped SiO$_2$ is not surprising [49]. It should be noted that the different nature of the Eu^{2+} and Eu^{3+} emissions (the first is due to an allowed transition, the second to a forbidden one) could lead to an overestimation of the Eu^{2+} content, if it is based only on the relative intensities of their PL signals. This means that even a small O deficiency can determine the presence of an Eu^{2+} signal having an intensity comparable to that of Eu^{3+}, even if the number of optically active divalent Eu ions is much lower than the trivalent ones.

On the other hand, from the analysis of figure 3.11 it appears evident that in samples annealed in O$_2$, the Eu^{2+} peak fully disappears, due to the complete oxidation of Eu^{2+} in Eu^{3+}. We notice also an increase by about a factor of 10 of the PL intensity for the Eu^{3+}-related peaks in the sample annealed at 750 °C in O$_2$ with respect to the as-deposited one. A decrease of the PL intensity by about a factor of 2 is found when the annealing temperature is increased up to 900 °C, contrarily to what happens for N$_2$ processes, where a monotonic increase as a function of the annealing temperature is observed. This effect depends on the higher effectiveness of O with respect to the temperature in eliminating matrix defects that may act as non-radiative de-excitation channels, by maximizing the yield of the photon emission process already at 750 °C. As a consequence, a further increase of the annealing temperature produces only a decrease of the

emission intensity due to the occurrence of clustering phenomena, in agreement with the TEM data shown in figure 3.11.

By summarizing, the structural data concerning Eu-doped SiO_2 highlight the occurrence of Eu precipitation in samples annealed both in O_2 and in N_2 environments. Although it is clear that this phenomenon strongly limits the fraction of optically active Eu ions, it is also evident that, due to the defects present in the matrix, a thermal process is required to optimize the optical properties of the system. This need is demonstrated by the stronger PL signals exhibited by annealed samples, even if the thermal process simultaneously induces Eu precipitation.

Since it is well known that Eu compounds can be very efficient light emitters [110], as it will be extensively discussed in chapter 4 of this thesis, a question arises about the possibility that the measured PL signals come (at least in part) from Eu-containing clusters formed during the annealing processes. However, previously reported strong light emission from RE compounds, such as oxides or silicates, has been linked to the presence of crystalline structures [111]. In the case of Eu-doped SiO_2 (figures 3.8-3.10) most of precipitates are amorphous (and very reasonably they have not a well defined stoichiometry), so that their optical inactivity appears probable.

Eu precipitation and the prevalence of the Eu^{3+} oxidation state both concur in making the optical properties of Eu-doped SiO_2 films quite far from the requirements for application of this material as a light source. A straightforward approach to solve at least the problem of Eu precipitation could be to reduce its concentration. The result of this attempt is illustrated in the BF XTEM images reported in figures 3.12a and 3.12c, referring to a SiO_2 film containing $5.0 \cdot 10^{20}$ Eu/cm^3 (i.e. an Eu concentration which is more than 3 times lower than that present in the samples discussed above), annealed in N_2 at 900 and 1000 °C, respectively. The TEM images show that Eu precipitation is still present; precipitate position is very similar to that found in

samples containing a higher Eu concentration, but a marked decrease of their size and density is obtained. Although these improved structural properties also produce a moderate increase of the PL intensity (accounting for less than a factor of 2 at 900 °C), it seems clear that further improvements are needed.

3.4 Structural and optical properties of Eu-doped SiOC films

It has been widely reported in literature that the Eu solubility can be remarkably increased by properly modifying (from both chemical and structural points of view) the host matrix [103, 112, 113]. Since the high luminescence efficiency of Eu^{2+} ions can be more appealing for lighting or photonics purposes, the matrix has been modified in order to simultaneously increase the Eu solubility and efficiently induce the $Eu^{3+} \longrightarrow Eu^{2+}$ reduction. In particular, instead of using SiO_2, we incorporated Eu ions in a SiOC matrix having a C content of about 5 at.%. SiOC has been already used as a host matrix for RE ions, including Er [114], Eu [88] and Tb [74]. Furthermore SiOC contains C, which is a reducing agent and can be used to promote the $Eu^{3+} \longrightarrow Eu^{2+}$ reduction [105]. In addition, since SiC is a wide bandgap semiconductor, a possible effect of indirect Eu excitation through energy transfer from SiC nanoclusters (nc) or the SiOC matrix, could be sought for, similarly to what happens in Er-doped Si nc [36]. Finally, as already found in the case of Si-rich SiO_2 [37], an improved electrical conduction in SiOC with respect to SiO_2 could be expected. This last property could make the material also suitable for the fabrication of electroluminescent devices.

In figures 3.12b and 3.12d the BF XTEM images relative to Eu-doped SiOC films annealed in N_2 ambient at 900 and 1000 °C, respec-
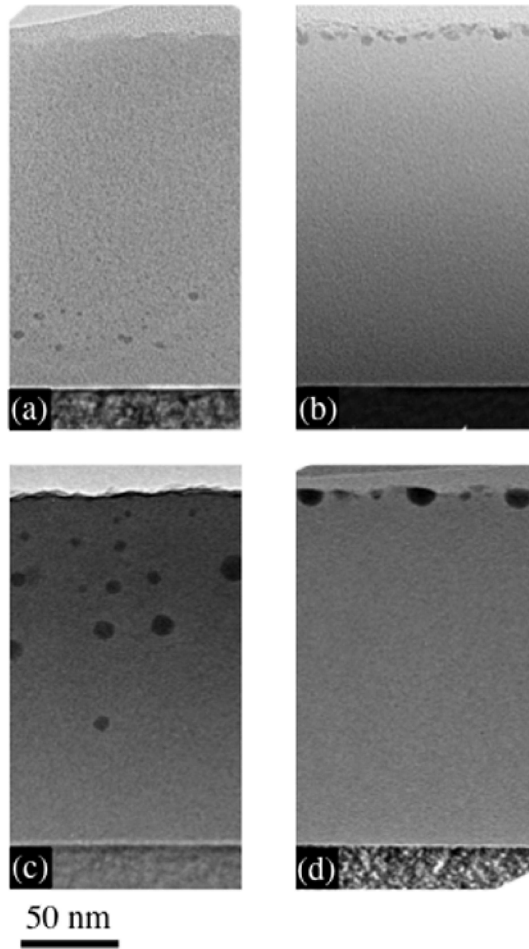
50 nm

Figure 3.12: *BF XTEM images relative to: (a) Eu-doped SiO$_2$ annealed in N$_2$ ambient at 900 °C; (b) Eu-doped SiOC annealed in N$_2$ ambient at 900 °C; (c) Eu-doped SiO$_2$ annealed in N$_2$ ambient at 1000 °C; (d) Eu-doped SiOC annealed in N$_2$ ambient at 1000 °C. Eu concentration is 1.5·10^{20} cm^{-3} in all of the samples.*

tively, are reported and compared to those relative to Eu-doped SiO_2 (figures 3.12a and 3.12c), annealed at the same temperature. The Eu concentration is $1.5 \cdot 10^{20}$ cm^{-3} for all the samples. From the comparison it is clear that SiOC matrix is very effective in increasing Eu solubility and that SiC addition dramatically changes the structural properties of the Eu-doped SiO_2 films. Indeed, for both the explored annealing temperatures, cluster formation occurs only at the sample surface. Precipitates have been studied by electron diffraction and EFTEM analyses and, analogously to what found for a pure SiO_2 matrix, they contain Eu and are amorphous. No precipitation occurs in as-deposited samples.

The quantitative analysis of the fraction of clustered Eu in the SiOC matrix has been done by performing RBS measurements. Figure3.13 shows the comparison between the Eu concentration profiles relative to an as-deposited Eu-doped SiOC film (black line) and those corresponding to thermally annealed samples (900 °C, red line and triangles; 1000 °C, blue line and circles, both in N_2 environment).

Data in figure 3.13 show an uniform Eu depth distribution in the as-deposited film, while for annealed samples the occurrence of Eu surface segregation is evidenced, in agreement with the TEM images reported in figure 3.12. The surface Eu concentration peaks account for about 10% (at 900 °C) and 65% (at 1000 °C) of the total Eu concentration (values estimated by subtracting a background equal to the Eu concentration in the deeper film regions). Even in this case, no Eu out-diffusion has been evidenced. Since Eu precipitates are confined in a very thin surface region, they can be also visualized by using plan view TEM analysis without the occurrence of any overlap between clusters. In figure 3.14 a plan view BF TEM image of an Eu-doped SiOC film annealed at 1000 °C (the corresponding XTEM image is shown in figure 3.12d) is reported.

The image shows a high density of well resolved, almost circular precipitates. The total volume of the precipitates can be easily eval-
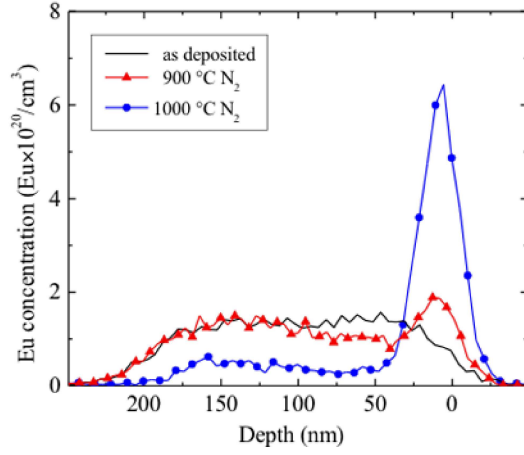
Figure 3.13: *Eu concentration profiles, measured by RBS, relative to Eu-doped SiOC films as-deposited and annealed in N_2 ambient at 900 and 1000 °C. Eu concentration is $1.5 \cdot 10^{20}$ cm^{-3} in all of the samples.*

uated by supposing a spherical shape for the clusters. However, since the precipitate composition is unknown, the fraction of clustered Eu ions cannot be unambiguously derived. Alternatively, by using the tabulated densities for the most common Eu compounds containing O and/or Si, we can estimate that an Eu fraction ranging from 40% (by hypothesizing the presence of the Eu compound characterized by the lowest Eu density, i.e. the silicate $EuSiO_3$ [115]) to 85% (if the Eu compound characterized by the highest Eu density, i.e. the oxide EuO [116], is present) is contained in the precipitates. Both values are in good agreement with the RBS estimate obtained from the data in figure 3.13. Although a fraction of precipitated Eu roughly ranging from 40 to 85% (at 1000 °C) could appear very high, we underline that the dissolved fraction corresponds, in the worst condition, to an Eu concentration of about $2.2 \cdot 10^{19}$ cm^{-3}, which remains a very high solubility value with respect to those reported in literature for RE ions
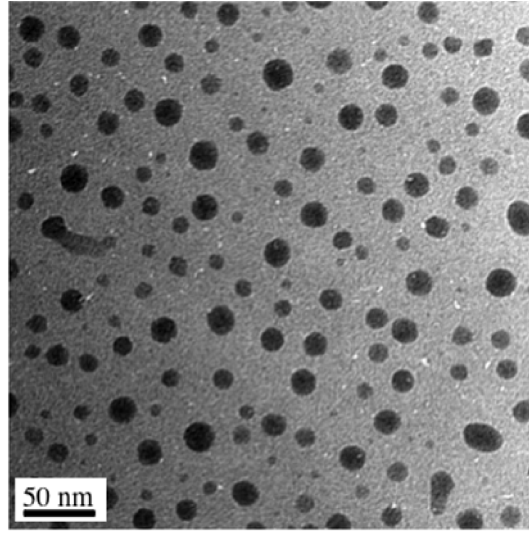
Figure 3.14: *Plan view BF TEM image of an Eu-doped SiOC film annealed in N_2 ambient at 1000 °C. Eu concentration is $1.5 \cdot 10^{20}$ cm^{-3}.*

dissolved in the most common SiO_2-based matrices [117].

The peculiar behaviour of Eu in SiOC is due to the combined effect of O (which, analogously to the case of the pure SiO_2 matrix, activates Eu diffusion towards the surface) and of an enhanced Eu mobility in the SiOC matrix. This enhanced Eu diffusion must be necessarily taken into account, since the precipitates detected at the surface have a total Eu content which largely exceeds that present in the surface region in absence of any diffusion process. Under these conditions, a very high Eu concentration is gathered in the surface layers, leading to the extensive cluster formation shown in the TEM images of figures 3.12 and 3.14.

On the basis of the above results, it is important to limit the O influence during the thermal annealing of the sample in order to reduce Eu diffusion towards the surface and the consequential Eu precipita-

tion and to fully exploit the enhanced Eu solubility in this matrix. The strategy we followed is the deposition of a SiO_2 capping layer (about 200 nm thick) on Eu-doped films before performing the annealing step, in order to avoid as much as possible additional interactions between Eu ions and the O_2 present in the furnace ambient.

The effect of the capping layer on the Eu behaviour is shown in figure 3.15 where the BF XTEM images relative to SiO_2-capped Eu-doped SiOC (a) and SiO_2-capped Eu-doped SiO_2 (b) samples annealed at 900 °C in N_2 are reported. Eu concentration is $1.5 \cdot 10^{20}$ cm^{-3} in both cases. Figure 3.15a demonstrate that the capping layer is able to completely suppress Eu precipitation in the SiOC matrix, especially if compared with the same sample without the capping layer (see figure 3.12b), where clusters are found at the sample surface. In the same figure the Eu concentration profile obtained by RBS measurements, showing that Eu is uniformly dispersed inside the film, is overlapped to the TEM image. For comparison a SiO_2 capping layer has been also deposited on Eu-doped SiO_2, samples. In this last case it is clear that the SiO_2 capping layer is less effective in avoiding Eu precipitation; indeed, the XTEM image reported in figure 3.15b shows the presence of residual Eu-containing precipitates close to the interface with the Si substrate. This experiment demonstrates that in a situation in which Eu is not subjected to any diffusion process, the SiOC matrix is able to fully prevent Eu precipitation thus increasing its solubility with respect to pure SiO_2.

Data shown in figures 3.12-3.15 clearly illustrate the complex structural evolution induced by the addition of SiC to a SiO_2 matrix, and, above all, how the capability of the matrix to incorporate high Eu concentration is deeply (and positively) affected. Furthermore, due to the presence of C, the SiOC matrix is also able to efficiently promote the $Eu^{3+} \longrightarrow Eu^{2+}$ reduction. Indeed when Eu ions can react with reducing agents, such as C in our case, Eu^{2+} oxidation state can be stabilized.
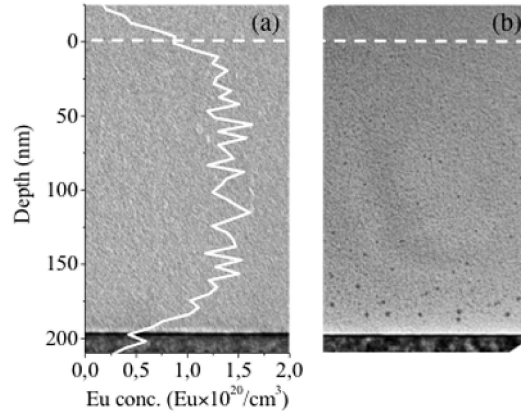
Figure 3.15: *(a) BF XTEM image of Eu-doped SiOC annealed in N_2 ambient at 900 °C after the deposition of a SiO_2 capping layer. The Eu concentration profile, extracted from the RBS spectrum, is superimposed to the TEM image. (b) BF XTEM image of an Eu-doped SiO_2 annealed in N_2 ambient at 900 °C after the deposition of a SiO_2 capping layer. The dashed line indicated the position of the interface between the Eu-doped films and the SiO_2 capping layer. Eu concentration is $1.5 \cdot 10^{20}$ cm^{-3} in both samples.*

In figure 3.16 the PL spectra of as-deposited and annealed Eu-doped SiOC samples containing $1.5 \cdot 10^{20}$ Eu/cm^3 are reported. All the spectra are characterized by a similar shape, corresponding to Eu^{2+} emission, and no relevant wavelength shifts among the various peaks can be noted. Moreover no peaks or shoulders assignable to Eu^{3+} can be detected. The increase of the PL intensity by increasing the annealing temperature up to 900 °C can be ascribed to a change of the matrix structure due to the thermal treatment, which contributes also to reduce the defect density in the host matrix. The sample appears very bright under naked eye observation as in figure 3.16b is shown. The small shifts of the peak position are due to changes in the matrix structure due to a partial ordering of the film during

the thermal annealing. By increasing the annealing temperature of Eu-doped SiOC samples up to 1000 °C, no relevant variation of the PL emission is found; indeed, the PL spectrum (magenta line) appears almost unchanged both in shape and in position and the small decrease of the PL intensity (by about 20%) is in agreement with the presence of a higher precipitate density evidenced by the TEM and RBS data reported in figures 3.12 and 3.14.
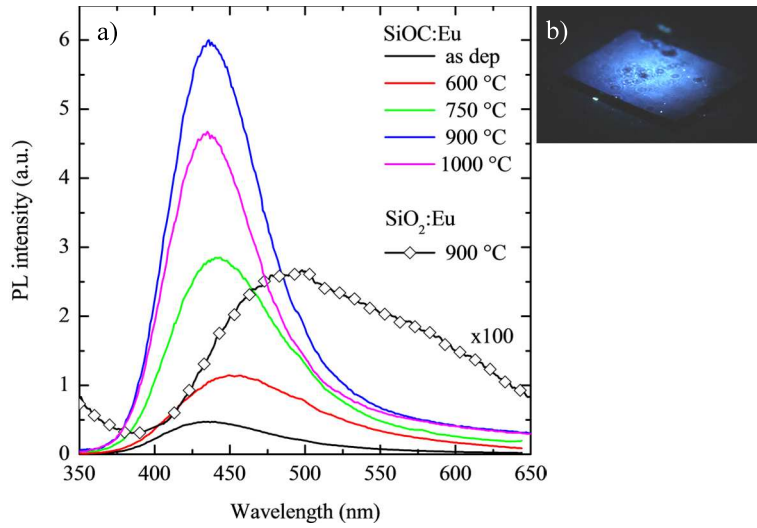
Figure 3.16: *(a)Room temperature PL spectra of Eu-doped SiOC as-deposited and annealed in the range 600-1000 °C in N_2 ambient and of Eu-doped SiO_2 annealed at 900 °C in N_2. The PL spectrum of Eu-doped SiO_2 is multiplied by a factor of 100 Eu concentration is $1.5 \cdot 10^{20}$ cm^{-3} in all of the samples. (b) Photograph of the sample annealed at 900 °C, having an area of about 1 cm?2, excited by 364 nm line of a fully defocused Ar^+ laser beam, showing a bright blue PL emission cleary visible by the naked eye.*

Figure 3.16 also allows the comparison between the PL spectrum

of an Eu-doped SiOC sample annealed at 900 °C in N_2 (blue line) with that of a SiO_2 sample with the same Eu content and annealed under the same conditions (multiplied by a factor of 100, black line and rhombus). By evaluating the integrated PL intensity of the two spectra, we obtain that a very strong enhancement of the room temperature PL emission by about a factor of 250 has been obtained when Eu is incorporated in SiOC instead of SiO_2; furthermore, the peak is sharper and its maximum, detected at around 435 nm, is blue-shifted by about 60 nm.

The enhancement of Eu solubility due to the presence of a SiO_2 cap layer on SiOC:Eu shown in figure 3.15 has beneficial effects also on the PL emission intensity. In figure 3.17 the PL spectra of Eu-doped SiOC samples annealed at 900 °C (red circles and line) and 1000 textdegree C (blue circles and line) after the SiO_2 cap deposition are shown. In agreement with the capability of the capping layer to fully prevent Eu precipitation, demonstrated by the XTEM image in figure 3.15a, an enhancement of the PL intensity by about a factor of 2 with respect to the same samples without the capping layer has been obtained for both temperatures.

Similarly to the case of the SiO_2 matrix, also for a SiOC matrix the observation of strong PL signals in samples characterized by the presence of Eu-containing precipitates rises the question on their possible optical activity. Although the arguments we have previously presented to exclude this effect maintain their validity also for the SiOC matrix, we have been able to collect a clear experimental evidence of the lack of relevant light emission from Eu-containing clusters. Indeed, the fact that, differently from the SiO_2 matrix, all the precipitates detected in SiOC are located in a thin (about 10 nm thick) surface region, allowed us to remove them by using a low energy, rastered Ar ion source. The observation that, also after cluster removal, the PL properties of the samples are unchanged constitutes a strong evidence of the fact that only the Eu ions which are dissolved in the matrix are optically active.
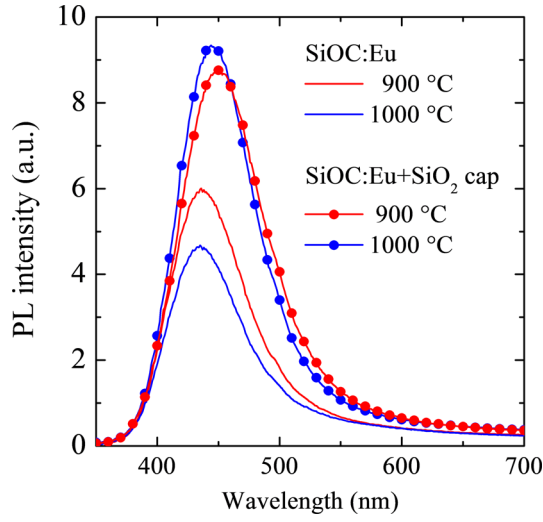
Figure 3.17: *Room temperature PL spectra of both SiO$_2$-capped and uncapped Eu-doped SiOC films annealed at 900 and 1000 °C in N$_2$ ambient. Eu concentration is $1.5 \cdot 10^{20}$ cm^{-3} in all of the samples.*

Moreover, this experiment supports the above reported considerations about the need of a well defined stoichiometry and/or crystalline structure to make the Eu-containing precipitates optically active.

Further information on the nature of Eu^{2+} emission can be obtained by time-resolved PL measurements. Figure 3.18a shows the time-decay curves of an Eu-doped SiOC sample with an Eu concentration of $1.5 \cdot 10^{20}$ cm^{-3} and treated at 900 °C in N$_2$, measured at different emission wavelengths lying within the broad PL peak shown in figure 3.16.

All of the curves are not single-exponential. The values of the decay-time τ, obtained by taking the time at which the PL signal is $1/e$ of the value at the laser shut-off, depend on the emission wavelength, since τ varies in the range 0.3-0.8 μs. Similarly to the inter-
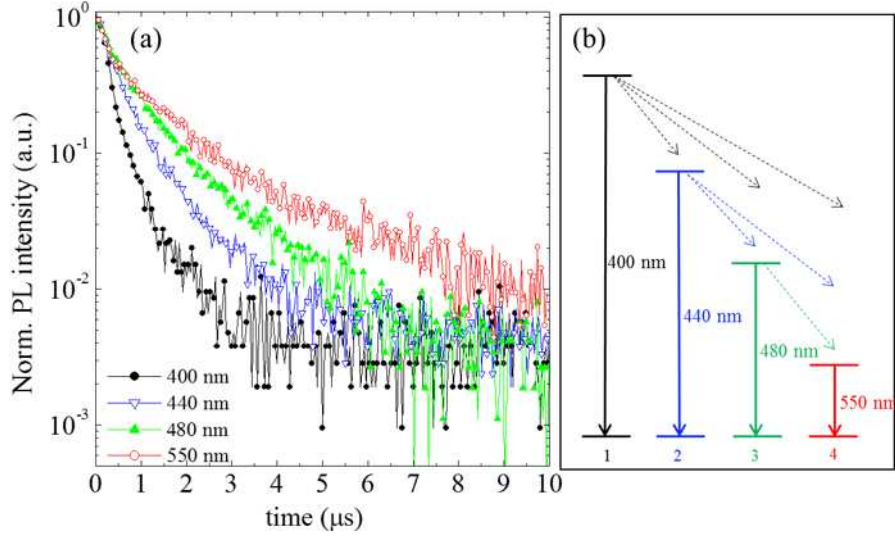
Figure 3.18: *(a) Room temperature time-decay PL curves of Eu-doped SiOC (Eu concentration is $1.5 \cdot 10^{20}$ cm^{-3}) treated in N_2 at 900 °C, measured at different emission wavelengths. (b) Schematic view of the model proposed to explain the data reported in panel (a); the numbers 1, 2, 3 and 4 correspond to different Eu^{2+} sites, in which the local Eu concentration increases on going from site 1 to site 4.*

pretation given to the same phenomenon observed in Si nc [118], the dependence of the τ values on the detection wavelength could be due to the mutual interactions among different Eu sites. More in detail, the PL decay behavior can be explained by the model sketched in figure 3.18b, where, for the sake of simplicity, we assume to have four different Eu^{2+} sites, while actually they could be many more. The numbers 1, 2, 3 and 4, correspond to different Eu^{2+} sites, in which the local Eu concentration increases on going from site 1 to site 4 and this fact, according to literature [108], produces a redshifted PL emission. Site 1 has the shortest decay lifetime and shows a radia-

tive emission (continuous arrow) at 400 nm and non-radiative decay channels (dashed arrows) that quench the PL emission through the interaction with sites 2, 3 and 4. Similar processes occur for sites 2 and 3, while site 4 has the longest decay lifetime because it can hardly find non-radiative channels to interact with other Eu sites. Time resolved PL measurements therefore demonstrate that the Eu^{2+} band peaked at about 440 nm shown in figure 3.16 can be actually considered the convolution of different contributions, corresponding to different Eu sites in the SiOC matrix.

These results demonstrate that SiOC can be a very suitable host matrix for luminescent Eu ions. Indeed, Eu precipitation, which strongly limits the optical efficiency of Eu ions embedded in the more conventional SiO_2 matrix, can be almost completely suppressed in SiOC. Furthermore, SiOC is also able to induce the $Eu^{3+} \longrightarrow Eu^{2+}$ reduction, providing a simple method to obtain high concentrations of the most optically efficient Eu species (Eu^{2+}). As in the case of Eu-doped SiO_2, the ambient of the annealing strongly influence the PL emission. To better understand the modification of the Eu emission properties, annealing in different ambient were performed. Figure 3.19 reports the room temperature PL spectra of Eu-doped SiOC samples having an Eu concentration of $1.5 \cdot 10^{20}$ cm^{-3}, treated at 900 °C in N_2 or O_2 ambient.

As already discussed, the N_2-treated sample (blue line) exhibits a very intense PL band, centered at about 440 nm, due to the $4f^65d \longrightarrow 4f^7$ transitions of Eu^{2+} ions, massively formed owing to a reduction reaction involving the C atoms of the SiOC matrix and no PL lines associated to Eu^{3+} are detected. The PL spectrum of the sample treated in O_2 ambient (magenta line, multiplied by a factor of 10 in the region 370-550 nm and by a factor of 400 in the region 550-750 nm) shows a band centered at about 420 nm, attributable to Eu^{2+} ions, and some weaker sharp peaks at longer wavelengths, typical of Eu^{3+} emission. The main Eu^{3+} peak is detected at 618 nm, which corre-
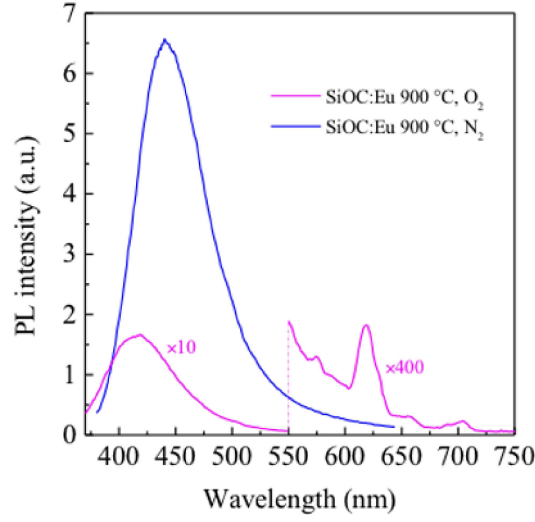
Figure 3.19: *Room temperature PL spectra for Eu-doped SiOC films annealed at 900 °C in N_2 (blue line), and in O_2 ambient (magenta line, multiplied by a factor of 10 in the region 370-550 nm and by a factor of 400 in the region 550-750 nm). Eu concentration is $1.5 \cdot 10^{20}$ cm^{-3}.*

sponds to the $^5D_0 \longrightarrow {}^7F_2$ transition, the other less intense peaks are at about 575, 657, 705 nm and correspond to $^5D_0 \longrightarrow {}^7F_J$ transitions of Eu^{3+} ions in solid matrices, with J = 0, 3 and 5, respectively. As expected, the annealing in oxidizing ambient promotes the formation of Eu^{3+} ions and it is therefore unsuitable to provide a strong Eu^{2+} emission. The shift of about 20 nm between the Eu^{2+} peaks detected in SiOC films annealed in O_2 and N_2 ambient is due to the well known dependence of the emission wavelength on the Eu concentration [108] for O_2 annealing treatments the concentration of Eu^{2+} ions decreases due to the oxidation process.

The results shown above highlight the dependence of the PL intensity in Eu-doped SiOC on the annealing conditions. A similar depen-

dence was already discussed in section 2.3 for the emission properties of SiOC. In figure 3.20 a comparison between the integrated PL intensities of undoped and Eu-doped SiOC is reported. For Eu-doped SiOC samples treated in N_2 (blue closed triangles) a monotonic increase of the integrated PL intensity as a function of the annealing temperature is found, while only a weak dependence is observed for processes in O_2 (blue closed circles). Interestingly, figure 3.20 demonstrates that these trends are very similar to those obtained by analyzing the integrated PL intensity of undoped SiOC samples after the same thermal processes (red open triangles refer to processes in N_2, red open circles to processes in O_2).
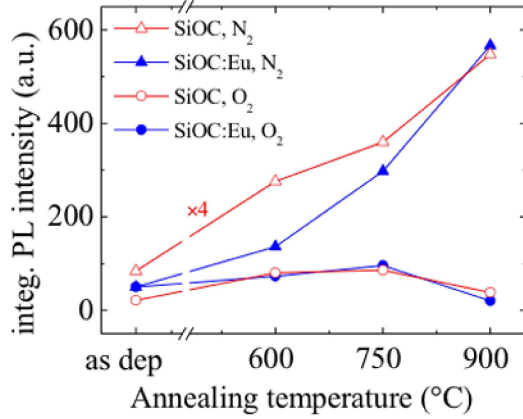
Figure 3.20: *Comparison of the integrated PL intensity as a function of the annealing temperature of undoped and Eu-doped SiOC (for both processes in N_2 and O_2); the data referring to undoped SiOC annealed in N_2 are multiplied by a factor of 4 to allow an easier comparison.*

The PL intensity values for undoped SiOC films treated in N_2 are remarkably weaker than those relative to Eu doped samples, so that they have been multiplied by a factor of 4 to make easier the comparison. The overlap between the trends of the PL intensities as a

function of temperature for undoped and Eu-doped SiOC annealed in N_2 is due to the fact that Eu^{2+} ions (which are by far the Eu species giving the main contribution to the PL signal of Eu-doped SiOC films) are formed owing to a redox reaction involving Eu^{3+} ions and Si-C bonds (which, as described in 2, give the main contribution to the PL signal of undoped SiOC films annealed in N_2). Indeed, by increasing the annealing temperature, the concentration of Si-C bonds increases and, as a consequence, the number of emitting Eu^{2+} ions, formed through the redox reaction, becomes higher. A confirmation of the above mechanism is given by the behavior of the samples annealed in O_2 environment. As already discussed in section 2.3, O_2 strongly decreases the content of Si-C bonds in the SiOC films, leading to a PL emission which is dominated by radiative defects; as a consequence, Eu^{2+} ions formation in Eu-doped films is strongly inhibited, and only a weak PL signal is observed. Figure 3.20 evidences a very steep increase of the PL intensity of Eu-doped films by increasing the annealing temperature in N_2 ambient. This implies an enhancement of the luminescence intensity at 440 nm (in correspondence to the Eu peak emission) in Eu-doped samples which is by a factor of 15 for an annealing temperature of 900 °C.

Figure 3.21 reports the room temperature PLE spectra of undoped and Eu-doped SiOC with an Eu concentration of $1.5 \cdot 10^{20}$ cm^{-3}, both annealed at 900 °C in N_2, obtained by integrating the PL spectra measured by exciting in the 260-370 nm wavelength range.

The PLE curve of Eu-doped SiOC (blue line and squares) is characterized by a monotonic decrease by increasing the excitation wavelength. It must be noticed that SiOC:Eu PLE spectrum appears quite different from the typical excitation spectrum of Eu^{2+} ions, shown in the inset. Furthermore, since the PLE spectrum of Eu-doped SiOC has a similar behavior with respect to the one of undoped SiOC (shown in figure 3.21 as red line and circles), which monotonically decreases by increasing the excitation wavelength, it is possible to conclude that the
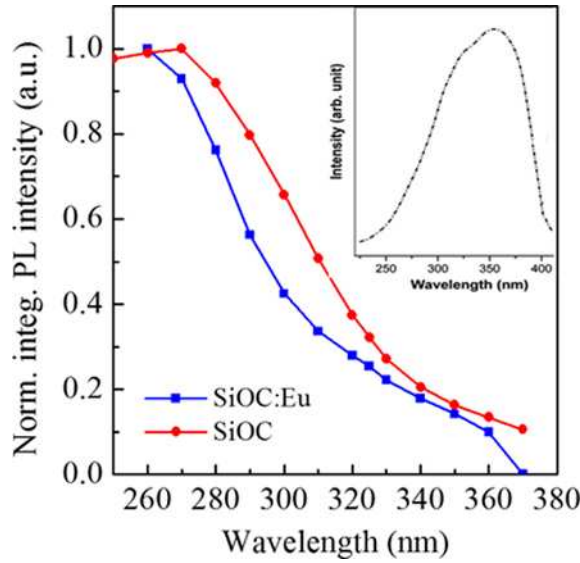
Figure 3.21: *Room temperature PLE spectrum of undoped and Eu-doped SiOC (Eu concentration is $1.5 \cdot 10^{20}$ cm^{-3}) annealed at 900 °C in N_2, obtained by integrating in the range 380-650 nm the PL spectra measured by exciting with wavelengths in the range 260-370 nm. The inset reports the typical PLE spectrum of a Eu^{2+} compound [119].*

SiOC matrix has an active role in the optical properties of Eu-doped SiOC. We can reasonably exclude that this role consists in the presence of a SiOC emission, since the spectral shape shown in figure 3.16 for an excitation wavelength of 325 nm does not appreciably change by changing the excitation wavelength, even by using the wavelengths which maximize a possible SiOC emission. We could therefore suppose the existence of an energy transfer mechanism between the Si-C bonds that act as absorber for the UV radiation, and the Eu ions dispersed into the SiOC matrix. To elucidate the mechanism, a schematic view of the energy levels involved is provided in figure 3.22. An excitation

photon at 325 nm (red arrow) is absorbed by N_2 annealed SiOC:Eu sample, where there are Si-C bonds able to promote Eu ions in the divalent oxidation state. The Eu^{2+} ions can be excited by an energy transfer (dashed black arrow) from the excited levels of SiOC. In their characteristic lifetime of the order of μs, 5d $\longrightarrow$ 4f transitions of Eu^{2+} ions occur, emitting photons at 440 nm (blue arrow). Therefore the efficient absorption properties of SiOC in the short wavelength region can be exploited to excite the Eu^{2+} ions and to enhance their PL efficiency also at short excitation wavelengths.
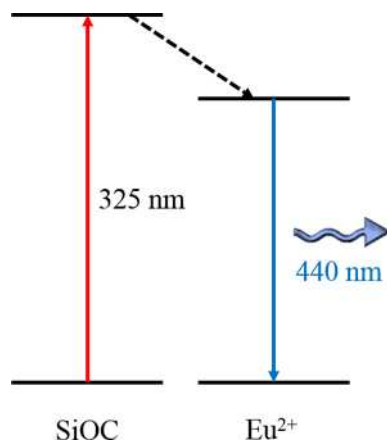
Figure 3.22: *Schematic view of the energy transfer mechanisms between the SiOC matrix and the Eu^{2+} ions. An excitation photon at 325 nm excites the matrix which relaxes non-radiatively to the excited levels of Eu^{2+} that relax to its ground state emitting a photon at 440 nm.*

In conclusions, the results obtained on Eu-doped SiOC demonstrate that the SiOC matrix acts at the same time (1) as a fully Si-compatible host matrix in which the solubility of Eu ions is enhanced with respect to pure SiO_2, (ii) as reducing agent which promotes Eu^{3+} reduction into Eu^{2+} and (iii) as an efficient absorber material, able to enhance the PL efficiency of Eu^{2+} ions.

3.5   How to make Eu-doped SiOC a white light emitter: the bilayer approach

As discussed in section 3.1 and illustrated in figure 3.4, one of the properties of Eu-doped materials is the dependence of Eu^{2+} emission peak wavelength on the crystal field of the host matrix. The possibility to tune the Eu^{2+} emission by changing the host matrix or the Eu concentration has been previously demonstrated [92, 108, 120], and represent a very interesting feature for light source development. Furthermore, in section 3.4 we evidenced a dependence of the Eu^{2+} emission wavelength on the local Eu concentration in the film. With the aim of elucidating the dependence of the PL emission on the total Eu concentration, SiOC thin films doped with different Eu concentrations have been synthesized by rf magnetron sputtering system. The deposition has been obtained, similarly to what already described in section 3.2, by the co-sputtering of SiO_2, SiC and Eu_2O_3 targets. Layers 120 nm thick, having a fixed C concentration of about 5 at.%, but characterized by four different Eu concentrations ($2.0 \cdot 10^{20}$, $1.8 \cdot 10^{21}$, $3.0 \cdot 10^{21}$ and $4.9 \cdot 10^{21}$ Eu/cm^3), have been grown by properly changing the power applied to the Eu_2O_3 target.

In figure 3.23 the normalized room temperature PL spectra of SiOC films doped with 4 different Eu concentrations are shown. All of the samples have been annealed at 600 °C in N_2 ambient. The PL peaks are remarkably shifted one another and approximately cover the whole visible range; the maxima are found at about 435, 535, 560 and 585 nm and, as expected, longer wavelengths correspond to higher Eu concentrations [92, 108, 120]. No marked variation of the wavelength of the emitted photons is found for annealing temperatures ranging from 600 to 900 °C, so that the capability of the Eu-doped samples to exhibit an emission covering the whole visible region holds in a wide range of annealing temperatures.
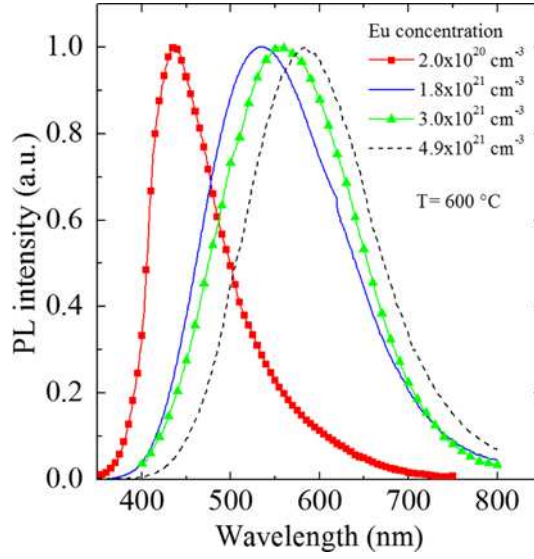
Figure 3.23: *Room temperature normalized PL spectra for Eu-doped SiOC films containing four different Eu concentrations, annealed at 600 °C.*

Eu-doped SiOC films therefore represent a class of light emitting materials exhibiting an intense room temperature PL which can be tuned from the blue to the red by simply changing the Eu concentration. This property implies that the combination in the same multilayer of a few SiOC layers, in which the Eu concentration has been properly varied, may produce the emission of white light. In order to test the potentialities of Eu-doped SiOC layers as an efficient white light source, a bilayer consisting of two SiOC films with different Eu contents ($3.0 \cdot 10^{21}$ Eu/cm^3 in the layer in contact with the Si substrate, $2.0 \cdot 10^{20}$ Eu/cm^3 in the surface layer), has been grown by sputter deposition, as schematically shown in the inset of figure 3.24. The layers sequence has been chosen in order to avoid that photons emitted from the lower layer (emitting at lower energy) can be absorbed by the up-

per one. Figure 3.24 reports the Eu depth profile in the as-deposited SiOC bilayer (red line and squares), as extracted by RBS; the profile is characterized by a steep variation of the Eu concentration at a depth corresponding to the interface between the two layers, demonstrating that no intermixing phenomena occurred. As discussed in section 3.4, a thermal annealing process in N_2 ambient is a necessary step in order to make Eu-doped SiOC layers efficient light emitters at room temperature. However, thermal treatments do not modify the Eu depth profile, this is clear from figure 3.24, in which Eu depth profile of Eu-doped SiOC annealed at 800 °C (blue line) overlaps the Eu depth profile of the as-deposited sample (red line and squares).

Furthermore, the films exhibit a marked dependence of the PL intensity on the annealing temperature and, in particular, 900 °C is the temperature which maximizes the PL intensity. However, since the bilayer consists of two films containing very different Eu concentrations and a dependence of the optimal annealing temperature on the Eu concentration is expected, we have studied in detail the room temperature PL emission of the bilayer as a function of the annealing temperature. The results are shown in figure 3.25 for bilayers as-deposited and annealed at temperatures ranging between 600 and 900 °C. The PL spectrum of the as-deposited bilayer consists of a very wide band, covering almost all the visible range, exhibiting a maximum at about 570 nm. Thermal annealing processes in the 600-800 °C range induce some modifications of the shape of the PL peak and remarkably increase its intensity.

More in detail, as shown in figure 3.26 the integrated PL intensity at 600, 750 and 800 °C is about a factor of 2, 3 and 4, respectively, higher with respect to the as-deposited sample. The peak shape modification mainly involves an increased contribution at shorter wavelengths so that, even if two maxima (at about 475 and 570 nm) are visible at 750 and 800 °C, an almost flat emission in the whole visible range is obtained. In fact, the sample annealed at 800 °C shows a
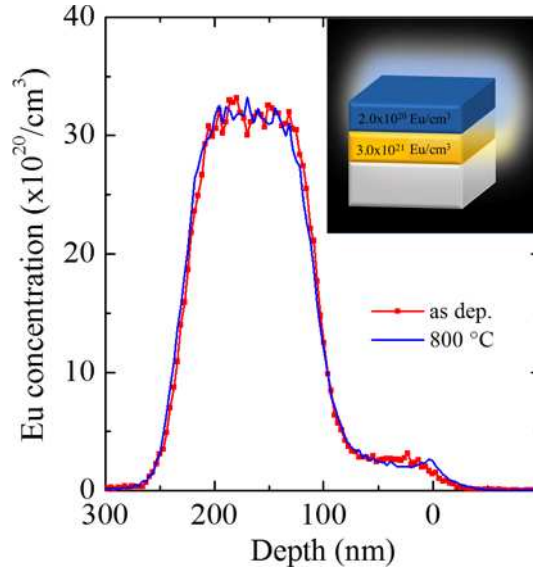
Figure 3.24: *Eu depth profiles, as extracted from the RBS spectra, in a bilayer consisting of two SiOC films with a different Eu concentration ($3.0 \cdot 10^{21}$ Eu/cm^3 in the lower layer, $2.0 \cdot 10^{20}$ Eu/cm^3 in the upper layer), as-deposited (red line and squares) and annealed at 800 °C (blue line). The bilayer structure is schematically shown in the inset.*

PL emission that appears white if observed by naked eye as in the inset of figure 3.25 is shown. From the comparison with the data in figure 3.23, it is straightforward to assign the component exhibiting the short-wavelength maximum to the layer with $2.0 \cdot 10^{20}$ Eu/cm^3 and the other one to the layer with $3.0 \cdot 10^{21}$ Eu/cm^3.

Figure 3.25 shows that at 900 °C the PL spectrum of the bilayer is remarkably different with respect to those observed at lower temperatures: indeed, although figure 3.26 demonstrates that this thermal process is able to produce a further increase of the integrated PL intensity, at this annealing temperature the short wavelength contribution
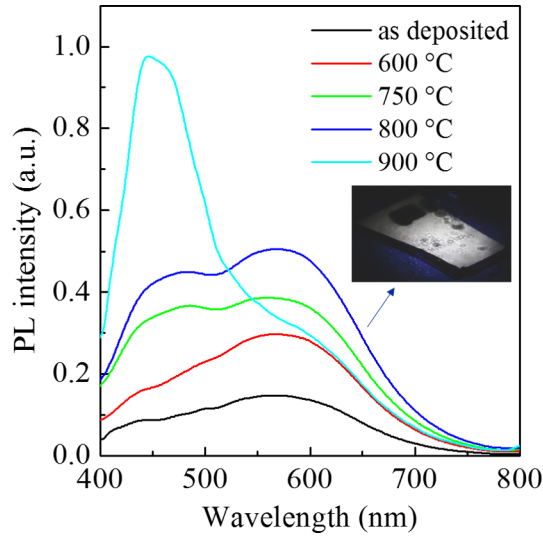
Figure 3.25: *Room temperature PL spectra for an Eu-doped SiOC bilayer, as-deposited and annealed in the 600-900 °C range. The inset shows the photograph of the sample annealed at 800 °C, having an area of about 1 cm?2, excited by 364 nm line of a fully defocused Ar$^+$ laser beam, showing a bright white PL emission cleary visible by the naked eye.*

strongly increases at the expenses of the long wavelength one, so that the very wide emission characterizing samples as-deposited and annealed up to 800 °C is not present anymore, being replaced by a PL signal markedly peaked at 450 nm and exhibiting a shoulder at longer wavelengths.

In order to gain deeper information on the nature of the observed PL emission, in figure 3.27 the PL spectrum of the bilayer annealed at 800 °C (black line) is compared with that of the single layers containing $2.0 \cdot 10^{20}$ Eu/cm^3 (blue line) and $3.0 \cdot 10^{21}$ Eu/cm^3 (red line), annealed at the same temperature. Although SiOC is able to strongly increase the Eu solid solubility with respect to the more conventional SiO$_2$ matrix,
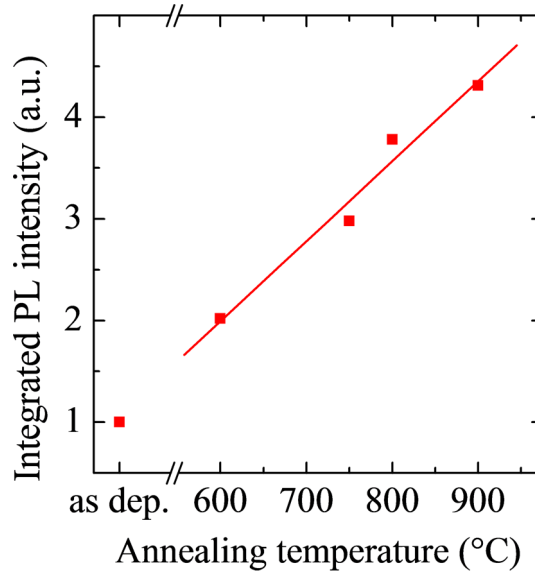
Figure 3.26: *Dependence of the integrated multilayer PL intensity on the annealing temperature. The line is drawn to guide the eye.*

the thermal process performed at temperatures of 800 °C or higher is critical and may lead to Eu precipitation (section 3.4). Obviously, films with a higher Eu concentration are more sensitive to an increase of the annealing temperature. This is evident in figure 3.27, where the spectrum peaked on the long wavelength side (corresponding to the single layer with the highest Eu concentration, plotted as a red line) is less intense by a factor of 4 with respect to that of the single layer with the lowest Eu concentration (blue line), while the two spectra have the same intensity for an annealing temperature of 600 °C. This effect occurs because films with $2.0 \cdot 10^{20}$ Eu/cm^3 are able to benefit of the increased thermal budget to improve the chemical environment of Eu ions without the occurrence of precipitation processes, while this phenomenon is unavoidable at higher Eu concentrations.
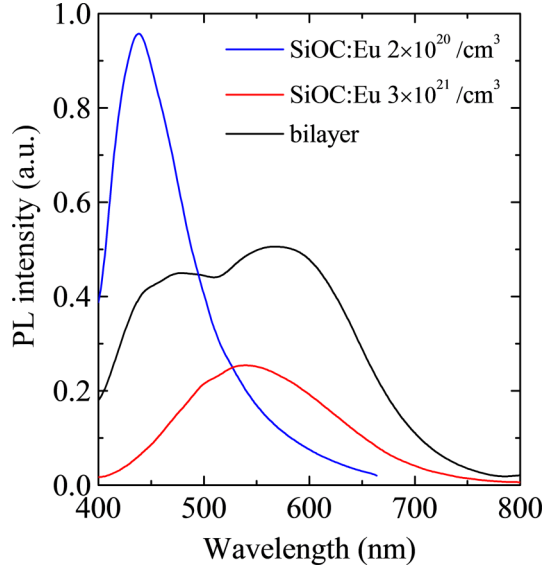
Figure 3.27: *PL emission spectra of $2.0 \cdot 10^{20}$ Eu/cm^3 (red line) and $3.0 \cdot 10^{21}$ Eu/cm^3 (blue line) single layers and of multilayer (black line) annealed at 800 °C.*

A different picture occurs when we couple these two single layers to form the bilayer sample: looking at the spectrum of the bilayer in figure 3.27 (black line) and comparing with those of the single layers annealed in the same conditions, the PL contribution due to the layer with the lowest Eu concentration and peaked at 440 nm seems to be reduced by a factor of 2, while the spectrum corresponding to the layer with the highest Eu concentration seems to be enhanced approximately by the same factor. The loss of signal at shorter wavelengths, can be understood if we consider that the upper layer in not in contact with a reflective Si substrate, which acts as a mirror for emitted photons in the case of single layer. On the other hand the lower layer ($3.0 \cdot 10^{21}$ Eu/cm^3) absorbs not only the photons from the excitation

laser, but also those at 440 nm emitted backwards from the upper layer ($2.0 \cdot 10^{20}$ Eu/cm^3), experiencing a more efficient excitation. This sort of gain-and-loss of total energy, give us the spectrum of the bilayer annealed at 800 °C with the desired flat behaviour in almost all the visible range.

The analysis of figure 3.25 suggests that, by excluding the sample annealed at 900 °C, which is characterized by an emission strongly peaked in the blue region, all the other PL spectra seem to be qualitatively close to a white emission. In order to quantitatively evaluate the emission spectra of the bilayer, we have calculated the Commission International de l'Eclairage (CIE) chromaticity coordinates for all the annealing temperatures. The emission closest to the white is obtained at 800 °C. In figure 3.28 the open dot indicates the CIE coordinates of this sample, which are (0.33, 0.36), to be compared with those relative to an ideal white emission which are (0.33, 0.33). Figure 3.28 also reports as solid squares the CIE chromaticity coordinates relative to the two Eu-doped SiOC single layers having the same Eu concentration as those forming the bilayer, both annealed at 800 °C; as expected, the point relative to the bilayer fairly lies on the straight line connecting the points corresponding to the single layers. From the CIE coordinates it is also possible to calculate the correlated color temperature (CCT) of the emission, which is 5140 K. CCT is typically used to classify the light emitted by commercial LEDs and lamps. It is also possible to evaluate the CRI. For the Eu-doped SiOC bilayer annealed at 800 °C the calculated CRI has a very high value of 91/100, which mirrors the broadband nature of the Eu^{2+} emission.

These data demonstrate the feasibility of a bilayer consisting of two SiOC thin films doped with different Eu concentrations which, after a proper tuning of the annealing temperature, represents an efficient emitter of white light at room temperature.
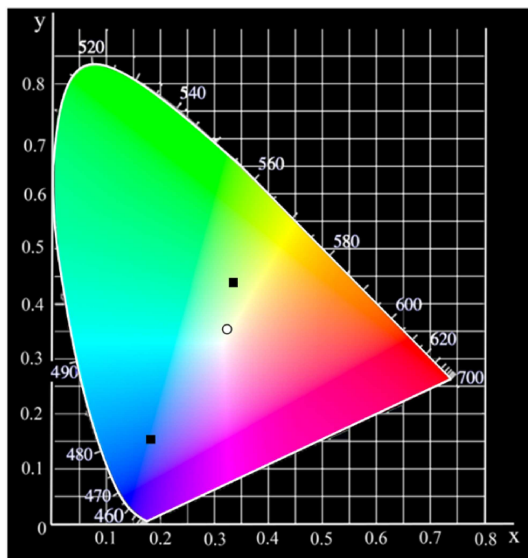
Figure 3.28: *CIE chromaticity coordinates for the Eu-doped SiOC bilayer (open dot) and for the corresponding Eu-doped SiOC single layers (solid squares); all of the samples have been annealed at 800 °C.*

3.6   Conclusions

In this chapter, limits and perspectives of pure SiO_2 and SiOC matrices as a host for optically active Eu ions have been presented and discussed. In the case of SiO_2, both Eu^{2+} or Eu^{3+} emissions have been obtained, but the occurrence of an extensive Eu precipitation in thermally annealed films seems to be unavoidable. The formation of Eu-containing clusters has been studied in a great detail, and the role played by the temperature and by the chemical environment during the thermal treatment elucidated. Although some strategies to minimize clustering phenomena and to improve the efficiency of the light emission process have been proposed, the material remains quite far

from requirements for practical applications.

On the other hand, a SiOC matrix is able to efficiently promote the $Eu^{3+} \longrightarrow Eu^{2+}$ reduction, so enriching the system with the Eu species exhibiting the brightest luminescence. Furthermore, TEM and RBS data have demonstrated that Eu ions in SiOC are characterized by an enhanced mobility and solubility; this peculiarity leads to a strongly reduced Eu precipitation, and, as a consequence, to a very intense and stable light emission at about 440 nm from Eu^{2+} ions. Accordingly, our data demonstrate that an increase of the luminescence intensity at 440 nm accounting for about a factor of 15 can be obtained in Eu-doped films in comparison with undoped SiOC. We have also found evidences of the occurrence of an energy transfer mechanism between the SiOC matrix and the Eu^{2+} ions which, by increasing the efficiency of photon absorption for exciting wavelengths shorter than 300 nm, further contributes to increase the optical efficiency of Eu-doped SiOC layers.

Furthermore we have demonstrated the feasibility of a bilayer consisting of two SiOC thin films doped with different Eu concentrations which, after a proper tuning of the annealing temperature, represents an efficient emitter of white light at room temperature with optimal characteristics especially in color rendering.

In conclusion, Eu-doped SiOC layers may find an application as the active layer in light emitting devices to be employed in Si photonics. On the other hand, the white color of the light emitted from Eu-doped SiOC bilayers suggests also very interesting applications in solid-state lighting.

Chapter 4

Overcoming the limits of Eu doping: the Eu compound approach

In this chapter we investigate the structural, chemical and optical properties of Eu compounds synthesized by thermal processing of Eu_2O_3 thin films deposited by RF magnetron sputtering on Si substrates.

Structural characterization of the films has been performed by transmission electron microscopy (TEM) and x-ray diffraction (XRD), which revealed that thermal processes in O_2 ambient induce an oxidation process in correspondence of the Eu_2O_3-Si interface. The formation of a Si oxide layer at the interface acts as a diffusion barrier between Eu_2O_3 and Si, preventing the reaction between them and leaving almost unaffected most of the Eu_2O_3 layer. Accordingly, photoluminescence (PL) measurements revealed the typical red emission of Eu^{3+} ions.

On the other hand, by changing the annealing environment from O_2 to N_2, no diffusion barrier is formed and TEM data evidence the occurrence of a complex reactivity at the Eu_2O_3/Si interface, which leads to the formation of stable Eu^{2+} silicates. The $Eu^{3+} \rightarrow Eu^{2+}$ reduction,

due to the chemical reaction with Si atoms from the substrate, has been confirmed by XRD analyses of the crystalline structure formed after thermal treated samples. PL measurements performed on N_2 treated samples reveal a very strong (the measured external quantum efficiency is about 10%) and broad room temperature emission peaked at 590 nm. This signal is much more intense (more than three orders of magnitude) than the Eu^{3+} one observed in O_2-annealed films.

These results demonstrate that the control of the annealing conditions of Eu_2O_3 thin films allows one to obtain different Eu compounds emitting in the visible range, having great potentialities for applications in photonics and in solid-state lighting.

4.1 Rare earth compounds: a new route to overcome clustering phenomena

In the previous chapter, the Eu doping approach to obtain efficient rare earth (RE)-based light emitting materials has been presented and discussed. RE doping of suitable insulating or semiconducting host matrices has been considered for a long time one of the best method to obtain light emission from Si-based materials [121]; however, due to the low solid solubility of RE in most of Si-based matrices [49, 53, 95–97, 103, 106], RE clustering and precipitation, leading to a reduced optical efficiency, occur in doped materials. It has been demonstrated [111] that the compound approach, being able to overcome these problems, may open some new and interesting perspectives for the application of RE in Si photonics [95]. Indeed a RE concentration of the order of $1 0 \cdot 22$ at/cm^3 can be reached in a compound, so potentially increasing by a factor of about 10^3 the number of luminescent centers. In recent years most of the efforts on these compounds have been focused on Er silicate thin films; relevant results include the

observation of energy transfer between Si nanostructures and Er ions in an Er silicate film [122], the achievement of optical gain in Er/Y silicate waveguides [123], and the observation of a very efficient Er/Yb coupling in mixed silicates [124]. Also photon cutting phenomena, being of great relevance for possible photovoltaic applications of these materials, have been demonstrated in Er/Y silicates [124].

Among the various RE, the intense and stable room temperature emission in the visible region exhibited by Eu ions incorporated in different host matrices has been studied and successfully applied in several technological fields, such as phosphors. On the other hand, research on Eu compounds seems to be at a less advanced level, although their optical properties have been exploited in simple prototypes of light emitting devices [48].

4.2   Properties of Eu compounds

Among the RE compounds, a considerable attention has been devoted to oxides and to silicates, which are the most common RE minerals found in nature. Research has been mainly focused on their synthesis and structure, so that in many cases their physical properties are not fully understood, suggesting that a deeper knowledge of these materials is needed.

RE oxides are very important, because they are the starting compounds for the synthesis of most of the RE-based materials used in many different technologies field. Furthermore, RE mixed oxides are widely used for high temperature superconductors, ferroelectric materials and as low dielectric constant materials.

From the mixture between SiO_2 and RE oxides it is possible to form a RE silicate which is a chemically stable RE compound. The number of possible crystalline structures of RE silicates is very high, due to the fact that polymorphism is a common feature. Indeed in these materi-

als the formation of a particular crystalline structure tightly depends on the technique used for the synthesis and above all on the thermal history. Generally the formation temperature of a phase and the transition temperature between two different phases both increase with the atomic radius of the RE, owing to the fact that higher energies are needed to allow the diffusion of the RE ions and their accommodation in the lattice sites in order to form the crystalline structure.

The most studied silicates are those in which RE ions are in their trivalent oxidation state, as in Er silicates [122]. However, attention has been also devoted to the silicates containing divalent REs ions, such as Eu^{2+}. Several divalent Eu silicates exist, as shown in the phase diagram of the binary system EuO-SiO_2 reported in figure 4.1. The existence of Eu^{2+} silicates, such as the orthosilicate Eu_2SiO_4 and the metasilicate $EuSiO_3$, has been established. Other important Eu^{2+} silicates are $Eu_3Si_2O_7$ and Eu_3SiO_5 [125, 126].

The preparation of pure Eu silicate crystals needs high temperature processing [128, 129]. For example, bulk Eu2SiO4 crystals have been prepared at high temperature by chemical transport reaction [130]. In particular, *Kaldis* et al [131] have performed a process at 1800 °C using HCl as a transport gas. Also $EuSiO_3$ crystals synthesis have been achieved by using processes at high temperature (about 1400 °C) [132].

The synthesis of Eu^{2+} silicates described above are therefore not compatible with most of the modern technologies, because they are not able to produce materials in the form of thin films and require very high temperatures. On the other hand, the optical properties of Eu^{2+} silicates, which have been investigated in several works [126, 131? – 135], could become very interesting for application requiring efficient light emitting materials, such as photonics and lighting.

Recently, new Eu^{2+} silicates fabrication processes have been developed. An example has been provided by *Qi* et al. [70], who have grown Eu silicate thin films by sputtering of Si and $EuSi_2$ targets on a
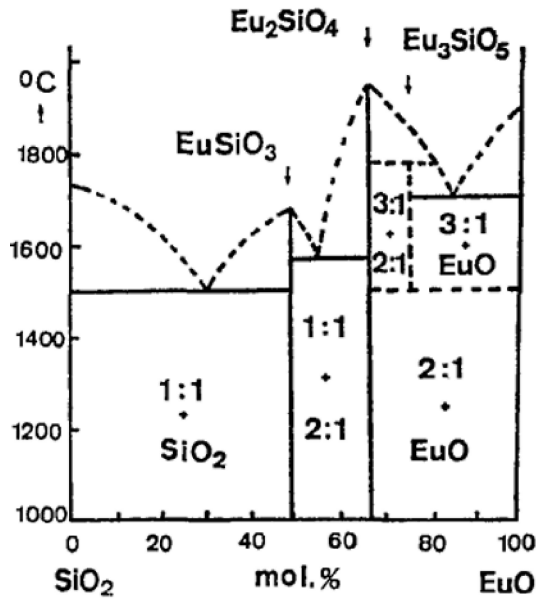
Figure 4.1: *Phase diagram of the SiO_2/EuO system [127].*

Si substrate. The formation of $EuSiO_3$ and Eu_2SiO_4 compounds have been demonstrated by x-ray photoelectron spectroscopy. The obtained polycrystalline film has been excited electrically and exhibits a broad emission in the 400-800 nm range, which has been assigned to the transitions of Eu^{2+} ions. However, the true mechanism leading to the observation of electroluminescence (EL) from a very thick (about 2 μm) insulating film remains quite unclear.

Eu^{2+} silicates light emission has been also obtained by *Li* et al. [97] from Eu-doped Si-rich Si oxide films deposited by electron beam evaporation and subsequently annealed at different temperatures. The authors have found that the luminescence is due to radiative defects of the oxide for samples annealed at low temperature and to the 4f^{6}5d-4f^7 transition of Eu^{2+} ions in $EuSiO_3$ when the films are annealed at

temperatures higher than 800 °C (figure 4.2). This transition is confirmed also by the evolution of photoluminescence (PL) decay lifetime as function of the annealing temperature shown in the inset of figure 4.2 for temperatures higher than 800 °C the decay time strongly increases, indicating a change in the nature of the emitting centers.
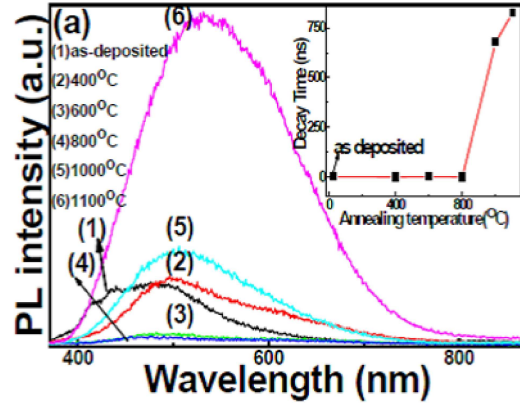
Figure 4.2: *PL of Eu:SiO$_x$ films as a function of the annealing temperature. The inset shows the dependence of the PL decay-time on the annealing temperature [97].*

In this chapter a new synthesis of divalent Eu silicates, consisting of an Eu$_2$O$_3$ thin film deposition on a Si substrate followed by a proper thermal treatment, is proposed. After a short discussion on the properties of Eu$_2$O$_3$ films, Eu^{2+} silicates formation and properties will be investigated in detail. In particular, the evolution of their structural properties upon thermal annealing will be studied and correlated with the characteristics of the PL emission in the visible region. The conditions leading to a material exhibiting a very efficient room temperature light emission, associated to the massive formation of Eu^{2+} ions, will be identified.

4.3   Synthesis of Eu compound thin films

Eu_2O_3 thin films, about 120 nm thick, have been deposited by using the UHV magnetron sputtering system already described in the previous chapters. The chamber base pressure was about $1 \cdot 10^{-9}$ mbar. The deposition has been obtained by RF sputtering of a 4 inches diameter water-cooled Eu_2O_3 target (99.9% purity). The films have been deposited on Si substrates kept at a temperature of 400 °C. The deposition was carried out with a sputter up configuration in a $5 \cdot 10^{-3}$ mbar Ar atmosphere and a RF power of 200 W for 1 h. After deposition samples were thermally treated in O_2 or N_2 ambient at temperatures ranging from 600 to 1100 °C; a rapid thermal annealer was used for annealing times ranging from 1 to 300 s while a conventional horizontal furnace was used for thermal treatments of 1 h. The structural and optical properties of both as deposited and annealed films have been studied by x-ray diffraction (XRD), transmission electron microscopy (TEM), energy filtered transmission electron microscopy (EFTEM) and PL measurements.

XRD analyses were performed with a Bruker-AXS D5005 diffractometer by grazing incidence of a Cu K_α radiation.

Bright field and dark field TEM images were carried out with a 200 kV Jeol 2010 microscope, while EFTEM images were performed with a 200 kV Jeol 2010F equipped with a Gatan Image Filter. PL measurements were performed by pumping with the 325 nm line of a He-Cd laser. The pump power was about 3 mW and the laser beam was chopped through an acousto-optic modulator at a frequency of 55 Hz. The PL signal was wavelength dispersed by a single grating monochromator and detected with a Hamamatsu visible photomultiplier. Spectra were recorded with a lock-in amplifier using the acousto-optic modulator frequency as a reference. All the spectra have been measured at room temperature (RT) and corrected for the system spectral response. PL lifetime measurements were performed by mon-

itoring the decay of the luminescence signal at a fixed wavelength after pumping to steady state and switching off the laser beam. The overall time resolution of our system is of 200 ns. Photoluminescence excitation (PLE) measurements in the 250-500 nm range were performed by using a FluoroMax spectrofluorometer by Horiba.

4.4   Optical and structural properties of Eu$_2$O$_3$ thin films

Figure 4.3 reports the BF XTEM image of an as-deposited Eu$_2$O$_3$ film grown on a Si substrate by magnetron sputtering. The film, about 120 nm thick, is polycrystalline and exhibits a smooth interface with the Si substrate. A native SiO$_2$ layer ($\sim$ 2 nm thick) is present at the interface between the film and the substrate.

Figure 4.3: *XTEM image of as-deposited Eu$_2$O$_3$ thin film on a Si substrate. The arrow indicates the 2 nm thick native SiO$_2$ layer.*

In order to optimize its optical and structural properties, the as-deposited film has been thermally treated. It should be taken into account that one of the main problems when dealing with RE oxides is their chemical reactivity with Si. In fact, interfacial reactions occur when RE oxide thin films are thermally treated at high temperatures.

Furthermore, annealing ambient plays an important role to control the reaction between RE oxides and Si. This phenomenon is evident by comparing figure 4.3 with figures 4.4a and 4.4b, where bright field XTEM images of an Eu_2O_3 film annealed at 1000 °C in O_2 for 1 h and 30 s, respectively, are shown. It is evident that the thermal process has induced relevant structural modifications.
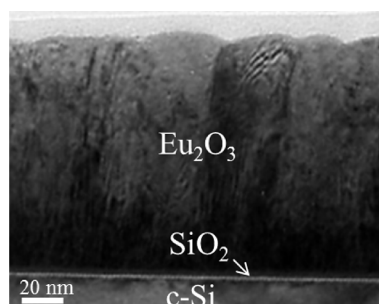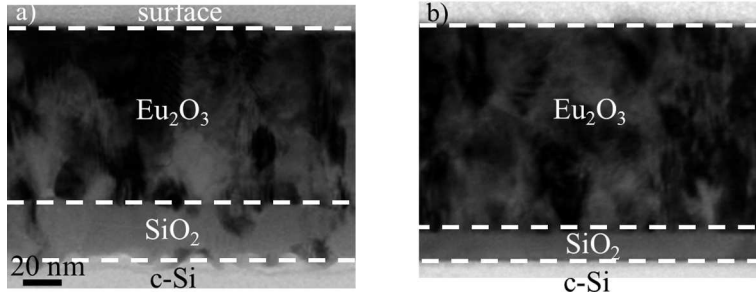

Figure 4.4: *XTEM image of as-deposited Eu_2O_3 thin film on a Si substrate. The arrow indicates the 2 nm thick native SiO_2 layer.*

Considering the sample annealed for 1 h (figure 4.4a), the resulting film is about 140 nm thick, has an increased interface roughness, and it is composed by two distinct layers, one at the surface and the other at the interface with the Si substrate, having a thickness of $\sim$ 100 and 40 nm, respectively. Similar results can be observed in the film annealed for 30 s (figure 4.4b), where, due to the shorter annealing time, the interfacial layer is thinner by about a factor of 2. We can conclude that the result of the thermal process performed in O_2 atmosphere is an oxidation process, which corresponds to an increment of the interfacial SiO_2 layer thickness. In order to study the films structural properties after the O_2 thermal treatment, dark field XTEM have been performed on the sample annealed for 1 h and are shown in figure 4.5a. The film appears to be polycrystalline, and it is possible to distinguish two different layers, similarly to what observed

in figure 4.4a. To investigate the chemical composition of the two layers, EFTEM analysis have been performed on the same sample. By using the 3-windows method, chemical maps of O, Eu and Si have been obtained by using the K edge of O at 532 eV, the NIV edge of Eu at 132 eV and the L$_{II,III}$ edge of Si at 99 eV. From the analysis of the chemical maps (not shown) we note that Eu and O are present throughout the film thickness. On the other hand, as shown in the Si map reported in figure 4.5b, Si is present only in the interfacial layer while in the surface layer only Eu and O are present. This suggests us that the upper layer corresponds to a crystalline Eu$_2$O$_3$ film, while the simultaneous presence of the 3 elements in the interfacial layer demonstrates the occurrence of a mixing between film and substrate, induced by the high temperature annealing. In fact the thermal process induces at the same time O$_2$ diffusion from the annealing ambient throughout the film, a reaction between O and the Si substrate to form SiO$_2$, and the increment of Eu mobility, leading to a diffusion of Eu into the SiO$_2$ layer.
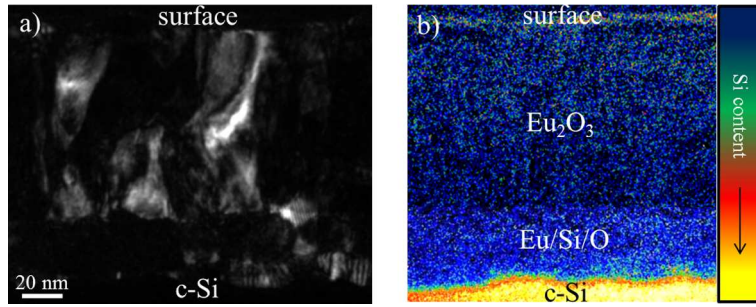

Figure 4.5: *TEM analysis of Eu$_2$O$_3$ film annealed at 1000 °C for 1 h in O$_2$: (a) cross-section dark field TEM image and (b) chemical map of Si, obtained by using L$_{II,III}$ edge of Si at 99 eV.*

A detailed study of the crystalline structure of the annealed Eu$_2$O$_3$ films was performed by XRD. By grazing angle incidence ($\theta = 1°$)

measurements, a XRD spectrum in the range of diffraction angles (2θ) from 18° to 60°, is obtained. In figure 4.6 the diffraction spectra for a Eu_2O_3 film deposited on Si and annealed at 1000 °C for 1 h (black line) and 30 s (blue line) are shown. Almost all the peaks of the spectra, marked with red circles, are related to the monoclinic Eu_2O_3 phase, for both the annealed samples.
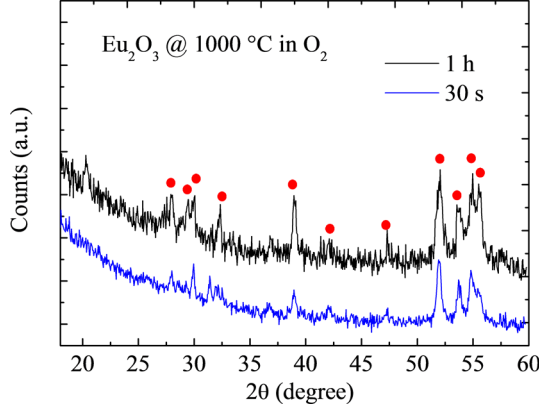
Figure 4.6: *XRD spectrum for Eu_2O_3 films annealed in O_2 at 1000 °C for 1 h (black line) and 30 s (blue line). The peaks labelled with red dots are related to the monoclinic Eu_2O_3 phase.*

In spite of the high reactivity of Eu ions towards Si and O to form Eu silicates, XRD analysis does not allow to identify any specific Eu/Si/O phase; in the absence of any clear XRD signature, we have to conclude that the interfacial layer is essentially an amorphous Er/Si/O mixture.

It is well known that annealing treatments in O_2 ambient can improve the optical properties of RE oxide thin films, due to the reduction of the defect density and to the optimization of oxide stoichiometry [136]. We have studied the room temperature light emission of Eu_2O_3 films deposited on Si substrates by pumping with the 325 nm

line of a He-Cd laser with a pump power of 3 mW. The emission spectrum, shown in figure 4.7 for samples as-deposited and annealed at different temperatures (in the 600-1000 °C range) is the one typical of Eu^{3+}.
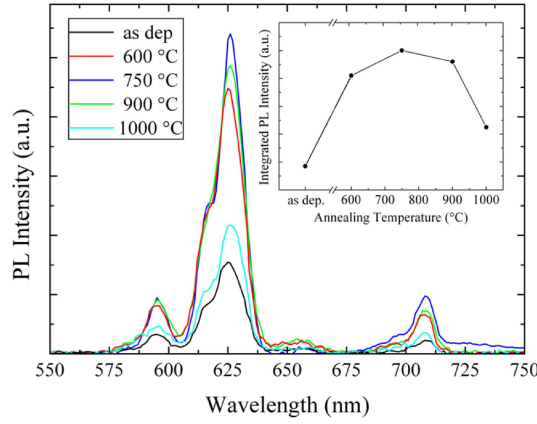
Figure 4.7: *Room temperature PL spectra for Eu$_2$O$_3$ films as-deposited and annealed in O$_2$ at temperatures in the 600-1000 °C range. In the inset the dependence of the integrated PL intensity on the annealing temperature is shown.*

For all the annealing temperatures the main peak, corresponding to the $^5D_0 \rightarrow {}^7F_2$ transition, is detected at 622 nm, with a FWHM of about 10 nm. The other less intense peaks at about 595, 655 and 708 nm correspond to $^5D_0 \rightarrow {}^7F_J$ transitions of Eu^{3+} ions in solid matrices, with J = 1, 3 and 4, respectively. Although the shape of the PL spectra appears almost unchanged at the various annealing temperatures, a variation of the peak intensity (as shown in the inset of figure 4.7) is present. All the thermal treatments lead to higher PL intensities with respect to the as-deposited sample. More in detail, although the maximum PL signal is reached at 750 °C (this signal is higher by about a factor of 3 than that of the as-deposited film), the

PL intensity remains almost constant within a quite wide temperature range (600-900 °C); a noticeable decrease by about a factor of 2 is finally seen at 1000 °C, due to a loss of optically active Eu ions into the layer formed at the Eu_2O_3/Si interface, as demonstrated by figures 4.4 and 4.5. We can conclude that the increment of PL intensity observed for annealing temperatures in 600-900 °C range is related to an improvement of the Eu^{3+} crystalline environment and to a reduction of the defects density (that quench the Eu^{3+} emission), both due to the O_2-thermal treatment.

These data allow us to understand the specific chemical role played by the annealing environment in the thermal evolution of Eu_2O_3. Indeed, the presence of O_2 activates a process of oxidation of the Si surface; this process competes with the Eu_2O_3/Si reaction and slows it down, as demonstrated by the fact that, also after a long annealing process at 1000 °C, most of the Eu_2O_3 film is unaffected. Therefore, O_2 annealing treatments produce an Eu_2O_3 thin film with optimized stoichiometry and structure, and with optical features fully compatible with the presence of Eu^{3+} ions.

4.5   From Eu_2O_3 to Eu^{2+} silicates thin films

In order to further investigate the role of the annealing ambient in determining the structural and optical properties of Eu_2O_3 thin films, samples have been also annealed in N_2 ambient at temperatures between 900 and 1100 °C and for times in the 1 - 300 s range. Figure 4.8a shows the BF XTEM images of the sample annealed at 1000 °C for 30 s. After the thermal process, the Eu_2O_3 film becomes thicker (about 170 nm), and two sublayers, labeled in the figure as A (surface sublayer) and B (interfacial sublayer), can be distinctly recognized. EFTEM measurements indicate that none of the two sublayers is pure SiO_2. Indeed, in absence of any interfacial SiO_2 layer acting as dif-

fusion barrier as in the case of O$_2$-annealed sample (figure 4.4), the strong reactivity between Si and Eu$_2$O$_3$ is activated and Si atoms can diffuse inside the film. This is demonstrated in figure 4.8b, showing the Si, O and Eu chemical maps of the N$_2$-treated film, obtained by EFTEM. The images were taken by selecting electrons which have lost 99 eV in the case of Si (corresponding to the L$_{II,III}$ edge), 532 eV in the case of O (corresponding to the K edge) and 132 eV in the case of Eu (corresponding to the NIV edge). EFTEM data demonstrate that the interface between sublayers A and B evidenced by TEM corresponds to a quite abrupt variation of the concentration of the three elements. In particular, sublayer B is characterized by an appreciable Si concentration and has a higher O content and a lower Eu content than sublayer A.

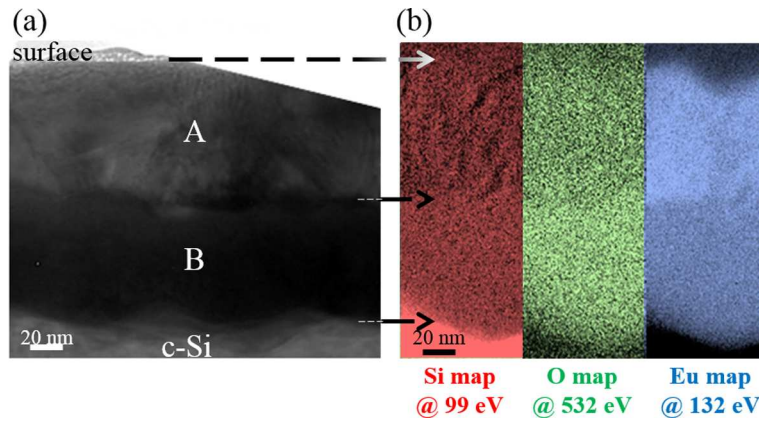**Figure 4.8:** *XTEM images of Eu$_2$O$_3$ films treated at 1000 °C for 30 s in N$_2$. (a) BF image; (b) EFTEM maps of Si (on the left), O (in the middle) and Eu (on the right). EFTEM images refer to the same region of the sample. The arrows highlight the correspondence between the A and B sublayers in the TEM image shown in (a) and the regions with a different composition in the EFTEM images in (b).*

The crystalline structure of the films was studied by XRD. As shown in figure 4.9, the as-deposited film exhibits a diffraction spectrum mainly consisting of peaks belonging to the monoclinic Eu_2O_3 phase [137]. However, also a few peaks belonging to the sub-stoichiometric oxide Eu3O4, accounting for the small O deficiency which may characterize oxide films grown by sputtering, are identified [138]. Figure 4.9 also reports the XRD spectrum of a film treated at 1000 °C for 30 s in N_2; peaks assigned to Eu_2O_3 are still present, but new peaks, corresponding to the monoclinic orthosilicate Eu_2SiO_4 [139], appear. The presence in the XRD spectrum of two different crystalline compounds (Eu_2O_3 and Eu_2SiO_4), coupled with the bilayered structure shown by TEM, suggests that the surface sublayer A mainly contains unreacted Eu_2O_3, since no appreciable Si diffusion occurs in this region. In the interfacial sublayer B the high Si concentration determines a reaction with Eu_2O_3 to form Eu orthosilicate. By increasing the annealing time, the Si diffusion length into the Eu_2O_3 film increases, and Si can therefore more extensively react with Eu_2O_3, as demonstrated by the XRD spectrum of the sample treated at 1000 °C for 300 s in N_2. In this last case, Eu_2SiO_4-related peaks are still present, but also peaks corresponding to the metasilicate $EuSiO_3$ [140] are found, while peaks corresponding to Eu_2O_3 disappeared.

It is strongly remarkable that, in both the silicates detected by XRD (Eu_2SiO_4 and $EuSiO_3$), Eu is in its divalent state, Eu^{2+}, while in the as-deposited film (Eu_2O_3), according to the target composition, almost only Eu^{3+} ions are present. Usually, $Eu^{3+} \longrightarrow Eu^{2+}$ reduction in glasses is accomplished by exploiting gaseous reactants such as H_2 [141] or CO [105]; in the previous chapter we also showed that C contained in SiOC films can act as a reducing agent for Eu^{3+}. In this case, Eu^{3+} reduction is due to a solid-state reaction involving the elemental Si (which, in turn, is oxidized) diffusing inside the Eu_2O_3 film.

A possible explanation for Eu^{2+} silicates formation in N_2-treated
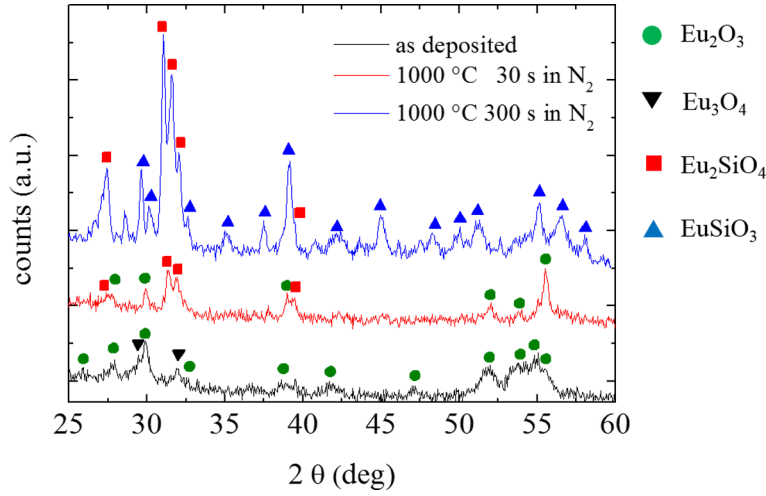
Figure 4.9: *XRD spectra of Eu$_2$O$_3$ films as-deposited and annealed at 1000 °C for 30 s and 300 s in N$_2$.*

Eu$_2$O$_3$ is sketched in figure 4.10. Figure 4.10a represents the annealing process performed for 30 s: Si atoms can diffuse in the region of the film closer to the substrate, react with Eu$_2$O$_3$, and, in agreement with figures 4.8 and 4.9, forms Eu$_2$SiO$_4$, while the surface region is almost unaffected. By increasing the annealing time at 300 s (figure 4.10b), Si concentration in the Eu$_2$O$_3$ film increases, leading to the formation of EuSiO$_3$, in agreement with the SiO$_2$/EuO phase diagram (figure 4.1) and the XRD data of figure 4.9.

Figure 4.11a shows the room temperature PL spectrum of an Eu$_2$O$_3$ sample annealed at 1000 °C in N$_2$ ambient for 30 s (blue line). The sample exhibits a very bright emission, consisting of a broad band (FWHM of about 95 nm) having the maximum at about 590 nm. This broad emission is assigned to the 4f^{6}5d $\longrightarrow$ 4f^7 transitions of Eu^{2+} ions [97, 142], confirming the presence of Eu^{2+} ions in the Eu silicates formed during the N$_2$ annealing treatment, in agreement with

Figure 4.10: *Schematic representation of Eu^{2+} silicates formation during annealing processes for (a) 30 s and (b) 300 s at 1000 °C in N_2.*
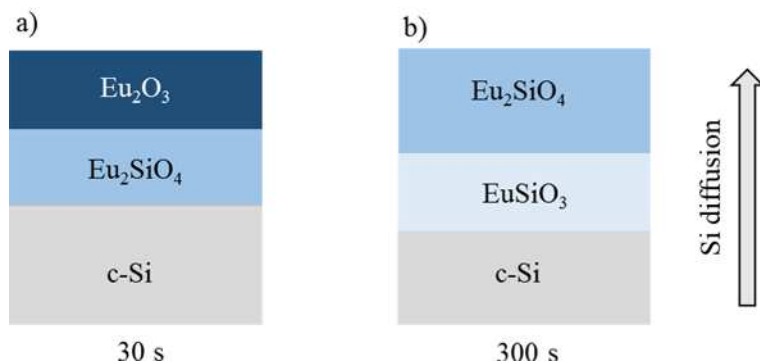
XRD data of figure 4.9. The Eu^{2+} transition is dipole-allowed and produces a very intense PL emission, visible by naked eye, shown in the photo of figure 4.11b. This emission is much more intense (by more than three orders of magnitude) than the forbidden intra-4f transitions characterizing Eu^{3+} ions of the as deposited thin film (green line), as shown in figure 4.11a.

In figure 4.12 the room temperature PL spectra of Eu_2O_3 samples annealed at 1000 °C in N_2 ambient for times ranging from 1 to 300 s are shown. The spectrum lineshape does not change by changing the annealing time, while the intensity increases by increasing the annealing time. We have also explored the dependence of the PL intensity on the annealing temperature for a fixed annealing time of 30 s; the data are reported in the inset of figure 4.12 and demonstrate that 1000 °C is the temperature that maximizes the PL emission. Both time and temperature dependence of the PL signal are in agreement with the model discussed above and sketched in figure 4.10. Indeed, by increasing the time or the temperature, Si diffusion inside the Eu_2O_3 film increases, with the consequent increase of the concentration of Eu^{2+}
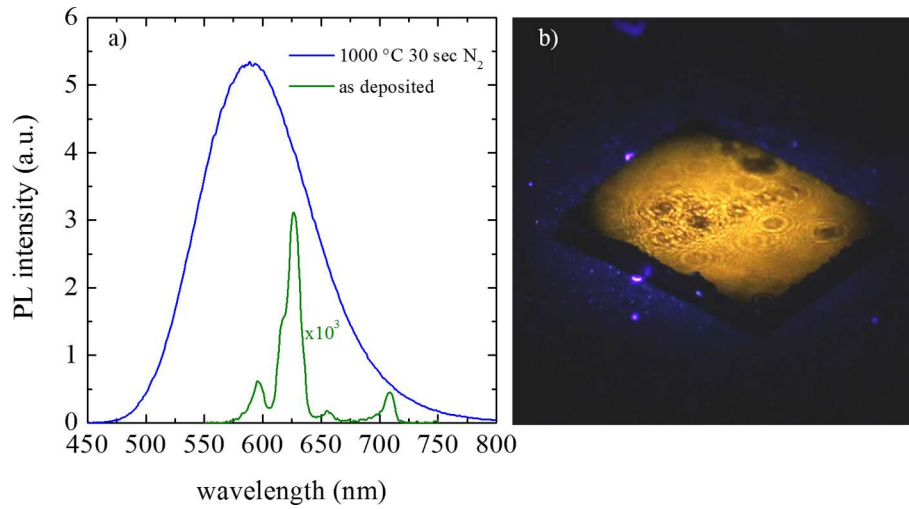
Figure 4.11: *(a) Room temperature PL spectra (obtained by exciting with the 325 nm line of a He-Cd laser) of Eu$_2$O$_3$ films as-deposited (green line) and annealed at 1000 °C for 30 s in N$_2$ (blue line). (b) Photograph of sample annealed at 1000 °C for 30 s in N$_2$ having an area of about 1 cm^2, excited by the 364 nm line of a fully defocused Ar$^+$ laser beam, showing a bright orange PL emission cleary visible by the naked eye.*

silicates, which in turn leads to an enhancement of the PL intensity. For longer annealing times, up to 1 h, or temperatures higher than 1100 °C, a massive diffusion of Si inside the whole Eu$_2$O$_3$ film occurs, leading to the formation of highly disordered regions where PL signal is quenched. From decay time measurements, same life time value, for samples annealed at different conditions, has been found, confirming that the PL quench is not due to the presence of non-radiative channels, as such as defects, but can be ascribed to the presence of optically inactive Eu centers in that regions, as discussed above.

It is noteworthy that the brightest silicates sample (the one annealed at 1000 °C for 300 s in N$_2$) shows an external quantum effi-

ciency of about 10%, which makes this material of great interest for applications in photonics or in lighting.
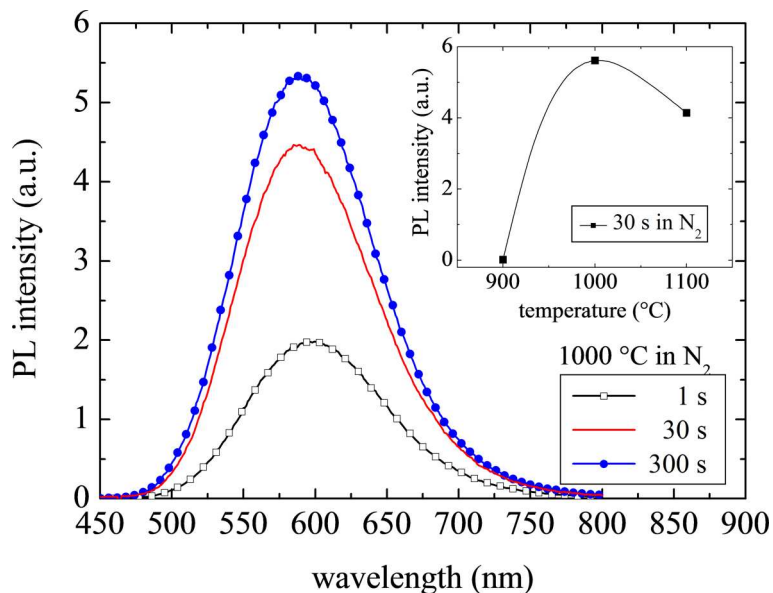
Figure 4.12: *Room temperature PL spectra of Eu_2O_3 films annealed at 1000 °C in N_2 for times ranging from 1 to 300 s. The inset shows the dependence of the integrated PL intensity on the annealing temperature for processes performed for 30 s in N_2*

Further information on the nature of Eu emission can be obtained by time-resolved PL measurements. Figure 4.13a shows the PL time-decay curve of Eu_2O_3 sample annealed at 1000 °C for 30 s in N_2 ambient, detected at a wavelength of 580 nm, corresponding to the maximum of the PL spectrum. Moreover, in figure 4.13b, the PL time-decay curve of the as-deposited Eu_2O_3 film, detected in correspondence of the emission peak at 620 nm, is displayed. It should be noticed that in figure 4.13 very different time scales have been used: for the N_2-treated sample (figure 4.13a) the time scale is in μs, while for the

as-deposited one (figure 4.13b) it is in tens of ms. By fitting the time-decay curves with a single exponential, we obtain lifetime values of about 0.36 μs for the Eu^{2+} silicate phases formed in N$_2$ ambient, and of about 3.7 ms for as deposited Eu$_2$O$_3$. This large difference in the τ values is in agreement with the different nature of the involved transitions: in the case of Eu^{2+} silicates the transitions are dipole-allowed, while in the case of Eu$_2$O$_3$ are forbidden.
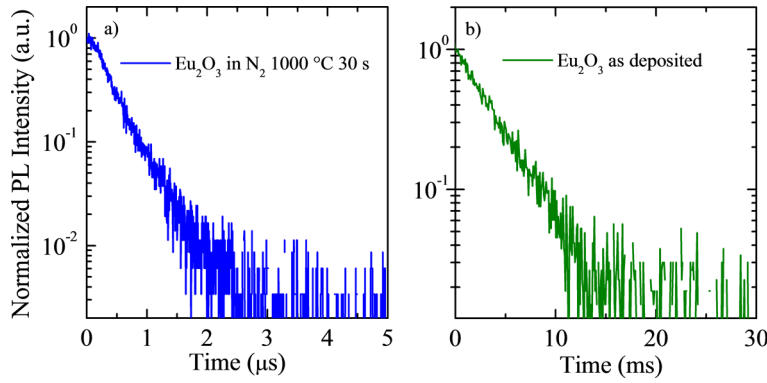
Figure 4.13: *Room temperature PL time-decay curves of Eu$_2$O$_3$ films (a) annealed at 1000 °C for 30 s in N$_2$ (b) and as-deposited, measured at 580 and 620 nm, respectively. It should be noted the different time scales used in panel (a) (μs) and (b) (tens of ms).*

The excitation properties of Eu$_2$O$_3$ films have been investigated by PLE measurements and are reported in figure 4.14. PLE spectra were obtained by integrating the PL peaks of the samples in the same range and by changing the excitation wavelength in the 250-500 nm range. The PLE spectrum of the as-deposited sample exhibits an intense excitation band for wavelengths lower than 300 nm, due to charge transfer transitions [143, 144]. These findings hold for all samples exhibiting an Eu^{3+} emission. On the other hand, N$_2$-treated samples (the figure in particular refers to an annealing at 1000 °C for 300 s)

exhibit the typical PLE spectrum of Eu^{2+}, characterized by a very intense and broad excitation band centered at about 350 nm, due to $4f^6 5d \longrightarrow 4f^7$ transitions [105, 142].
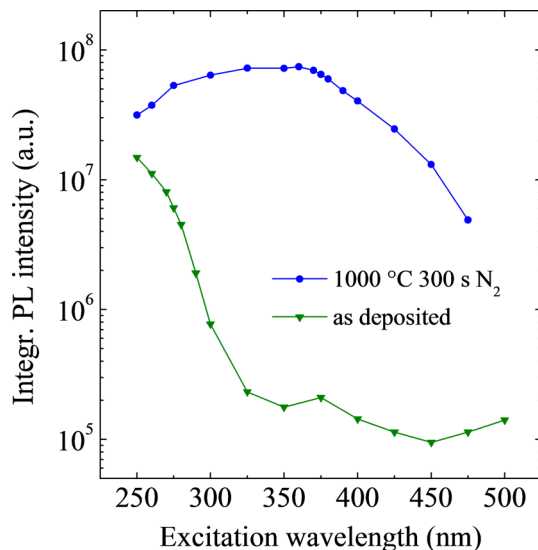
Figure 4.14: *Room temperature PLE spectra of Eu_2O_3 films as-deposited and annealed at 1000 °C for 300 s in N_2. Spectra were taken by integrating the PL peaks obtained for different excitation wavelengths.*

The intriguing dependence on the annealing process of the PL properties of Eu_2O_3 has been fully explained by the above discussed TEM and XRD structural data (figure 4.8 and 4.9). As-deposited and O_2-treated films are essentially pure Eu_2O_3 and, accordingly, exhibit the typical red emission of Eu^{3+} ions. On the other hand, the Eu^{2+} silicates formed in N_2-treated films exhibit a broader and much more intense PL signal.

The possible co-existence of Eu^{2+} and Eu^{3+} in N_2-annealed films remains a partially open question. Residual Eu_2O_3 is still detected in

the XRD spectrum of the Eu_2O_3 film annealed for 30 s, but, given the extremely different PL efficiency of the two Eu species and the overlap of the corresponding PL spectra, it is not surprising the absence of any Eu^{3+} contribution to the PL spectrum which is covered by the overwhelming Eu^{2+} contribution. This is even more obvious in the case of the annealing for 300 s, where no XRD peaks relative to Eu^{3+} compounds were detected. We remark also that no Eu^{3+} PL signal has been obtained by using an excitation wavelength of 275 nm, corresponding to an enhanced excitation efficiency for Eu^{3+} by about a factor of 30. Therefore, although the occurrence of the almost complete $Eu^{3+} \longrightarrow Eu^{2+}$ reduction suggested by XRD is a reasonable hypothesis, the presence of crystalline Eu^{3+} compounds concentrations below the detection limit of XRD, as well as of amorphous Eu^{3+} compounds, cannot be excluded a priori, also in the absence of any optical evidence.

4.6   Conclusions

This study demonstrates that annealing parameters deeply influence the structural and optical properties of Eu_2O_3 thin films grown by magnetron sputtering on Si substrates.

Annealing in oxidizing atmosphere at temperatures below 1000 °C for 1 h leads to an improvement of the film structure and composition and, in turn, to the maximization of the Eu^{3+} PL signal. If the temperature is increased up to 1000 °C, a film-substrate intermixing occurs but no crystalline silicate phases are formed. In this conditions, Eu_2O_3 shows a partial quenching of the PL signal, due to a loss of optically active Eu ions.

If the annealing ambient is changed to N_2, a completely different behaviour is found. Thermal treatments induce Si diffusion inside the Eu_2O_3 film; Si is then able to reduce the Eu^{3+} ions to Eu^{2+} and crys-

talline Eu^{2+} silicates are finally formed. It has been shown that the nature and structural and optical properties of Eu^{2+} silicates can be controlled by varying annealing time and the temperature. In particular, for annealing at 1000 °C for 30 s in N_2, an extremely strong room temperature PL emission from Eu^{2+} ions has been obtained, characterized by a very high external quantum efficiency of about 10%. This high efficiency is due to the high concentration of optically active centers, to the fact that Eu^{2+} is more easily and efficiently excitable than Eu^{3+} through a broad excitation band, and to the nature of Eu^{2+} ions, which show dipole-allowed optical transitions. These data demonstrate that it is possible, through a proper tuning of the synthesis process, to obtain Eu compounds which are very efficient light emitters in the visible region at room temperature, opening the way to new promising perspectives for applications of Eu-based materials in photonics and in solid state lighting.

Summary

Aim of this thesis has been the study of novel approaches to obtain Eu-based thin films able to emit light in the visible range, for application in lighting and Si photonics.

Among the various rare earth ions, a particular attention is currently devoted to Eu, because of its peculiar chemical and optical properties. Indeed Eu is stable both in its trivalent and divalent oxidation state; Eu^{2+} ions are characterized by a very intense and broad emission band, tunable in all the visible range, which can be of interest for many technological fields, while Eu^{3+} ions present less intense and sharp emission peaks at ~ 600 nm. In this thesis, two different approaches able to take advantage of the properties of Eu ions have been presented: i) the doping approach, which fully exploits the many advantages offered by a Si oxycarbide (SiOC) host matrix, and ii) the compound approach, which mainly focuses on Eu silicates. By centering the attention on host matrices compatible with Si technology, Eu-doped SiO_2 is a widely studied system, but its perspectives are quite poor, since the low Eu solid solubility in SiO_2 strongly limits the concentration of optically active Eu ions. On the other hand, it has been demonstrated in this thesis that a SiOC matrix is able to enhance the solubility of Eu ions by two orders of magnitude with respect to SiO_2, and simultaneously acts as an efficient reducing ambient for Eu ions, which are indeed stabilized in their divalent oxidation state. As

127

a result, Eu-doped SiOC shows a very strong room temperature PL emission in the visible range, which is more than two orders of magnitude more intense than that one of Eu-doped SiO_2. Furthermore, the occurrence of an energy transfer mechanism between the SiOC matrix and Eu^{2+} ions increases the efficiency of photon absorption for excitation wavelengths shorter than 300 nm.

Due to this properties Eu-doped SiOC offers great potentialities for the fabrication of light sources. In this thesis a continuous redshift of the emission peak from 400 to 600 nm by increasing the Eu concentration has been reported, allowing to consider this material a tunable light source. Furthermore, Eu^{2+} properties have been also used to realize a white light source, through the synthesis of a bilayer consisting of two SiOC films doped with different Eu concentrations. Through a proper choice of the annealing temperature, and taking advantage of the dependence of the PL peak position on the Eu concentration, an intense white emission at room temperature has been obtained. The CIE chromaticity coordinates of the emission are (0.33, 0.36), to be compared with those relative to an ideal white emission which are (0.33, 0.33), and the calculated color rendering index is 91/100.

The notable properties of Eu-doped SiOC films may find application in solid-state lighting or in Si photonics. These applications require further studies on the influence of C concentration on the films structural and optical properties, to obtain an increment of the optical efficiency of Eu-doped SiOC; furthermore, SiOC films with a higher C content are expected to show a significant electrical conduction, making possible the electrical excitation of this material. As far as lighting is concerned, Eu-doped SiOC may represent a possible alternative to III-V semiconductor LEDs, which require an expensive technology for their fabrication process. Indeed blue emitting materials are widely applied in lighting technology, not only as the blue component in multicolor LEDs, but also as excitation source of phosphors. Therefore the availability of new efficient blue light sources is of great importance

for further developments in lighting technology. Furthermore, since SiOC is a Si-based material, it can be well coupled with the existing Si technology, opening the way also to possible photonic applications.

The second approach discussed in this thesis is based on the synthesis of Eu compounds by thermal processing of Eu_2O_3 thin films deposited by RF magnetron sputtering on Si substrates. It has been shown that annealing processes in N_2 ambient lead to a complex reactivity at the Eu_2O_3/Si interface, which induces $Eu^{3+} \longrightarrow Eu^{2+}$ reduction and formation of stable Eu^{2+} silicates (Eu_2SiO_4 and $EuSiO_3$). These materials show a very strong and broad room temperature emission peaked at 590 nm, with a very high external quantum efficiency $\sim 10\%$. This result is very impressive, especially if we consider previously reported data for Eu silicates grown with different methods, in which an external quantum efficiency of 0.1% has been observed. Also in this case, further investigations on the possibility to electrically excite these materials can open unexpected perspectives for their application in photonics or in solid state lighting.

The results shown in this thesis demonstrate that Eu-doped SiOC and Eu silicates have the potentialities for becoming the building blocks of future devices for lighting and photonics. The development of suitable strategies for obtaining an electrical excitation in both kind of materials, coupled with a full comprehension of the dependence of their optical properties and structural features on growth conditions and post-growth processing will be able to drive a complete transition of these materials from research laboratories to devices for every-day life.

Bibliography

[1] G. Liu and X. Chen, *Handbook on the physics and chemistry of rare earths* (Elsevier B. V. Amsterdam, 2007).

[2] J. Becquerel, *Phys. Z.* **8**, 632 (1908).

[3] G. Liu and B. Jacquier, *Spectroscopic Proprieties of Rare Earths in Optical Materials* (Springer Berlin, 2005).

[4] E. Desurvire, *Erbium-doped fiber amplifiers: principles and applications* (John Wiley and Sons, 1994).

[5] G. E. Moore, *Electronics* **38** (1965).

[6] T. Miya, Y. Terunuma, T. Hosaka, and T. Miyashita, *Electron. Lett.* **15**, 108 (1979).

[7] W. J. Miniscalco, *J. Lightwave Technol.* **9**, 234 (1991).

[8] E. Mills, "The 230-billion dollars global lighting energy bill", (2002).

[9] F. Dongradi, "The commission of the european communities. implementing directive 2005/32/ec of the european parliament and of the council with regard to ecodesign requirements for non-directional household lamps", Technical report, Official Journal of the European Union (2009).

[10] A. Kitai, *Luminescent materials and application* (John Wiley & Sons, Inc., 2008).

[11] S. Nakamura and G.Fasol, *The blue laser diode* (Berlin: Springer-Verlag, 1997).

[12] S. Shionoya and W. Yen, *Phosphor Handbook* (New York: CRC Press, 1998).

[13] J. Craford, "Leds for solid state lighting and other emerging applications: status, trends and challenges", (2005).

[14] T. Taguchi, "Japanese semiconductor lighting project based on ultraviolet led and phosphor system", (2001).

[15] Y. Uchida and T. Taguchi, *J. of Opt. Eng.* **44**, 124003 (2005).

[16] M. Paniccia and S. Koehl, *IEEE Spectrum* **42**, 38 (2005).

[17] "IBM Research http://researcher.ibm.com/", .

[18] B. P. Pal, *Progress in Optics* **32**, 1 (1993).

[19] U. Hilleringmann and K. Goser, *IEEE Trans. Electron. Devices* **42**, 841 (1995).

[20] T. Miya, *IEEE J. Sel. Top. Quantum Electron.* **6**, 38 (2000).

[21] H. Zimmermann, *Integrated Silicon Optoelectronics* (Springer Berlin, 2000).

[22] L. Colace, G. Masini, G. Assanto, H. C. Luan, K. Wada, and L. C. Kimerling, *Appl. Phys. Lett.* **76**, 1231 (2000).

[23] S. M. Csutak, J. D. Schaub, W. E. Wu, R. Shimer, and J. C. Campbell, *J. Lightwave Technol.* **20**, 1724 (2002).

[24] S. Winnerl, D. Buca, S. Lenk, C. Buchal, S. Mantl, and D. X. Xu, *Mater. Sci.Eng. B* **89**, 73 (2002).

[25] P. Y. Yu and M. Cardona, *Fundamentals of semiconductors* (Springer Berlin, 1996).

[26] R. B. Hammond and R. N. Silver, *Appl. Phys. Lett.* **36**, 68 (1980).

[27] M. A. Tamor and M. A. Wolfe, *Phys. Rev. Lett.* **44**, 1703 (1980).

[28] D. Kovalev, H. Heckler, M. Ben-Chorin, G. Polisski, M. Schwartzkopff, and F. Koch, *Phys. Rev. Lett.* **81**, 2803 (1998).

[29] L. T. Canham, *Appl. Phys. Lett.* **57**, 1046 (1990).

[30] V. Lehmann and U. Gösele, *Appl. Phys. Lett.* **58**, 856 (1991).

[31] L. Pavesi, L. Dal Negro, C. Mazzoleni, G. Franzó, and F. Priolo, *Nature* **408**, 440 (2000).

[32] Z. H. Lu, D. J. Lockwood, and J.-M. Baribeau, *Nature* **178**, 258 (1995).

[33] D. J. Lockwood, Z. H. Lu, and J.-M. Baribeau, *Phys. Rev. Lett.* **76**, 593 (1996).

[34] E. Barbagiovanni, D. Lockwood, P. Simpson, and L. Goncharova, *Phys. Rev. Lett.* **76**, 593 (1996).

[35] S. Godefroo, M. Hayne, M. Jivanescu, A. Stesmans, M. Zacharias, O. I. Lebedev, G. V. Tendeloo, and V. V. Moshchalkov, *Nature Nanotechnology* **3**, 174 (2008).

[36] F. Priolo, G. Franzó, D. Pacifici, V. Vinciguerra, F. Iacona, and A. Irrera, *J. Appl. Phys.* **89**, 264 (2001).

[37] G. Franzó, A. Irrera, E. C. Moreira, M. Miritello, F. Iacona, D. Sanfilippo, G. D. Stefano, P. Fallica, and F. Priolo, *Appl. Phys. A* **74**, 1 (2002).

[38] A. Irrera, P. Artoni, F. Iacona, E. F. Pecora, G. Franzó, M. Galli, B. Fazio, S. Boninelli, and F. Priolo, *Nanotechnology* **23**, 075204 (2012).

[39] A. Hochbaum and P. Yang, *Chem. Rev.* **110**, 543 (2010).

[40] P. G. Kik and A. Polman, *MRS Bulletin* **23**, 48 (1998).

[41] A. J. Kenyon, *Progress in Quantum Electronics* **26**, 225 (2002).

[42] A. Yoshida, Y. Nakanishi, , and A. Wakahara, "Light emission from rare-earth-implanted gan expected for full-color display", (2003).

[43] M. Yoshihara, A. Sekiya, T. Morita, K. Ishii, S. Shimoto, S. Sakai, and Y. Ohki, *J. Phys. D* **30**, 1908 (1997).

[44] S. Wang, H. Amekura, A. Eckau, R. Carius, and C. Buchal, *Nucl. Instrum. Method. B* **148**, 481 (1999).

[45] C. Buchal, *Nucl. Instrum. Method. B* **743**, 167 (2000).

[46] J. Sun, W. Skorupa, T. Dekorsy, M. Helm, L. Rebohle, and T. Gebel, *J. Appl. Phys.* **97**, 123513 (2005).

[47] J. Sun, W. Skorupa, T. Dekorsy, M. Helm, L. Rebohle, and T. Gebel, *Appl. Phys. Lett.* **85**, 3387 (2004).

[48] S. Prucnal, J. M. Sun, W. Skorupa, and M. Helm, *Appl. Phys. Lett.* **90**, 181121 (2007).

[49] L. Rebohle and W. Skorupa, *Rare earth implanted MOS devices for silicon photonics* (Springer Berlin, 2010).

[50] W. Skorupa, J. Sun, S. Prucnal, L. Rebohle, T. Gebel, A. Nazarov, I. Osiyuk, and M. Helm, *Solid State Phenom.* **775**, 108 (2005).

[51] J. Sun, S. Pruncal, W. Skorupa, M. Helm, L. Rebohle, and T. Gebel, *Appl. Phys. Lett.* **89**, 091908 (2006).

[52] L. Rebohle, J. Lehmann, A. Kanjilal, S. Prucnal, A. Nazarov, I. Tyagulskii, W. Skorupa, and M. Helm, *Instrum. Methods Phys. Res. B* **267**, 1324 (2009).

[53] L. Rebohle, J. Lehmann, S. Prucnal, A. Nazarov, I. Tyagulskii, S. Tyagulskii, A. Kanjilal, M. Voelskow, D. Grambole, W. Skorupa, and M. Helm, *J. Appl. Phys.* **106**, 123103 (2009).

[54] M. Helm, J. Sun, J. Potfajova, T. Dekorsy, B. Schmidt, and W. Skorupa, *Microelectron. J.* **36**, 957 (2005).

[55] A. Nazarov, I. Osiyuk, I. Tyagulskii, V. Lysenko, S. Prucnal, J. Sun, and R. W. Skorupa, Yanko, *J. Luminesc.* **121**, 213 (2006).

[56] J. Sun, S. Pruncal, W. Skorupa, T. Dekorsy, A. Mücklich, M. Helm, L. Rebohle, and T. Gebel, *J. Appl. Phys.* **99**, 103102 (2006).

[57] S. Prucnal, J. Sun, A. Nazarov, I. Tyagulskii, I. Osiyuk, R. Fedaruk, and W. Skorupa, *Appl. Phys. B* **88**, 241 (2007).

[58] S. Prucnal, J. Sun, A. Mücklich, and W. Skorupa, *Electrochem. Solid State Lett.* **10**, H50 (2007).

[59] S. Prucnal, J. Sun, L. Rebohle, and W. Skorupa, *Appl. Phys. Lett.* **91**, 181107 (2007).

[60] S. Prucnal, J. Sun, H. Reuther, W. Skorupa, and C. Buchal, *Electrochem. Solid State Lett.* **10**, J30 (2007).

[61] S. Prucnal, J. Sun, H. Reuther, and C. Buchal, *Vaccum* **81**, 1269 (2007).

[62] S. Wang, S. Coffa, R. Carius, and C. Buchal, *Mater. Sci. Eng. B* **81**, 102 (2001).

[63] J. M. Sun, L. Rebohle, S. Prucnal, M. Helm, and W. Skorupa, *Appl. Phys. Lett.* **92**, 071103 (2008).

[64] A. Irrera, M. Miritello, D. Pacifici, G. Franzó, F. Priolo, F. Iacona, D. Sanfilippo, G. D. Stefano, and P. Fallica, *Nucl. Instrum. Methods. Phys. Res. B* **216**, 222 (2004).

[65] S. Prucnal, L. Rebohle, A. Nazarov, I. Osiyuk, I. Tyagulskii, and W. Skorupa, *Appl. Phys. B* **91**, 123 (2008).

[66] M. Castagna, S. Coffa, M. Monaco, A. Muscara, L. Caristia, S. Lorenti, and A. Messina, *Mater. Sci. Eng. B* **105**, 83 (2003).

[67] A. Irrera, F. Iacona, G. Franzó, S. Boninelli, D. Pacifici, M. Miritello, C. Spinella, D. Sanfilippo, G. D. Stefano, P. Fallica, and F. Priolo, *Opt. Mater.* **27**, 1031 (2005).

[68] S. Prucnal, L. Rebohle, and W. Skorupa, *Appl. Phys. B* **98**, 451 (2010).

[69] J. Qi, T. Matsumoto, M. Tanaka, and Y. Masumoto, *J. Phys. D* **33**, 2074 (2000).

[70] J. Qi, T. Matsumoto, M. Tanaka, and Y. Masumoto, *Appl. Phys. Lett.* **74**, 3203 (1999).

[71] B. Garrido, M. López, C. García, A. Perez-Rodriguez, J. R. Morante, C. Bonafos, M. Carrada, and A. Claverie, *J. Appl. Phys.* **91**, 798 (2002).

[72] M. López, B. Garrido, C. García, P. Pellegrino, A. Pérez-Rodríguez, J. R. Morante, C. Bonafos, M. Carrada, and A. Claverie, *Appl. Phys. Lett.* **80**, 1637 (2002).

[73] J. Heo and H. J. Kim, *J. Electrochem. Soc.* **153**, F228 (2006).

[74] S.-Y. Seo, K.-S. Cho, and J. H. Shin, *Appl. Phys. Lett.* **84**, 717 (2004).

[75] A. Perez-Rodriguez, O. Gonzalez-Varona, B. Garrido, P. Pellegrino, J. R. Morante, C. Bonafos, M. Carrada, and A. Claverie, *J. Appl. Phys.* **94**, 254 (2003).

[76] S. Gallis, V. Nikas, H. Suhag, M. Huang, and A. E. Kaloyeros, *Appl. Phys. Lett.* **97**, 081905 (2010).

[77] Y. P. Guo, J. C. Zheng, A. T. S. Wee, C. H. A. Huan, K. Li, J. S. Pan, Z. C. Feng, and S. J. Chua, *Chem. Phys. Lett.* **339**, 319 (2001).

[78] Y. Ding and H. Shirai, *J. Appl. Phys.* **105**, 043515 (2009).

[79] Y. H. Yu, S. P. Wong, and I. H. Wilson, *Phys. Status Solidi A* **168**, 531 (1998).

[80] J. Zhao, D. S. Mao, Z. X. Lin, B. Y. Jiang, Y. H. Yu, X. H. Liu, H. Z. Wang, and G. Q. Yang, *Appl. Phys. Lett.* **73**, 1838 (1998).

[81] J. Zhao, D. S. Mao, Z. X. Lin, B. Y. Jiang, Y. H. Yu, X. H. Liu, and G. Q. Yang, *Mater. Lett.* **38**, 321 (1999).

[82] S. Hayashi, M. Kataoka, and K. Yamamoto, *Jpn. J. Appl. Phys.* **32**, L274 (1993).

[83] A. Karakuscu, R. Guider, L. Pavesi, and G. D. Soraru, *J. of the American Ceramic Society* **92**, 2969 (2009).

[84] Y. Ishikawa, A. V. Vasin, J. Salonen, S. Muto, V. S. Lysenko, A. N. Nazarov, N. Shibata, and V.-P. Lehto, *J. Appl. Phys.* **104**, 083522 (2008).

[85] L. Zhuge, X. Wu, Q. Li, W. Wang, and S. Xiang, *Physica E* **23**, 86 (2004).

[86] T. Gebel, L. Rebohle, J. Sun, and W. Skorupa, *Physica E* **16**, 366 (2003).

[87] S. Gallis, M. Huang, and A. E. Kaloyeros, *Appl. Phys. Lett.* **90**, 161914 (2007).

[88] Y. Zhang, A. Quaranta, and G. D. Soraru, *Opt. Mater.* **24**, 601 (2004).

[89] M. Brewer, D. R. Bujalski, V. E. Parent, K. Su, and G. A. Zank, *J. Sol-Gel Sci. Technol.* **14**, 49 (1999).

[90] T. Rajagopalan, X. Wang, B. Lahlouh, C. Ramkumar, P. Dutta, and S. Gangopadhyaya, *J. Appl. Phys.* **94**, 5252 (2003).

[91] J. Y. Kim, M. S. Hwang, Y.-H. Kim, H. J. Kim, and Y. Lee, *J. Appl. Phys.* **90**, 2469 (2001).

[92] A. Herrmann, S. Fibikar, and D. Ehrt, *J. non-crystalline solid* **335**, 2093 (2009).

[93] N. S. Singh, H. Kulkarni, L. Pradhan, and D. Bahadur, *Nanotechnology* **24**, 065101 (2013).

[94] X. Zhao, Z. Li, T. Yu, and Z. Zou, *RSC Adv.* **3**, 1965 (2013).

[95] L. Rebohle, J. Lehmann, S. Prucnal, A. Kanjilal, A. Nazarov, I. Tyagulskii, W. Skorupa, and M. Helm, *Appl. Phys. Lett.* **93**, 071908 (2008).

[96] A. N. Nazarov, S. I. Tiagulskyi, I. P. Tyagulskyy, V. S. Lysenko, L. Rebohle, J. Lehmann, S. Prucnal, M. Voelskow, and W. Skorupa, *J. Appl. Phys.* **107**, 123112 (2010).

[97] D. Li, X. Zhang, L. Jin, and D. Yang, *Opt. Express* **18**, 27191 (2010).

[98] T. Higuchi, Y. Hotta, Y. Hikita, S. Maruyama, Y. Hayamizu, H. Akiyama, H. Wadati, D. G. . Hawthorn, T. Z. Regier, R. I. R. Blyth, G. A. Sawatzky, and H. Y. Hwang, *Appl. Phys. Lett.* **98**, 071902 (2011).

[99] C.-J. Jia, L.-D. Sun, F. Luo, X.-C. Jiang, L.-H. Wei, and C.-H. Yan, *Appl. Phys. Lett.* **84**, 5305 (2004).

[100] S. Boninelli, *Properties and Evolution of Si Nanoclusters studied by Energy Filtered Transmission Electron Microscopy*, Ph.D. thesis, Univesity of Catania.

[101] L. Krivanek, M. K. Kundmann, and X. Bourrat, *Mater. Res. Soc. Symp. Proc.* **332**, 341 (1994).

[102] "http://carine.crystallography.pagespro-orange.fr/", .

[103] N. D. Afify and G. Mountjoy, *Phys. Rev. B* **79**, 024202 (2009).

[104] M. W. Sckerl, S. Guldberg-Kjaer, M. R. Poulsen, P. Shi, and J. Chevallier, *Phys. Rev. B* **59**, 13494 (1999).

[105] Y. Qiao, D. Chen, J. Ren, B. Wu, J. Qiu, and T. Akai, *J. Appl. Phys.* **103**, 023108 (2008).

[106] Y. Tian, B. Chen, R. Hua, J. Sun, L. Cheng, H. Zhong, X. Li, J. Zhang, Y. Zheng, T. Yu, L. Huang, and H. Yu, *J. Appl. Phys.* **109**, 053511 (2011).

[107] X. Song, H. He, R. Fu, D. Wang, X. Zhao, and Z. Pan, *J. Phys. D: Appl. Phys.* **42**, 065409 (2009).

[108] X. Song, R. Fu, S. Agathopoulos, H. He, X. Zhao, and S. Zhang, *J. Appl. Phys.* **106**, 033103 (2009).

[109] G. Blasse and B. C. Grabmaier, *Luminescent Materials* (Springer Verlag, Berlin, 1994).

[110] Y. C. Shin, S. J. Leem, C. M. Kim, S. J. Kim, Y. M. Sung, C. K. Hahn, and J. H. Baek, *J. Electroceram.* **23**, 236 (2009).

[111] H. Isshiki, M. de Dood, A. Polman, and T. Kimura, *Appl. Phys. Lett.* **85**, 4343 (2004).

[112] Y. Kishimoto, X. Zhang, T. Hayakawa, and M. Nogami, *J. Lumin.* **129**, 1055 (2009).

[113] Q. Zhang, X. Liu, Y. Qiao, B. Qian, G. Dong, J. Ruan, Q. Zhou, J. Qiu, and D. Chen, *Opt. Mater.* **32**, 427 (2010).

[114] S. Gallis, M. Huang, H. Efstathiadis, E. Eisenbraun, A. E. Kaloyeros, E. E. Nyein, and U. Hommerich, *Appl. Phys. Lett.* **87**, 091901 (2005).

[115] "JCPDS Card No. 35-0297", .

[116] "JCPDS Card No. 15-0886", .

[117] J. Laegsgaard, *Phys. Rev. B* **65**, 174114 (2002).

[118] J. Linnros, N. Lalic, A. Galeckas, and V. Grivickas, *J. Appl. Phys.* **86**, 6128 (1999).

[119] G. Dong, X. Xiao, L. Zhang, Z. Ma, X. Bao, M. Peng, Q. Zhang, and J. Qiu, *J. Mater. Chem.* **21**, 2194 (2011).

[120] R. J. Xie, M. Mitomo, F. F. K. Uheda amd Xu, and Y. Akimune, *J. Am. Ceram. Soc.* **85**, 1229 (2002).

[121] A. Polman, *J. Appl. Phys.* **82**, 1 (1997).

[122] M. Miritello, R. Lo Savio, F. Iacona, G. Franzó, A. Irrera, A. M. Piro, C. Bongiorno, and F. Priolo, *Adv. Mater.* **19**, 1582 (2007).

[123] K. Suh, M. Lee, J. Chang, H. Lee, N. Park, G. Sung, and J. Shin, *Opt. Express* **18**, 7724 (2010).

[124] M. Miritello, P. Cardile, R. L. Savio, and F. Priolo, *Opt. Express* **19**, 20761 (2011).

[125] I. Bondar and N. Toropov, *Mat. Res. Bull.* **2**, 479 (1967).

[126] M. W. Shafer, *J. Appl. Phys.* **36**, 1145 (1965).

[127] G. Adachi, N. Imanaka, and Z. Kang, *Binary rare earth oxides* (Kluwer Academic Publishers, 2004).

[128] G. Busch, E. Kaldis, R. Verreault, and J. Felsche, *Mat. Res. Bull.* **5**, 9 (1970).

[129] J. Felshe, *Die Naturwissenschaften* **58**, 565 (1971).

[130] E. Kaladis and V. R., *J. Less Common Metals* **20**, 177 (1970).

[131] E. Kaldis, P. Streit, and P. Wachter, *J. Phys. Chem. Solids* **32**, 159 (1971).

[132] K. Machida, G. Adachi, J. Shiokawa, M. Shimada, M. Koizumi, K. Suito, and A. Onodera, *Inorg. Chem.* **21**, 1512 (1982).

[133] M. W. Shafer, T. R. Mcguire, and J. C. Suits, *Phys. Rev. Lett.* **11**, 251 (1963).

[134] J. Schoenes, E. Kaldis, W. Thoni, and P. Wachter, *Phys. Status Solidi A* **51**, 173 (1979).

[135] G. M. Kalvius and G. K. Shenoy, *Naturf. A* **26**, 353 (1971).

[136] M. Miritello, R. Lo Savio, A. Piro, G. Franzó, F. Priolo, F. Iacona, and C. Bongiorno, *J. Appl. Phys.* **100**, 013502 (2006).

[137] "JCPDS Card No. 43-1009", .

[138] "JCPDS Card No. 43-1041", .

[139] "JCPDS Card No. 22-0286", .

[140] "JCPDS Card No. 35-0299", .

[141] M. Nogami and Y. Abe, *Appl. Phys. Lett.* **69**, 3776 (1996).

[142] G. Gao, N. Da, S. Reibstein, and L. Wondraczek, *Opt. Express* **18**, A575 (2010).

[143] X. Ye, W. Zhuang, Y. Hu, T. He, X. Huang, C. Liao, S. Zhong, Z. Xu, H. Nie, and G. Deng, *J. Appl. Phys.* **105**, 064302 (2009).

[144] G. Wakefield, E. Holland, P. J. Dobson, and J. L. Hutchison, *Adv. Mater.* **13**, 1557 (2001).

Curriculum Vitae

Gabriele Bellocchi was born in Paternó (CT), Italy, in February 23th, 1986.

1. **Education**

   - Working, since November, 2013 at the Department of Physics and Astronomy of University of Catania, with a research contract.

   - Physics Ph. D. Student at the University of Catania and CNR-IMM-MATIS, from January 2011 to October, 2013.

   - Master Degree in Physics, obtained on October 15th, 2010 with full marks (110/110 cum laude) with a dissertation entitled: *f-d transitions of divalent ytterbium ions in halide crystals* (supervisors: Prof. Francesco Priolo, Prof. Andries Meijrink).

   - Guest student (February-July 2010) at Utrecht University, CMI Debye Institute, for research activity, under the supervision of Prof. Andries Meijrink.

   - Bachelor Degree in Physics obtained on April 22th, 2008 with full marks (110/110) with a dissertation entitled: *Silicon Raman Laser* (supervisor: prof. Francesco Priolo).

2. **Collaborations**

   - Dipartimento di Fisica e Astronomia,University of Catania, Italy.
   - CNR IMM, Catania, Italy.
   - Dipartimento di Fisica e Astronomia, University of Padova, Italy.
   - CMI Debye Institute, University of Utrecht, Netherland.
   - Consorzio Catania Ricerche

3. **Conferences participation**

   - E-MRS Spring Meeting international conference, Oral presentation, Strasburg (FR), 26th-31th May, 2013.
   - VII International Conference on f-Elements, Oral presentation, Udine (IT), 26th-31th August, 2012.
   - International school *International School of Materials for Renewable Energy*, Erice (IT), 18th-28th July, 2012.
   - E-MRS Fall Meeting international conference, Oral presentation, Warsaw (PL), 19th-23th September, 2011.
   - International school *Nano-optics for enhancing light-matter interactions on a molecular scale*, Erice (IT), 3rd-18th July, 2011.

4. **Awards**

   - Winner of the E-MRS Graduate Student Awards - Symposium G: *Alternative approaches of SiC and related wide bandgap materials in light emitting and solar cell applications* during of the E-MRS Spring Meeting, Strasbourg (FR) 26th - 31th May, 2013.

List of publications

- G. Bellocchi, G. Franzó, F. Iacona, S. Boninelli, M. Miritello, F. Priolo, "Synthesis and characterization of light emitting Eu_2O_3 films on Si substrates", *J. Lumin.*, **132**, 3133 (2012).

- G. Bellocchi, G. Franzó, F. Iacona, S. Boninelli, M. Miritello, T. Cesca, F. Priolo, "Eu^{3+} reduction and efficient light emission in Eu_2O_3 films deposited on Si substrates", *Opt. Express*, **20**, 5 (2012).

- S. Boninelli, G. Bellocchi, G. Franzó, M. Miritello, F. Iacona, "New strategies to improve the luminescence efficiency of Eu ions embedded in Si-based matrices", *J. Appl. Phys.*, **113**, 143503 (2013).
  This publication has deserved the cover of the issue 14, volume 113 of the journal, and it has been placed among the top 25% most downloaded articles published in the Journal of Applied Physics since January 1, 2013.

- G. Bellocchi, F. Iacona, M. Miritello, T. Cesca, G. Franzó, "SiOC thin films: an efficient light source and an ideal host matrix for Eu^{2+} ions", *Opt. Express*, **21**, 20280 (2013).

- G. Bellocchi, F. Franzó, M. Miritello, F. Iacona, "White light

emission from Eu-doped SiOC films", *App. Phys. Express*, in press, (2013).

- G. Bellocchi, G. Franzó, S. Boninelli, M. Miritello, T. Cesca, F. Iacona, F. Priolo, "Structural and luminescence properties of undoped and Eu-doped SiOC thin films", submitted to *IOP Conf. Series: Mater. Sci. Eng.*, (2013).

- S. Boninelli, A. Shakoor, K. Welma, T. F. Krauss, L. O'Forlain, R. Lo Savio, S. Portalupi, D. Gerace, M. Galli, P. Cardile, G. Bellocchi, G. Franzó, M. Miritello, F. Iacona, F. Priolo, "Microscopic investigations of advanced thin films for photonics", *J. Phys.: Conf. Ser.* **471**, 012004 (2013).